

# Theoretical studies of laser induced torsion of molecules

Christian B. Brandt, 20071902

July 20, 2012



Master's thesis

Advisor: Lars Bojer Madsen

Department of Physics and Astronomy  
Aarhus University



## Abstract

Control of molecular degrees of freedom by ultrashort laser pulses is an exciting field that has emerged over the past few decades. Recent experiments [1, 2, 3] have shown that it is now possible to initiate torsional motion of biphenyl-like molecules. A theoretical model of the process has been introduced previously, but this model makes some approximations that can be avoided. In this thesis, a more precise model is introduced and implemented numerically, and the theoretical results are compared to experiments. These theoretical results show a better agreement with experiments than the results of the previous model, and working with this improved model has also improved the understanding of the experiments. It is shown that a certain change in the polarization direction of one of the lasers in the experiments will lead to an increase in the amplitude of torsional oscillations, and it is suggested to apply this to future experiments. Other ideas for gaining a better control of molecular torsion are also discussed, and it is found that using trains of kick pulses cannot possibly increase the torsional amplitude by more than a factor of two. If total control of the torsional motion is achieved in the future, it may be applied to e.g. time-resolved measurements of deracemization.

## **Thank you**

I would like to thank my advisor Lars Bojer Madsen for giving me the opportunity to work on this exciting master's project, and Christian Bruun Madsen for insight in the model he has previously implemented. I am also grateful to Ole Sørensen for his help with the exact separation of rotation and torsion. Rasmus Lauritsen, Sabrina Tang Christensen, and Sidse Damgaard Hansen deserve a round of applause for their willingness to read and comment on my thesis.

Finally, I would like to thank my amazing girlfriend Rikke for supporting me, especially during the final intense writing process.

# Contents

<b>Contents</b>	<b>iii</b>
<b>1 Introduction</b>	<b>1</b>
1.1 Outline of the thesis . . . . .	2
<b>2 Lasers and molecules</b>	<b>3</b>
2.1 Short laser pulses . . . . .	3
2.2 Interaction between molecule and laser . . . . .	5
2.3 Molecular field-free eigenstates . . . . .	5
2.4 Alignment of molecules . . . . .	8
2.5 Chiral molecules and deracemization . . . . .	12
2.6 Density matrix formalism: Mixed states in a molecular gas . . . . .	13
<b>3 The experiments and a model of the molecule</b>	<b>15</b>
3.1 Description of the experiments . . . . .	15
3.2 Model of the molecule . . . . .	16
3.3 Experimental results . . . . .	21
3.4 Summary . . . . .	25
<b>4 Interaction between a non-ionizing laser and a gas of molecules</b>	<b>27</b>
4.1 Qualitative theory . . . . .	27
4.2 Quantitative approach . . . . .	29
4.3 Application of the results to the experiments of interest . . . . .	34
4.4 Summary . . . . .	35
<b>5 A semiclassical model</b>	<b>37</b>
5.1 Outline of the model . . . . .	37
5.2 The angles $\phi_d$ and $\Phi$ . . . . .	37
5.3 Reduction to a 1D problem . . . . .	40
5.4 Numerical solution of the 1D equation . . . . .	41
5.5 Results: Eigenvalues and eigenstates . . . . .	43
5.6 Inclusion of the kick pulse . . . . .	44
5.7 Results: Time-dependent simulations . . . . .	46
5.8 Problems with the semiclassical model . . . . .	49
5.9 Summary . . . . .	50
<b>6 2D quantum mechanical models: The torsional potential</b>	<b>51</b>
6.1 The dihedral angle $\phi_d$ and the overall rotational angle $\Phi$ . . . . .	52
6.2 Simple coordinates: $\phi_1$ and $\phi_2$ . . . . .	52

6.3	Another choice of coordinates . . . . .	56
6.4	Correct boundary conditions and periodicities of $\phi_d$ and $\Phi$ . . . . .	57
6.5	Summary . . . . .	62
<b>7</b>	<b>2D quantum mechanical models: Inclusion of the kick pulse</b>	<b>63</b>
7.1	Solving in a basis . . . . .	64
7.2	Split-step method . . . . .	64
7.3	Propagation in "imaginary time" . . . . .	67
7.4	Comparing to experiments . . . . .	67
7.5	Discussion of the $(\phi_d, \Phi)$ -coordinates . . . . .	68
7.6	Summary . . . . .	69
<b>8</b>	<b>Results of a 2D quantum mechanical model</b>	<b>71</b>
8.1	Oscillations in $\langle \phi_d \rangle$ . . . . .	71
8.2	The period of the oscillations . . . . .	74
8.3	Oscillation amplitude for different initial values of $\Phi$ . . . . .	76
8.4	Variation of the degree of initial 3D alignment . . . . .	78
8.5	Four-dot structure and delocalization . . . . .	80
8.6	Discussion of more general initial states . . . . .	83
8.7	Summary . . . . .	85
<b>9</b>	<b>Future perspectives</b>	<b>87</b>
9.1	Laser induced deracemization . . . . .	87
9.2	Quantum optimal control . . . . .	89
9.3	Molecular switch . . . . .	90
<b>10</b>	<b>Conclusion</b>	<b>91</b>
<b>A</b>	<b>Matrix elements of the torsional potential</b>	<b>93</b>
	<b>Bibliography</b>	<b>97</b>

# Chapter 1

## Introduction

Lasers have been used to extract information from atomic and molecular systems ever since their invention in 1960. During the past few decades, light sources with a very short duration have been developed, as short as a hundred attoseconds ( $\sim 100 \times 10^{-18}$  s) [4]. These light sources are called ultrashort laser pulses, and they have shown great potential for studying quantum phenomena with a very high time-resolution. With this new tool, it is even possible to observe a quantum system on its natural time scale. Apart from being very short in time, these pulses have a very high peak intensity, which has opened a door to new phenomena that are not seen with ordinary light sources. Examples of such phenomena are multiphoton ionization and high-harmonic generation [5, 6].

Ultrashort laser pulses have a wide range of applications. Matter can be cut and blasted away with laser ablation [7, 8], telecommunication systems can be improved [9, 10], and the pulses are a convenient tool for accessing the dynamics of molecules and chemical reactions [11]. The application of interest in this thesis is to access the external and internal degrees of freedom of a molecule. Molecules can be slowed down [12], deflected [13], focused [14], aligned and rotated [15] by ultrashort laser pulses, and it has been shown that the vibrational motion can also be controlled [16]. In this thesis, the focus will be on the effects of laser fields on torsional motion of molecules. Torsion is the twisting of an object due to an applied torque. In 2009, the group of Henrik Stapelfeldt conducted an experiment that resulted in two papers [1, 2] where a method for accessing the torsional degree of freedom for a certain molecule was described. The molecule of their choice is 3,5-difluoro-3',5'-dibromobiphenyl (DFDBrBPh), an axially chiral molecule, and the method involves three different ultrashort lasers. The experiment was improved in [3] from 2012, partly by using a different molecule, 3,5-difluoro-3',5'-dibromo-4'-cyanobiphenyl (DFDBrCNBPh).

One of the reasons for studying the torsion of biphenyls like DFDBrBPh and DFDBrCNBPh is their axial chirality. If the molecular torsion can be controlled, one can twist the chiral molecule into its mirror form, from one enantiomer to another, by rotating the two phenyl rings with respect to each other. Such a transition would pave the way towards light-induced deracemization, that is creation of an excess of one enantiomer over the other. This reaction can be studied in a time-resolved manner because the duration of the laser pulses involved is so short.

The transfer from one enantiomer to the other has been studied theoretically in a large number of cases [17, 18, 19, 20], but until this day there has not been an *experimental* realization of laser induced deracemization. The experiments in [1, 2, 3] have shown that the torsional motion can be probed, and the method may lead to control of torsion in the future. It is therefore of great interest to provide a theory that can be applied to these experiments with

the goal of finding the direction towards deracemization, or at least towards improving the control of the torsional motion.

The experiments in [1, 2, 3] follow an outline given by [21], which is to use the alignment dynamics of molecules to induce torsional motion. This strategy seems to have a chance of being experimentally feasible, since alignment dynamics are already well understood and controlled [15]. In [21], a single circularly or elliptically polarized pulse was used theoretically to probe the torsional motion, but it was later shown that this approach will not lead to a confinement in the torsional angle [22]. Methods with more than one pulse have also been discussed theoretically and applied to biphenyl-like molecules in [23, 24].

In this thesis, a theory for laser induced torsion in biphenyl-like molecules is presented. It is an extension of the theory described in [2], and the results will be compared to the previous theory and the experiments [1, 2, 3]. The model from [2] separates torsional and rotational motion by doing an approximation, which is avoided in the model in this thesis. Therefore, we expect to find a better agreement between theory and experiments than what has previously been found. A more exact model requires numerical solution of more equations than the model used in [2]. A large part of the work behind this thesis has thus been dedicated to implementing the model in MATLAB in order to find new theoretical results. These new calculations can hopefully guide experimentalists towards better control of molecular torsion.

## 1.1 Outline of the thesis

This thesis focuses on the implementation of a model that describes the experiments in [1, 2, 3], where non-ionizing lasers and chiral molecules are involved. The model is inspired by a one-dimensional semiclassical model presented in [2].

Most of the introductory theory is explained in chapter 2: The theory behind laser pulses, molecules and an introduction to their interaction is discussed. Most of this is known if the reader has a basic knowledge of atomic and molecular physics. A section on chiral molecules has been added for the reader that is unfamiliar with this branch of chemistry, and finally, the rather complicated state of a molecular gas is described by the density matrix formalism.

In chapter 3, the experiments in [1, 2, 3] and their results are discussed along with the main ideas in modelling the molecule. Chapter 4 treats the interaction between a non-ionizing, off-resonant laser and a molecule. The result is applied to the system describing the experiments in [1, 2, 3].

In chapter 5 the semiclassical model used in [2] is described, and chapters 6 and 7 deal with the central model of this thesis. It is a two-dimensional model, so the simulations are harder to implement and need longer time to run than the model of chapter 5. The problem of finding a proper initial state for solving the 2D model is described in chapter 6. This problem involves solving a time independent Schrödinger equation, which is carried out in different coordinate systems. At the end of this chapter a new explanation of some of the success of the semiclassical 1D model is given. Chapter 7 describes the implementation of the actual solution of the 2D model.

In chapter 8, the results of the 2D model are presented and compared to experiments and the 1D semiclassical model in [2]. Some possible future applications are discussed in chapter 9 along with a few ideas for improving the control of the torsional motion. Appendix A shows some of the analytical calculations used in chapter 6.

Atomic units are used in this thesis, except in parts of chapter 4. These units set the value of the electron mass ( $m_e$ ), the elementary charge ( $e$ ), the reduced Planck's constant ( $\hbar$ ), and the Coulomb constant ( $1/4\pi\epsilon_0$ ) equal to one.



## Chapter 2

# Lasers and molecules

The technique used in the experiments in [1, 2, 3] is based on focusing ultrashort lasers onto a molecular system. In order to understand the theory explaining these experiments, it is necessary to have some knowledge of both short laser pulses and of molecular systems. This chapter will provide such knowledge, starting with the laser pulses in section 2.1. Afterwards the interaction between lasers and molecules is briefly discussed in section 2.2, and molecular states will be described in section 2.3. Section 2.4 studies alignment of molecules by laser pulses, and chiral molecules are the subject of section 2.5. This section is included because the molecules used in the experiments are chiral, and that will play a role later in the thesis. Finally the statistical state of a molecular system is described in section 2.6.

### 2.1 Short laser pulses

Laser light can be divided into two categories: continuous wave laser light and laser pulses. The former type is characterized by a constant intensity of often monochromatic light, containing only a single wavelength. Laser pulses, on the other hand, only appear for a short interval of time, as the name suggests. Such pulses do not have a completely well-defined wavelength, which can be seen from the following argument: Monochromatic light can be thought of as a sine wave, which is a continuous wave, not a pulse. To get a laser pulse, one has to superpose light of many different wavelengths.

An example showing the main characteristics of a laser pulse can be seen in figure 2.1. The pulse consists of oscillations on a small scale that are damped by an overall envelope function. Mathematically, we can write the electric field of the pulse as

$$\mathbf{F}(t) = F_0(t)\mathbf{e} \cos(\omega t + \delta), \quad (2.1)$$

where  $F_0(t)$  is the envelope function,  $\mathbf{e}$  is the polarization,  $\omega_0$  is the central frequency of the pulse and  $\delta$  is the phase. Such a pulse contains many different frequencies, and a pulse that is Gaussian in the time domain will also be Gaussian in the frequency domain. For a Gaussian laser pulse, it can be shown by Fourier analysis that

$$\Delta\omega \cdot \tau \geq 4 \log 2, \quad (2.2)$$

where  $\tau$  is the full width at half maximum (FWHM) of the Gaussian in the time domain, and  $\Delta\omega$  is the FWHM of the laser pulse in the frequency domain. For this thesis, Gaussian pulses will be used, and they will be characterized by their FWHM widths.

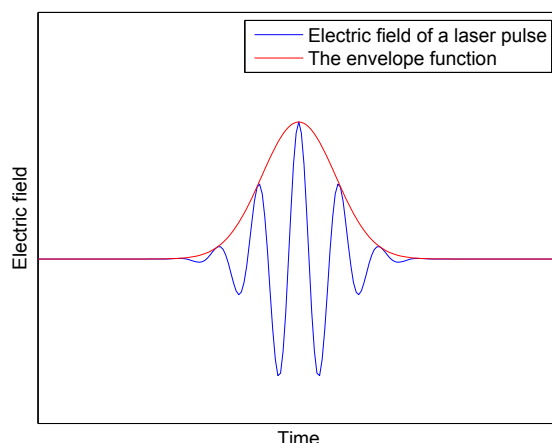


Figure 2.1: A laser pulse in the time domain. It can be characterized by oscillations on a small time scale that are damped by an envelope function.

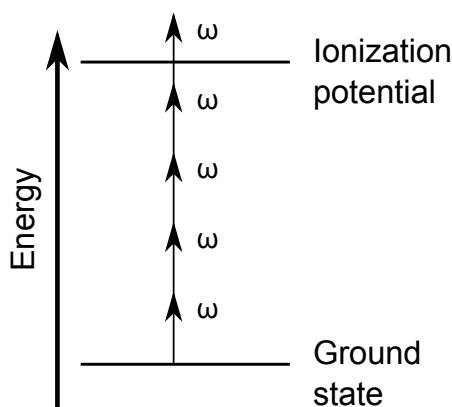


Figure 2.2: Multiphoton ionization. An intense laser field can ionize, even though the individual photons do not have the required energy.

In recent years it has been possible to obtain ultrashort laser pulses on the femtosecond ( $10^{-15}$  s) and even attosecond ( $10^{-18}$  s) time scale in laboratories around the world. For such short pulses, the peak intensity can become very high, which opens for studying new phenomena, as described in chapter 1. The shortness of the pulses also allows for measuring on a very small time scale. The relevant time scale for nuclear motion is picoseconds ( $10^{-12}$  s) and for electronic motion it is attoseconds, so these pulses can actually be used to measure the *dynamics* of a chemical reaction or molecular motion. In the future they may even be applied in time-resolved measurements of electronic motion.

As shall later be seen, the type of process studied in this thesis requires the laser field to be non-ionizing. This means that the wavelength of the laser must not be too short, and

furthermore the pulse must not be too intense. The last condition appears because a very intense laser can ionize a molecule even though the energy of the individual photons is not large enough. The phenomenon is called *multiphoton ionization*, and it is illustrated in figure 2.2. When the intense field hits the molecule, there is a chance that the molecule will absorb a large number of photons at once. Their total energy may be larger than the ionization potential, and then ionization is possible [5].

If we want to quantify how likely a given pulse is to ionize a molecule, it is not enough to look at the intensity of that pulse. If the pulse is longer there is more time for ionizing, so the relevant parameter is the intensity integrated over time. This is called the *fluence* of the pulse.

## 2.2 Interaction between molecule and laser

To describe the interaction between molecules and light, a semiclassical model is often used. The electric field of the laser is treated classically, as was already done in (2.1), whereas the molecule will be treated quantum mechanically. This model works very well when many photons are considered, which is the case for laser fields of high intensity, like short pulses, and even for low intensity as well [25]. The idea of the model is to incorporate the classical field in the Schrödinger equation for the molecular states  $\Psi(\mathbf{r}, t)$ , where  $\mathbf{r}$  denotes the coordinates of the electrons in the molecules. The results of this model are simplified if the *dipole approximation* is used. The dipole approximation states that the wavelength of the field is so long that it is almost constant over the dimensions of the molecule. For laser wavelengths above 100 nm, it is a good approximation for molecular systems. One can obtain (see chapter 4 in [25])

$$i\frac{\partial}{\partial t}\Psi(\mathbf{r}, t) = \left( \frac{\mathbf{p}^2}{2m} + V(\mathbf{r}) - \boldsymbol{\mu} \cdot \mathbf{F} \right) \Psi(\mathbf{r}, t), \quad (2.3)$$

where  $\boldsymbol{\mu}$  is the dipole moment of the molecule. The reason why the approximation is called the dipole approximation, is that the term in (2.3) that corresponds to an interaction between the laser field and the molecule is exactly the energy of an electric dipole. The way the interaction is represented in (2.3) is called the *length gauge*, because  $\boldsymbol{\mu} = q\mathbf{r}$ , so that the "length"  $\mathbf{r}$  is present in the interaction term. Other choices of gauge exist, but they will not be treated in this thesis. The only comment to be made is that the different gauges are in principle equivalent, but they can give different results when doing certain approximations [26].

Equation (2.3) will be the starting point for a calculation of the interaction between laser field and molecule in the case of a non-ionizing field, which will be done in chapter 4.

## 2.3 Molecular field-free eigenstates

In order to understand the interaction between laser and molecule on a deeper level than in the section above, we need to know the field-free eigenstates of a molecular system. The degrees of freedom of a molecule can be divided into three categories: motion of the valence electrons, vibration of the nuclei, and rotation of the molecule. Since nuclei are significantly heavier than electrons and both are submitted to forces of comparable magnitude, the nuclei will move much slower than the electrons. This means that the positions of the nuclei  $\mathbf{R}$  can be kept constant while solving the Schrödinger equation for the electronic motion. This is the Born-Oppenheimer (BO) approximation, and the result is that the nuclear and electronic motion is decoupled. This approximation will now be derived in a more quantitative way, much like it is done in chapter 10 in [25].

The total problem is given by the Hamiltonian

$$H = T_N + T_e + V, \quad (2.4)$$

where  $T_N$  is the nuclear kinetic energy,  $T_e$  the electronic kinetic energy and  $V$  the interaction between different particles. To find a set of basis states to expand the solution of this problem in, we study the time-independent Schrödinger equation for a Hamiltonian like (2.4), but with the nuclear coordinates fixed. This means that  $T_N$  is zero, so the equation reads

$$H_e(\mathbf{r}, \mathbf{R})\chi_q(\mathbf{r}, \mathbf{R}) = E_e(\mathbf{R})\chi_q(\mathbf{r}, \mathbf{R}), \quad (2.5)$$

where  $H_e = T_e + V$  is the electronic Hamiltonian,  $\mathbf{r}$  and  $\mathbf{R}$  represent the coordinates of all electrons and nuclei respectively. The states  $\chi_q(\mathbf{r}, \mathbf{R})$  are the solutions to the equation, and they are called electronic states.  $E_q(\mathbf{R})$  is the electronic energy, which depends on the nuclear coordinates. There are several solutions for each value of  $\mathbf{R}$ , and they form a complete orthonormal set, which means that the eigenstates  $\Psi$  of the Hamiltonian (2.4) can be expanded as

$$\Psi(\mathbf{r}, \mathbf{R}) = \sum_q F_q(\mathbf{R})\chi_q(\mathbf{r}, \mathbf{R}). \quad (2.6)$$

$F_q(\mathbf{R})$  represents the nuclear motion when the electrons are in state  $q$ . Now, the equation  $H\Psi = E_{\text{tot}}\Psi$  is projected onto an electronic state  $\chi_s$ , and the result is a coupled set of equations, one for each electronic state  $\chi_s$ ,

$$\sum_q \langle \chi_s | H - E_{\text{tot}} | \chi_q \rangle F_q(\mathbf{R}) = 0, \quad s = 0, 1, 2, \dots \quad (2.7)$$

where  $E_{\text{tot}}$  is the energy corresponding to the total Hamiltonian  $H$ . These coupled equations are still exact, but now the BO approximation will be used. We neglect some of the terms in (2.7) that correspond to actions of  $T_N$  on the electronic states  $\chi_q$ . This approximation holds because the electronic states vary slowly with  $\mathbf{R}$  compared to  $F_q$ , which represents the nuclear motion. After making this approximation, (2.7) reduces to an uncoupled set of equations for  $F_q$ , and therefore one can make the ansatz

$$\Psi_q = F_q(\mathbf{R})\chi_q(\mathbf{r}, \mathbf{R}). \quad (2.8)$$

The derivation above shows how the BO approximation separates electronic ( $\chi_q$ ) and nuclear ( $F_q$ ) motion. A similar approach will be used in section 6.4, which is why the derivation has been included in this thesis. Now, to find the molecular state  $\Psi$ , the electronic states have to be found first, since the electronic energies  $E_q(\mathbf{R})$  will be present in the equations (2.7) playing the role as a potential. The states  $F_q$ , representing both vibrational and rotational motion, can be found by solving the uncoupled equations that emerge from using the BO approximation on (2.7).

Solving the electronic part of the Schrödinger equation gives the electronic states and their electronic energies. These energies will depend on the positions of the nuclei  $\mathbf{R}$ , and the separation between two states is of the order of a few eV. This can be seen in figure 2.3 along with the vibrational and rotational states. These states will, unlike the electronic states, only depend on the positions of the nuclei. The difference between two vibrational states is two orders of magnitude smaller than the difference between electronic states, and for the rotational states it is four orders of magnitude. A harmonic oscillator is often used to describe a vibrating system, so the vibrational energy levels will be

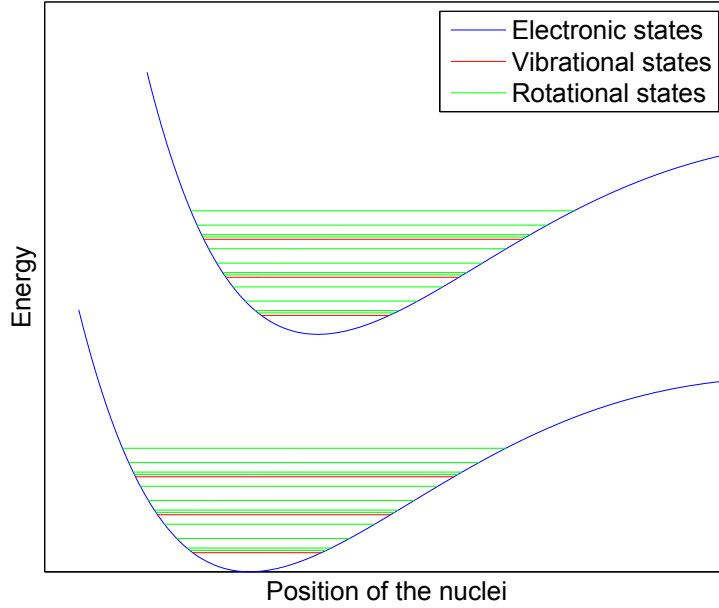


Figure 2.3: Molecular field-free eigenstates. The blue curves show the electronic energies which depend on the coordinates of the nuclei, here represented by just one coordinate. The vibrational states are marked by red lines and the rotational states by green, with energies given by (2.9) and (2.10). Note that the energies are not to scale in this figure, since the electronic energy scale should be two orders of magnitude larger than the vibrational energy scale.

$$E_{\text{vib}} = \hbar\omega(\nu + 1/2), \quad (2.9)$$

where  $\omega$  is the characteristic frequency of the vibrations and the integer  $\nu$  labels the vibrational states. The energy for rotational motion can be shown to be of the form

$$E_{\text{rot}} = BK(K + 1), \quad (2.10)$$

where  $B$  is the rotational constant and  $K$  the integer used label the rotational states. See chapter 10 in [25] for a derivation of these energy levels. In figure 2.3 the energy levels are shown. Notice that it requires an ultraviolet laser to do a coupling between two electronic states, because the separation between electronic states is a few eV. The lasers used in [1, 2, 3] are all infrared. The rotational and vibrational states are often called rovibrational states when one does not want to make a distinction between them.

Transitions between molecular states are limited by the Franck-Condon principle. Since the nuclear positions in figure 2.3 change slowly, any transition must happen vertically. Not all molecular states have a population for all positions of the nuclei, so this principle limits the number of allowed transitions.

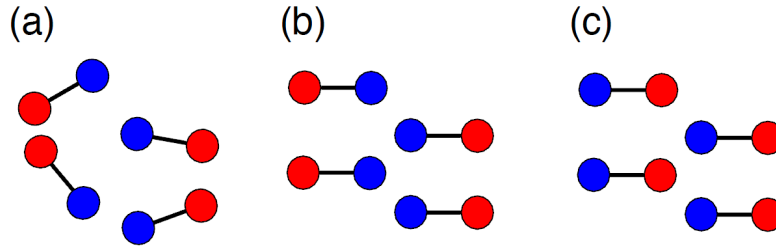


Figure 2.4: Illustration of alignment and orientation of molecules of heteronuclear diatomic molecules. (a) Unaligned, (b) aligned and (c) oriented molecules. This figure is taken from [26].

The time scale of any kind of motion depends on the separation between the relevant energy levels. This is because the time dependent part of each eigenstate of the field-free molecular Hamiltonian is  $e^{-iEt}$ , which oscillates with a period of  $2\pi/E$ , so for a superposition of eigenstates,

$$\Psi = \sum_n c_n \psi_n e^{-iE_n t}, \quad (2.11)$$

expectation values will contain a lot of terms with different time-dependent factors,

$$\langle A \rangle = \sum_{m,n} c_m^* c_n e^{i(E_n - E_m)t} \int \psi_m^* A \psi_n dx. \quad (2.12)$$

These terms have periods of  $2\pi/(E_n - E_m)$ , and the largest of these periods will determine when the system has returned to its original state. So the period of this motion is

$$T \approx \frac{2\pi}{\Delta E}, \quad (2.13)$$

where  $\Delta E$  is a typical difference between two energy levels. For electronic motion, the typical energy difference is a few eV, as stated earlier, meaning that the time scale is femtoseconds. For vibration, it will thus be picoseconds, since the energy scale is two orders of magnitude smaller. The time scale for rotational motion is two orders of magnitude larger than for vibrational motion, although still in the region of picoseconds.

## 2.4 Alignment of molecules

Molecules can be affected by lasers in many ways. When one uses lasers that have very high frequency or are very intense, the molecules will ionize or even dissociate, but non-ionizing lasers can be used to control molecules. One possible way of controlling molecules is to fix their orientation in space with respect to some axis. This is called laser induced alignment or orientation. The distinction between alignment and orientation is shown in figure 2.4 for diatomic heteronuclear molecules. *Alignment* is when the axis of the molecules is fixed, but they are allowed to point in both directions along this axis. *Orientation* also requires that the molecules are pointing in the same direction, meaning that the inversion symmetry is broken.

Now, the interaction between the laser and molecule will be described from a different perspective than in section 2.2. When a non-ionizing electric field  $\mathbf{F}$  interacts with a molecule,

the molecule is polarized, and a dipole moment  $\mu$  is induced. This induced dipole moment depends on the polarizability of the molecule. Some molecules polarize more readily in some directions than in others because of their lack of symmetry. Therefore  $\mu$  might point in a different direction than  $F$ . It is usually assumed that  $\mu$  is related linearly to  $F$  by

$$\mu = \alpha F, \quad (2.14)$$

where  $\alpha$  is the polarizability tensor which has nine components. The relation can also be written as

$$\begin{aligned} \mu_x &= \alpha_{xx}F_x + \alpha_{xy}F_y + \alpha_{xz}F_z \\ \mu_y &= \alpha_{yx}F_x + \alpha_{yy}F_y + \alpha_{yz}F_z \\ \mu_z &= \alpha_{zx}F_x + \alpha_{zy}F_y + \alpha_{zz}F_z \end{aligned} \quad (2.15)$$

This is the most general linear relation, and higher order corrections to  $\mu$  are neglected here.

Apart from this induced dipole moment, the molecule might also possess a permanent dipole moment  $\mu_0$ . This is for instance the case for diatomic molecules consisting of two different atoms.

The electric field  $F$  can now interact with the induced dipole moment  $\mu$  and the permanent dipole moment  $\mu_0$ . The laser will often be in the near-infrared regime at wavelengths around 800–1000 nm. Such a laser has a period of a few femtoseconds, while the time scale for molecular dynamics is picoseconds, as seen in section 2.3. Therefore, the interaction between the laser and the molecule can safely be averaged over a laser pulse. This makes the interaction with  $\mu_0$  vanish, since  $\mu_0$  is constant while  $F$  is oscillating back and forth. Because  $\mu$  depends on  $F$ , the interaction with  $\mu$  does not vanish. The result is that the polarizability determines the dynamics of the molecule in the field from a short laser pulse.

When a molecule is hit by a linearly polarized pulse with an electric field given by (2.1), the following will happen: Classically, the laser will exert a torque on the molecule, which will result in rotation. If the duration of the laser pulse is long compared to the molecular dynamics, it will actually align the molecule along the axis of polarization. The molecular axis that is aligned is the most polarizable axis (MPA), since the interaction is governed by the polarizability. Because the torque will be stronger whenever molecules are far from being aligned, there will eventually be some degree of alignment. This degree of alignment will follow the envelope of the pulse. The concept described here is called *adiabatic* alignment, because the pulse is long and the envelope only changes slowly compared to the rotational dynamics of the molecule. The technique works very well for a nanosecond pulse, since the rotational dynamics happen on a picosecond time scale.

If an elliptically polarized pulse is used instead of the linearly polarized pulse described above, it is also possible to get adiabatic alignment, but this time, the molecule will be three-dimensionally aligned. The field vector of the pulse draws an ellipse during one optical cycle, and we average over such a cycle as before. As a result, the MPA of the molecule will be aligned with the major axis of the ellipse, and the second most polarizable axis (SMPA) will be aligned with the minor axis. The SMPA is the most polarizable axis that is perpendicular to the MPA.

Another way to achieve 3D alignment is to use two linearly polarized pulses that are polarized perpendicular to each other. The first pulse can align the MPA with its polarization axis, and analogously the second pulse can align the SMPA. The alignment of the SMPA is caused by the tendency for second pulse to align the most polarizable accessible axis with its

polarization. This time the MPA is already aligned perpendicular to the polarization of the kick pulse, so it will align the SMPA with its axis of polarization instead.

There is however a downside to the adiabatic alignment. Alignment is only achieved while the field is strong, and when the pulse is gone, there will no longer be alignment. The alignment pulse may affect the molecules in other ways than just aligning them, so with this technique it is not possible to do any experiments on aligned molecules that are unaffected by external forces. It is actually possible to achieve alignment under field free conditions by the use of *non-adiabatic* alignment schemes. The idea is to use a pulse that is considerably shorter, so that the envelope is no longer slowly changing compared to rotational dynamics. Since rotation happens on a time scale of many picoseconds, the technique can work for a pulse length less than a picosecond.

Now, the pulse will "kick" the molecules so that they start rotating, and since the pulse is short, the rotation will continue after the pulse is gone. The molecules are rotating out of phase with each other, so after a certain time, they will end up being aligned. This alignment occurs when the field of the pulse is no longer playing any role, so it is field-free alignment. This method is not a perfect solution to the problem of alignment, though, as the alignment will only take place for a very short time.

The non-adiabatic alignment can also be described quantum mechanically by looking at wave packet revivals. The pulse kicks the initial molecular state into a wave packet of different rotational states,

$$\Psi = \sum_K c_K e^{-iE_K t} |K\rangle, \quad (2.16)$$

where  $K$  is a rotational index,  $|K\rangle$  are the rotational states and  $E_K$  are the corresponding energies given by

$$E_K = BK(K+1). \quad (2.17)$$

When this wave packet evolves in time, it will experience a revival after a certain revival time  $T_{\text{rev}}$ , where the wave packet returns to its original form. This revival will happen when the phases  $e^{-iE_K t}$  are all equal to one, i.e.

$$E_K T_{\text{rev}} = 2\pi N_K, \quad (2.18)$$

where  $N_K$  is an integer that depends on  $K$ , but  $T_{\text{rev}}$  must be the same for all  $K$ . Inserting (2.17) into (2.18) yields

$$T_{\text{rev}} = \frac{2\pi}{B} \frac{N_K}{K(K+1)}. \quad (2.19)$$

We can get a value of  $T_{\text{rev}}$  that is independent of  $K$  by choosing  $N_K$  to be  $K(K+1)$  multiplied by an integer, and the smallest integer that works is 1. The conclusion is that revival of the wave packet will be seen at the time

$$T_{\text{rev}} = \frac{2\pi}{B}. \quad (2.20)$$

When one wants to measure whether or not molecules are aligned, one cannot observe the wave function directly. It is necessary to look at expectation values. The observable  $\langle \cos^2 \theta \rangle$  is normally used, where  $\theta$  is the angle between the MPA of the molecule and the polarization axis. When the molecules are well-aligned, this quantity is close to 1, and when they are not, it is closer to 0. It also has a certain periodicity, since



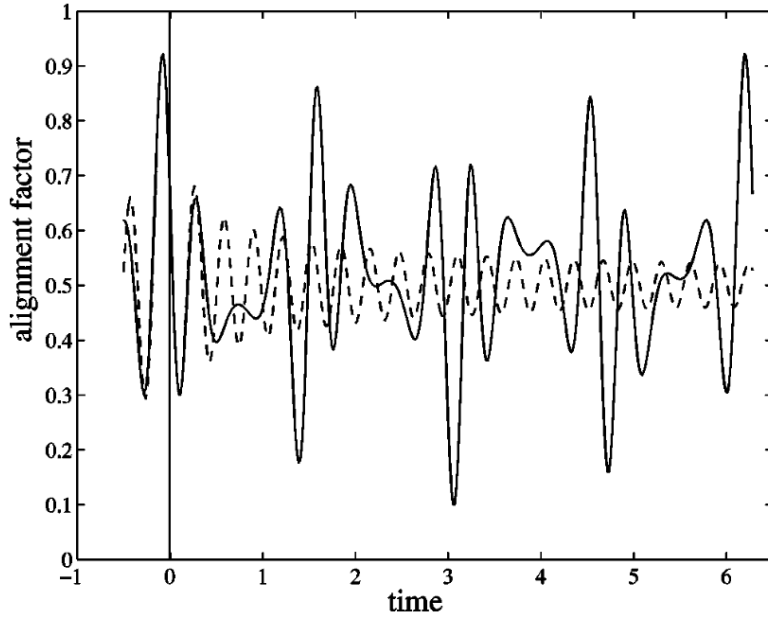


Figure 2.5: The alignment of a molecule as a function of time in the case of non-adiabatic alignment. The alignment factor is  $\langle 1 - \cos^2 \theta \rangle$ , so the alignment is at its best when the alignment factor is close to zero. This figure shows theoretical results, and is taken from [27]. The calculations are made for a quantum mechanical revival model (solid line), and the dashed line shows results from a classical model. A dimensionless time is used.

$$\langle \cos^2 \theta \rangle = \langle \Psi(t) | \cos^2 \theta | \Psi(t) \rangle = \sum_{K', K} c_{K'}^* c_K e^{i(E_{K'} - E_K)t} \langle K' | \cos^2 \theta | K \rangle. \quad (2.21)$$

This is a Fourier series where the terms have different periodicities,

$$\frac{2\pi}{E_{K'} - E_K} = \frac{T_{\text{rev}}}{K'(K' + 1) - K(K + 1)}. \quad (2.22)$$

These are fractions of the revival time, so  $\langle \cos^2 \theta \rangle$  will be periodic with the period  $T_{\text{rev}}$ . An example of a revival in  $\langle \cos^2 \theta \rangle$  is shown in figure 2.5. The alignment factor on the vertical axis is defined as  $\langle 1 - \cos^2 \theta \rangle$ , which means that the best alignment corresponds to an alignment factor of zero. In the figure a lot of different oscillations are seen on top of each other. They stem from the many waves in (2.21) with different periods. At some points in time, the alignment is much better than at other times, but it is only present for a short time, for instance at  $t \approx 3$ .

What has been described in this section so far is how to achieve alignment. Molecules can also be oriented, but then one has to combine the laser field with a static electric field [15]. The theory behind orienting molecules will not be discussed in this thesis, since we will only be concerned with aligning molecules.

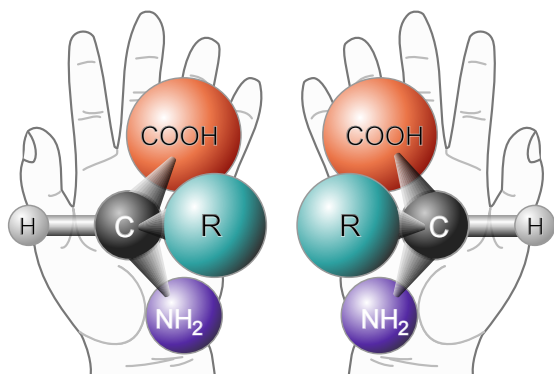


Figure 2.6: The two enantiomers of a simple chiral molecule, a carbon atom with four different groups attached to it. This example shows a generic amino acid. The stereogenic center is the carbon atom. The figure is taken from the homepage [en.wikipedia.org/wiki/Chirality](http://en.wikipedia.org/wiki/Chirality)

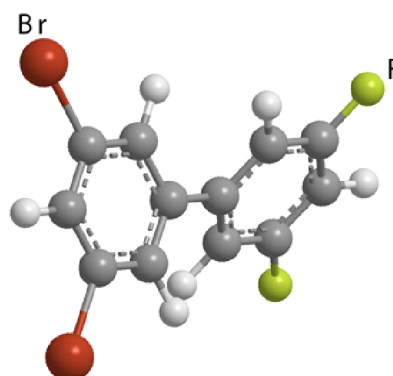


Figure 2.7: Biphenyl molecule with two fluorine and two bromine substituents. The stereogenic axis is the axis of the chemical bond that connects the two phenyl rings. This figure is taken from [26]. The molecule is axially chiral, and it is the  $R_a$  enantiomer that is shown here.

## 2.5 Chiral molecules and deracemization

The molecules used in [1, 2, 3] are examples of *chiral* molecules, and that property will play a major role in some of the later discussions, particularly in chapter 9. This section is intended for a reader unfamiliar with the concept of chirality and deracemization.

A molecule is said to be *chiral* when it cannot be superposed onto its mirror image, like the human hand. This is the case if the molecule includes an atom that has four different groups attached to it, see figure 2.6. Two mirror images of chiral molecules are called enantiomers, and they are examples of stereoisomers, molecules that differ only in the orientations of their atoms in space. The chiral molecule in figure 2.6 has point chirality, meaning the focus of the chirality is a point, namely the carbon atom. This point is called the stereogenic center.

There are other types of chirality, though. One is axial chirality, where the molecule does not contain a stereogenic center, but a stereogenic axis is the focus of chirality instead, see [28]. Biphenyls are examples of axially chiral molecules. They consist of two phenyl rings and can have different substituents instead of some of the hydrogen atoms. An example of a biphenyl is shown in figure 2.7. A phenyl ring is a cyclic group of atoms with the structure  $C_6H_5$ , where the six carbon atoms are bonded together in a hexagonal planar ring. It is an aromatic structure, meaning that the p-orbitals of the carbon atoms combine to yield a circular, delocalized orbital covering all six carbon atoms. The bonds between the carbon atoms are not alternating single and double bonds, as would be the simple picture. Instead, they are all equally strong. This makes the structure more stable. From figure 2.7, one may note that the two rings are twisted away from each other, due to the fact that the electron clouds of the hydrogen atoms on the two different rings repel each other. This is called steric repulsion. The reason why the rings are not  $90^\circ$  from each other, is that the creation of two delocalized orbitals next to each other makes it favourable for these orbitals to be parallel [29]. The enantiomer seen in figure 2.7 is called  $R_a$ , and its mirror image is called  $S_a$ . A rotation of approximately  $90^\circ$  of one of the

phenyl rings about the stereogenic axis, will turn the  $R_a$  into its mirror form  $S_a$ . This means that biphenyls can rotate about the stereogenic axis to move from one enantiomer to another. There will be an energy barrier related to this rotation, because the structure with parallel rings is not energetically favoured.

Chiral chemical compounds that are synthesized from non-chiral starting reagents are racemic, i.e. there is a 50:50 mixture of enantiomers. To obtain a non-racemic compound, one has to go through a process of *deracemization*. This process is very desirable in many cases, because the different enantiomers may possess different properties. This includes medical drugs that are often chiral molecules. One example of a chiral molecule of medical importance is vitamin C; ascorbic acid. Only one of the stereoisomers is identical to the natural vitamin C, and another stereoisomer (erythorbic acid) is not effective against scurvy as vitamin C [30]. To obtain deracemization, one normally uses chemical synthesis with catalysts, but it would also be interesting to be able to achieve it with ultrashort laser pulses. Then, the reaction could be studied in a time-resolved manner, and that would lead to a better understanding of the process.

Racemization will occur at room temperature for many biphenyl compounds, because the energy barrier for rotating through the co-planar geometry is not very large; about 75 meV, as will be seen later in this thesis. Since the average kinetic energy of molecules at room temperature is 1/40 eV, there will be some molecules with a high enough energy to change from one enantiomer into the other. It is therefore necessary to cool the molecules if one wants to study the process of deracemization, because otherwise the two enantiomers will be equilibrated thermally.

For most molecules the energy barrier that has to be crossed to obtain deracemization is significantly larger than in biphenyl compounds. Thermal equilibration is not possible for these molecules. This means that the required energy is much larger than what an ultrashort laser pulse can apply without destroying the molecule.

## 2.6 Density matrix formalism: Mixed states in a molecular gas

The experiments [1, 2, 3] that are studied in this thesis are using molecules in the form of a gas; a molecular beam. The quantum state of such a gas of molecules is investigated in this section, and for that purpose we need the density matrix formalism.

The molecules in a molecular gas are in a thermal ensemble at a finite temperature, meaning that they can interact with each other. Because of that, there will be molecules occupying many different states. When we do measurements on the system, we do not know which state is measured, just as in the case of a classical gas. In other words, there is a classical uncertainty in our system, and we have to treat it statistically. The initial state of the molecular system is an example of a *mixed state*.

Another example of a mixed state is a system that has a classical probability  $p$  of being in state  $|1\rangle$  and  $1 - p$  of being in state  $|2\rangle$ . The expectation value of an operator  $A$  in such a state is

$$\langle A \rangle_{\text{mixed}} = p \langle 1|A|1\rangle + (1 - p) \langle 2|A|2\rangle. \quad (2.23)$$

For a superposition  $|b\rangle = \sqrt{p}|1\rangle + \sqrt{1-p}|2\rangle$  with a probability  $p$  of being in state  $|1\rangle$  and  $1 - p$  of being in state  $|2\rangle$ , the expectation value of  $A$  is

$$\langle A \rangle_{\text{pure}} = \langle b|A|b\rangle = p \langle 1|A|1\rangle + (1 - p) \langle 2|A|2\rangle + \sqrt{p}\sqrt{1-p} (\langle 1|A|2\rangle + \langle 2|A|1\rangle). \quad (2.24)$$

Since there are two extra interference terms in (2.24), the superposition is not the same as the classical sum. In a classical sum one can just add the expectation values, but in quantum physics it is the state vectors that must be added. The states  $|1\rangle$ ,  $|2\rangle$  and  $|b\rangle$  are examples of *pure states*. A pure superposition is called a coherent sum, whereas a mixed state is called an incoherent sum. In other words, a mixed state is an incoherent mixture of different pure states.

One can actually show that a mixed state cannot be described by a single state vector, meaning that there is no state vector  $|a\rangle$  such that the expectation value of an operator  $A$  is  $\langle a|A|a\rangle$ . For a mixed state, the expectation value of  $A$  can instead be written as

$$\langle A \rangle_{\text{mixed}} = \text{Tr}[\rho A], \quad (2.25)$$

where the symbol  $\text{Tr}[\dots]$  means taking the trace of an operator (see [31]). The definition of the trace of an operator  $A$  is

$$\text{Tr}[A] = \sum_n \langle n| A |n\rangle, \quad (2.26)$$

where  $\{|n\rangle\}$  is a complete basis. The trace is independent on the choice of basis. The operator  $\rho$  in (2.25) is called the *density operator*. For a mixed state with probability  $P_i$  of being in state  $|i\rangle$ , the density operator is

$$\rho = \sum_i P_i |i\rangle \langle i|. \quad (2.27)$$

The expectation value found in (2.25) is in fact an average over the ensemble, where each state  $|i\rangle$  is weighted by the probability  $P_i$ .

This section showed that the density matrix formalism can be used to describe a system with a classical uncertainty, for instance a gas of molecules.

Since the expectation value of an observable can be calculated from the density matrix, one can actually determine the time evolution of the expectation value by looking at the time evolution of the density matrix. This is not an approach that will be followed in this thesis. We have other ways of determining the time evolution of our system. The density matrix formalism is just needed to describe the state of the molecular system.

The precise initial state of the molecular system of interest in this thesis will be described in detail in sections 3.2 and 5.6 and chapter 7.

## Chapter 3

# The experiments and a model of the molecule

The experiments in [1, 2, 3], showing that ultrashort pulses can be used to initiate torsional motion in molecules, will be described in this chapter. After that, the main ideas in modelling the experiments will be presented. Finally, the experimental results will be shown and discussed.

### 3.1 Description of the experiments

In the group of Henrik Stapelfeldt at the chemistry department of Aarhus University, the torsion of biphenyl-like molecules has been studied experimentally, as shown in a series of papers [1], [2] and [3]. The first two papers describe an experiment on 3,5-difluoro-3',5'-dibromobiphenyl (DFDBrBPh), which is a biphenyl molecule with two bromine and two fluorine substituents. The molecule can be seen in figure 3.1 and will be discussed further in the next section. The experiment in these papers will be described first. The third paper shows results of an experiment that was conducted somewhat differently on the molecule 3,5-difluoro-3',5'-dibromo-4'-cyanobiphenyl (DFDBrCNBPh). The only difference between the two molecules is that DFDBrCNBPh has a cyano-group ( $-\text{C}\equiv\text{N}$ ) instead of the hydrogen atom to the left in figure 3.1. This experiment will be described afterwards.

The experiment in [1, 2] involves focusing three short laser pulses onto a very cold gas of DFDBrBPh. Each of the lasers play a specific role in the experiment.

The first laser is a linearly polarized nanosecond pulse ( $\tau = 9 \text{ ns}$ ,  $\lambda = 1064 \text{ nm}$ ,  $I = 7 \times 10^{11} \text{ W cm}^{-2}$ ) that aligns the molecules along the axis of its polarization. This pulse is called the *alignment pulse*. It is the most polarizable axis (MPA) of the molecules that is aligned; the axis that has the bromine ring at one end and the fluorine ring at the other end as shown in figure 3.1. This axis is also the stereogenic axis.

The second laser is a linearly polarized femtosecond pulse which is shorter and much more intense than the first pulse ( $\tau = 700 \text{ fs}$ ,  $\lambda = 800 \text{ nm}$ ,  $I = 5 \times 10^{12} \text{ W cm}^{-2}$ ). It is polarized perpendicular to the alignment pulse. This pulse is short enough to act non-adiabatically on the molecule, and it is this pulse that kicks the molecule into torsional motion. It is therefore called the *kick pulse*.

The role of the third pulse, which we will call the *probe pulse* ( $\tau = 25 \text{ fs}$ ,  $\lambda = 800 \text{ nm}$ ,  $I = 2 \times 10^{14} \text{ W cm}^{-2}$ ), is to turn the molecules into ionic fragments that can be projected onto a two-dimensional detector by using a weak static electric field. This pulse is polarized along the same axis as the alignment pulse. The pulse is so intense that it simply rips the molecules apart, and this allows detection of the position of the  $\text{F}^+$  and  $\text{Br}^+$  ions in the form of two-

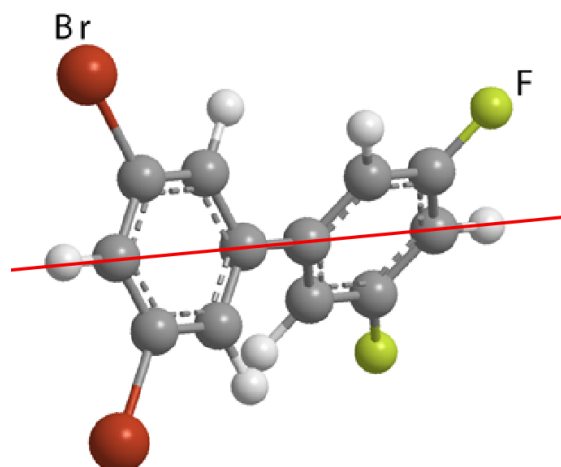


Figure 3.1: The molecule 3,5-difluoro-3',5'-dibromobiphenyl (DFDBrBPh). The most polarizable axis (MPA), which is the same as the stereogenic axis, is marked with red in this figure. This figure is taken from [26]. White atoms are hydrogen, grey atoms carbon, yellow are fluorine, and red are bromine.

dimensional ion images. These images show the position of the two phenyl rings in the plane perpendicular to the alignment pulse polarization, because the  $F^+$  and  $Br^+$  ions will move in the plane of the phenyl ring after the fragmentation of the molecule. The detection technique used here is called Coulomb explosion [32]. By varying the time delay between the kick pulse and the third pulse, time-resolved measurements can be conducted, and because the third pulse is so short, a very good resolution is obtained.

The paper [3] describes an experimental procedure that is slightly changed from the above. Now the first laser pulse is not linearly polarized, but elliptically polarized. That gives rise to 3D alignment of the molecules, as described in section 2.4. The idea behind this change is to improve the torsional control, as we will see in chapters 5 and 8. Another change is the use of a different molecule, DFDBrCNBPh. This new molecule is not too different from DFDBrBPh, since a cyano-group is just added instead of the hydrogen atom to the left in figure 3.1. The only important change is that DFDBrCNBPh has a larger dipole moment than DFDBrBPh. This fact is used to improve the degree of 3D alignment by selecting the most localized quantum states from the rest with an electrostatic field. The technique is called quantum state selection [33].

The main result of these experiments is that it is possible to probe the torsion of molecules using ultrashort lasers, and the torsional motion can be monitored with a very high time resolution. The results will be discussed in detail in section 3.3.

## 3.2 Model of the molecule

The molecule in focus of the first two papers mentioned above is DFDBrBPh, which is shown in figure 3.1. This is a biphenyl-like molecule that consists of two phenyl rings, one with two bromine substituents and one with two fluorine substituents. As described in section 2.5, this molecule is twisted away from the co-planar geometry. Without any lasers present, the

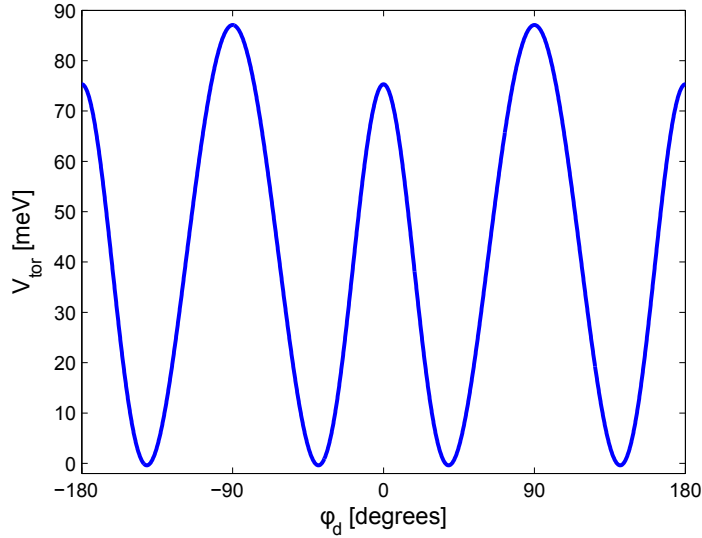


Figure 3.2: The torsional potential of DFDBrBPh in meV. This figure shows a fit to the calculations in [2]. The method used to calculate it is described in further detail in [34]. Note that the torsional barrier is about 75 meV.

interaction between the two phenyl rings is given by a *torsional potential*. This potential only depends on one variable, and that is the angle between the two rings, the *dihedral angle*  $\phi_d$ . The torsional potential has been calculated by quantum chemists at several values of  $\phi_d$ , and the results are shown in [2]. The method used in the calculations is discussed more thoroughly in [34]. By fitting the torsional potential found in [2] to a sum of cosines, one can find

$$V_{\text{tor}}(\phi_d) = a \cos(4\phi_d) + b \cos(2\phi_d) + d \cos(6\phi_d) + e \cos(8\phi_d) + c, \quad (3.1)$$

where

$$\begin{aligned} a &= 0.001430 \pm 0.000006 \text{ a.u.} & b &= -0.0004726 \pm 0.0000060 \text{ a.u.} \\ d &= 0.0002561 \pm 0.0000060 \text{ a.u.} & e &= 0.00004004 \pm 0.00000602 \text{ a.u.} \\ c &= 0.001514 \pm 0.000004 \text{ a.u.} \end{aligned} \quad (3.2)$$

The  $\cos(4\phi_d)$ -term is most dominant, and the other terms are corrections. The unit of  $\phi_d$  should be radians when these coefficients are used in calculations, but when discussing the physics we will often be using degrees, since this is the tradition. This potential can be seen in figure 3.2, where it is noticed that there are four minima between  $-180^\circ$  and  $180^\circ$  at almost the same energy. Each of these minima correspond to a preferred angle of the field-free molecule, for instance at  $39^\circ$ . If we were to find eigenstates of a Hamiltonian including this potential, we would expect that the four states with the lowest energy were almost degenerate, since there would be one state for each well.

The molecule used in the experiment behind the third paper [3] is DFDBrCNBPh, which is identical to DFDBrBPh except for a cyano group attached to the bromine-end. A cyano group is a carbon atom with a triple bond to a nitrogen atom ( $-\text{C}\equiv\text{N}$ ). The main advantage of this

molecule is that it has a larger permanent dipole moment, which allows the experimentalists to get a better alignment of the molecules [33]. The torsional potential for this molecule has not been calculated, but with small corrections, the potential of DFDBrBPh can be used, as will be explained towards the end of this section.

Now, we have described the molecules used in the two experiments [1, 2] and [3], respectively. The time has come to discuss a model for these experiments. As we will see later, it is possible to use the same model for both experiments. First, a model for the experiment in [1, 2] will be developed, and later we will argue that the same model applies to the experiment in [3]. The model developed here will be continued in one direction in chapter 5, and in another direction in chapters 6 and 7.

### Modelling the experiment in [1, 2]

The experiment in [1, 2] can be described using two sets of coordinate systems. A laboratory fixed frame  $(X, Y, Z)$  specifies the polarization axes of the lasers, and a molecular fixed frame  $(x, y, z)$  is given by the orientation of the molecule DFDBrBPh. The  $Z$ -axis is chosen to be along the polarization of the linearly polarized alignment pulse, and the  $X$ -axis along the polarization of the kick pulse. This specifies the laboratory fixed frame. The molecular frame is given by the choice of the  $z$ -axis along the stereogenic axis and the  $x$ -axis along the phenyl ring with the bromine substituents. All models used in this thesis are based on the assumption that the first laser pulse completely 1D-aligns the molecules. Experimental results show that this is a fairly good approximation, as we will see in the next section. This means that the  $Z$ - and  $z$ -axes are aligned. The position of the axes can be seen in figure 3.3. Another assumption to be made is that the only accessible normal mode is torsion, meaning that the rings will only rotate about the stereogenic axis. This assumption has been justified elsewhere by a normal mode analysis [2]. With these two assumptions, we can describe the system as two rigid rings that can rotate about the stereogenic axis, which is pointing along the polarization of the first pulse. There will be an interaction between the two rings, which is given by the torsional potential. Such a system can be described using only two coordinates, for example the angles of the two rings with respect to the  $X$ -axis. These coordinates are called  $\phi_1$  and  $\phi_2$  for the bromine and fluorine ring respectively. The dihedral angle  $\phi_d$ , which is the angle between the rings, is now given as  $\phi_d = \phi_1 - \phi_2$ . Figure 3.3 illustrates the angular coordinates and their relation the axes. The angles  $\phi_1$  and  $\phi_2$  are obviously  $2\pi$ -periodic, but since each of the two rings are symmetric about the stereogenic axis, they comply with a symmetry that is even more strict. They are in fact both  $\pi$ -periodic, but in this thesis, only  $2\pi$ -periodicity will be considered. It is more general, which is good if this model is to be used on other molecules.

The system will be described quantum mechanically by a Hamiltonian containing both kinetic energy and potential energy terms. The kinetic energy terms will be discussed first. The two rings will have different moments of inertia for rotation about the stereogenic axis, since they have different masses. This difference will lead to different kinetic energies for the two rings. Classically, the kinetic energy of a rotating body is

$$T = \frac{1}{2}I\omega^2 = \frac{L^2}{2I}, \quad (3.3)$$

where  $L$  is the angular momentum and  $I$  the moment of inertia. In quantum mechanics, the angular momentum operator is

$$L = -i\frac{\partial}{\partial\phi} \quad (3.4)$$



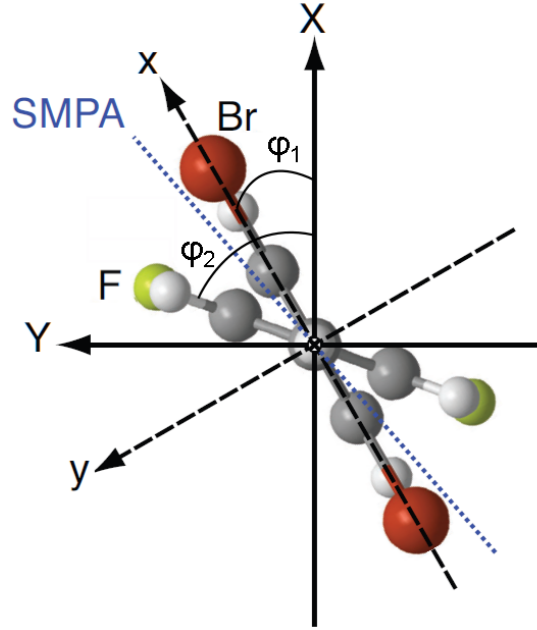


Figure 3.3: A two-dimensional illustration of DFDBrBPh, seen along the stereogenic axis (see figure 3.1). The Z- and z-axes are both perpendicular to the paper, because the molecule is aligned by the alignment pulse. The two rings are rigid, but may rotate with respect to each other if an external field is applied. The angles of the two rings are  $\phi_1$  for the bromine ring and  $\phi_2$  for the fluorine ring, both measured with respect to the polarization axis of the kick pulse, which is the X-axis. Notice the signs of the angles in this figure. Positive angles are to the left of the X-axis, which is towards the Y-axis and thus the usual positive direction for angles. This figure is from [2].

in atomic units, where  $\phi$  is the angle in the plane perpendicular to the axis about which the object is rotating. The angles  $\phi_1$  and  $\phi_2$  are exactly such angles for the two rings. By inserting (3.4) into (3.3), it is found that

$$T = -\frac{1}{2I} \frac{\partial^2}{\partial \phi^2}. \quad (3.5)$$

This means that the kinetic energy terms in the Hamiltonian for the two rings can be written as

$$T = -\frac{1}{2I_1} \frac{\partial^2}{\partial \phi_1^2} - \frac{1}{2I_2} \frac{\partial^2}{\partial \phi_2^2}, \quad (3.6)$$

where  $I_1$  and  $I_2$  are the moments of inertia of the bromine ring and fluorine ring respectively. By using classical mechanics, it can be found that  $I_1 = 8911925$  a.u. and  $I_2 = 1864705$  a.u. [2].

Now it is time to look at the potential energy terms. There will definitely be a term for the torsional potential corresponding to an interaction between the two rings. This term is given by (3.1). There should also be a potential energy term for the alignment laser, because this two-

dimensional model only makes sense when the molecules are aligned. We will neglect this, though, because the laser is not very intense ( $7 \times 10^{11} \text{ W cm}^{-2}$ ). It only perturbs the torsional potential slightly, and therefore we can ignore it. The second pulse is much more intense ( $5 \times 10^{12} \text{ W cm}^{-2}$ ), and this pulse has a potential that is comparable in strength to the torsional potential. The third pulse is ignored as well, since it is only used for measurement purposes. Because the kick pulse is much shorter than the alignment pulse, there will be alignment before the kick pulse hits, and that alignment will persist for a long time compared to the length of the kick pulse. This means that before the kick pulse hits, the alignment pulse has aligned the molecules but not deformed the torsional potential that much. In that case, the system can be described by the Hamiltonian

$$H = -\frac{1}{2I_1} \frac{\partial^2}{\partial \phi_1^2} - \frac{1}{2I_2} \frac{\partial^2}{\partial \phi_2^2} + V_{\text{tor}}(\phi_1 - \phi_2). \quad (3.7)$$

This Hamiltonian corresponds to two rigid rotors that interact via the potential  $V_{\text{tor}}(\phi_1 - \phi_2)$ . When the kick pulse hits, another potential  $V_{\text{kick}}(\phi_1, \phi_2, t)$  will be included in the Hamiltonian so that it becomes

$$H_{\text{kick}} = -\frac{1}{2I_1} \frac{\partial^2}{\partial \phi_1^2} - \frac{1}{2I_2} \frac{\partial^2}{\partial \phi_2^2} + V_{\text{tor}}(\phi_1 - \phi_2) + V_{\text{kick}}(\phi_1, \phi_2, t). \quad (3.8)$$

The kick pulse is so short and intense that its actions on the molecule can be treated non-adiabatically, see section 2.4. It kicks the molecule into a wave packet of vibrational and rotational states, and then the two rings starts to rotate, which initiates both rotational and torsional motion. The rotational excitation assures that the pulse initiates non-adiabatic 3D alignment of the molecules, see section 2.4. One axis is of course already aligned because of the alignment pulse. To have 3D alignment, another axis must be aligned, and this axis will be the SMPA of the molecule. The SMPA is seen in figure 3.3, and it will be aligned to the polarization axis of the kick pulse, the X-axis.

The equation to be solved is the time-dependent Schrödinger equation corresponding to the Hamiltonian (3.8). This is done by starting in an initial state and propagating the equation forward in time in small steps. In general the initial state is given by the density operator (see section 2.6)

$$\rho = \sum_i P_i |i\rangle \langle i|, \quad (3.9)$$

where  $|i\rangle$  is a set of pure states. This quantity can be expanded in any complete basis, and a natural choice would be energy eigenstates. The calculations are started before the kick pulse hits the molecule, so the initial state is governed by the Hamiltonian (3.7). The density operator (3.9) can thus be expanded in eigenstates of this Hamiltonian. In case of a very cold gas of molecules, an approximation can be made. Because of the low temperature, the initial state can actually be described by the ground state of (3.7) alone. Then things become less complicated, because the density matrix (3.9) simply corresponds to a pure initial state. There is however a problem with the ground state of (3.7), and that problem is degeneracy. The four lowest states are almost degenerate, so even at low temperatures four states may be populated. We therefore stick to a mixed initial state described by a density matrix (2.27) with four terms for now. In section 5 and 7 these four terms will be reduced to one by making an additional approximation.

This is as far as we will go with modelling of the experiment in [1, 2] in this chapter. Now we turn to the experiment in [3].

### Modelling the experiment in [3]

It is time to test whether the theory can be applied to the experiment in [3]. In the theory above, it was assumed that the 1D alignment laser achieved perfect alignment of the molecules. In the new experiment in [3], the first pulse initiates 3D alignment, but in our modelling we will not assume that the 3D alignment is perfect. We will stick to the assumption that perfect 1D alignment is achieved, such that the two-dimensional model of two rigid rotors can be used. The alignment of another axis can be included in the model by choosing an initial state that is localized in  $\phi_1$  and  $\phi_2$ , meaning that it is rotated by a certain angle with respect to the X-axis. Such an initial state is not clearly seen to be in correspondence with (3.9) and the discussion below that equation, but the approach may be attempted anyway. This will be discussed further in chapter 7.

Another difference between the two experiments is the molecule itself. In the experiment in [3], DFDBrCNBPh was used instead of DFDBrBPh. This means that the torsional potential might be different, and it is very hard to calculate precisely [34]. Since the molecules are very cold, only a few states at the bottom of the wells in the torsional potential will be occupied. This means that the exact shape of the potential is not so important. The most important thing is the position of the minima in the potential, and they are different for the two molecules. For DFDBrBPh there is a minimum at about  $\phi_d = 39^\circ$ , but for DFDBrCNBPh, that minimum is  $0.9^\circ$  lower [3]. This means that a curve of  $\phi_d$  as a function of time can be calculated by simply using the torsional potential of DFDBrBPh, and then, in the end, it should be lowered by  $0.9^\circ$ . This is a lot easier than calculating the torsional potential for DFDBrCNBPh.

There is another reason why the torsional potentials of the two molecules do not differ significantly. The bromine ring is much heavier than the fluorine ring, so the torsional motion will mainly be caused by movement of the fluorine ring. The cyano group in the molecule used in [3] is attached to the bromine ring, and since it does not move much it is not expected to make much of a difference.

In conclusion, the model intended for the experiment in [1, 2] can also be applied to the experiment in [3]. The only significant difference is the initial state to be used. For [1, 2] we use a 1D aligned initial state, but for [3] a 3D aligned initial state is used. In chapter 5, the model introduced in this chapter will be continued in a direction towards a 1D model, and in chapter 6 and 7 it will be used as a 2D model.

### 3.3 Experimental results

The first part of this section will treat the experimental results of the experiment from [1, 2]. After that, the results of [3] will be discussed. The ion images obtained in [1, 2] are shown in figure 3.4 (a) at different times for both  $F^+$  and  $Br^+$ . The kick pulse peaks at  $t = 0$  and has a length of 0.7 ps, and it is polarized in the horizontal direction of the images in figure 3.4 (a). To verify the quality of the 1D alignment obtained by the alignment pulse, we note that there are no  $F^+$  ions at the center of the images. If there was no alignment, the fluorine ions would be seen everywhere on the 2D image. It is concluded that the molecules are experiencing a fairly good degree of alignment at all times, even during the kick pulse and after it has died out. Then the bromine ring should also be aligned, but when looking at the bromine images of 3.4 (a), we see that there are  $Br^+$  ions at the center of the images. This observation can be explained by the fact that bromine is much heavier than fluorine. This means that the bromine ion achieves a smaller velocity than the fluorine in the Coulomb explosion process and does not move away from the center of the detector as fast.

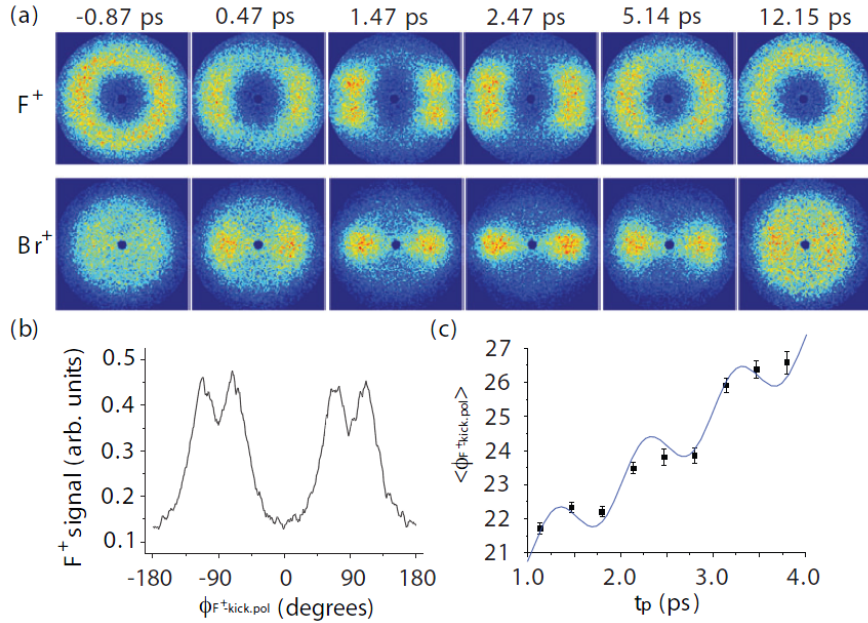


Figure 3.4: This figure shows experimental results, and it is taken from [2]. (a) Ion images of the fragments  $F^+$  and  $Br^+$ . The images show the position of the ions in the plane perpendicular to the polarization of the alignment pulse. The kick pulse is polarized horizontally in these images, and it peaks at  $t = 0$ . (b) Angular distribution of  $F^+$  ions at  $t = 1.47$  ps, which is found by doing a radial integration of the corresponding  $F^+$  ion image. Note that there is an error in (b). The horizontal axis has been moved by  $90^\circ$  compared to (a). (c)  $\langle \phi_{F^+ \text{kick, pol}} \rangle$  as a function of time for the times where a four-dot structure is visible in the  $F^+$  ion image.  $\phi_{F^+ \text{kick, pol}}$  is the same as  $\phi_2$  in figure 3.3. The curve is a fit of the sum of a linear and a harmonic function to the experimental data.

At  $t = -0.87$  ps the image of  $F^+$  is almost circularly symmetric. This means that there is no preferred direction in the plane perpendicular to the alignment pulse polarization, or, in other words, that there is 1D alignment. The reason for the small deviation from circular symmetry is that the kick pulse has a non-zero value at  $t = -0.87$  ps. When the kick pulse hits, initiation of 3D alignment is observed as the circular symmetry is broken. At  $t = 1.47$  ps, the ions have localized near the polarization axis of the kick pulse. The  $F^+$  image shows a clear four-dot structure, which means that the rings with fluorine on the molecules in the gas will be localized around four angles. These are approximately  $28^\circ$ ,  $-28^\circ$ ,  $152^\circ$ , and  $-152^\circ$  with respect to the kick pulse polarization. The bromine image at  $t = 1.47$  ps does not show the same four-dot structure, but that is because the angles are such that two spots coincide too much to be resolved by these measurements. The angles of the two rings correspond to the ones seen in figure 3.3;  $\phi_1$  for  $Br^+$  and  $\phi_2$  for  $F^+$ . These ion images are consistent with 3D alignment of the molecules along the kick pulse polarization axis, the X-axis in figure 3.3. The reason is that the molecules will have dihedral angles corresponding to the minima of the torsional potential (3.1), for instance  $\phi_d = \pm 39^\circ$ . If  $\phi_2$  is  $28^\circ$  and  $\phi_d$  is  $-39^\circ$ , it fits with  $\phi_1$  being  $-11^\circ$ , which could very well correspond to one of the peaks in the bromine ion image

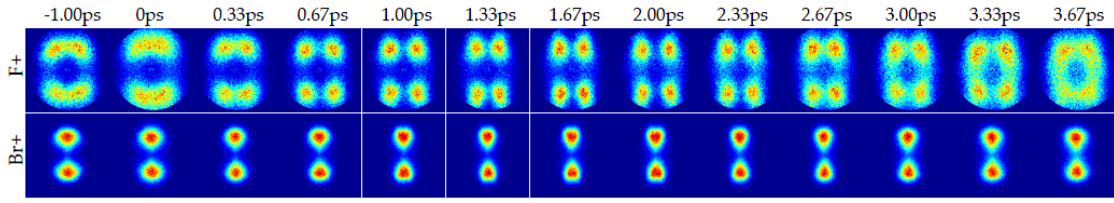


Figure 3.5: This figure shows the ion images of the experiment in [3] at relatively small times. The kick pulse peaks at  $t = 0$ . Note that the polarization axis of the kick pulse is vertical in this figure, in contrast to figure 3.4.

at  $t = 1.47$  ps. In a similar way,  $\phi_2 = -28^\circ$  and  $\phi_1 = 11^\circ$  corresponds to  $\phi_d = 39^\circ$ . To account for the last two of the four peaks, it is noted that the geometry of the system is the same if the angle of one of the rings is changed by  $180^\circ$ , for example from  $28^\circ$  to  $-152^\circ$ .

A look at the ion images for  $t = 12.15$  ps shows that the 3D alignment is lost at larger values of  $t$ , where the molecules will simply be 1D aligned. The delocalization of these images occurs faster for  $\phi_1$  than for  $\phi_2$ .

Figure 3.4 (b) shows the angular distribution of  $F^+$  ions at  $t = 1.47$  ps. It is obtained by radially integrating the ion image, and the result also shows the four-dot structure.

If the ion images at  $t = 2.47$  ps are studied, one notices that the bromine ring increases the degree of localization around the  $X$ -axis. If this was to be consistent with an unchanged dihedral angle, the ion image of  $F^+$  should show a clear four-dot structure like at  $t = 1.47$  ps, but with a larger distance from the dots to the horizontal axis. Instead, the image becomes more blurry, and the conclusion is that  $\phi_d$  does in fact change. It is possible to quantify if there is a characteristic oscillation in  $\phi_d$  by looking at  $\phi_2$  alone. The fluorine ring is by far the lightest of the two rings, which means that most of the movement will be done by this ring. The expectation value of  $\phi_2$  is shown in figure 3.4 (c) as a function of time; experimental results as well as a fit to them. The fit is the sum of a linear and a harmonic function. The linear part is there because the molecules rotate away from the SMPA, since the kick pulse is short and non-adiabatic. On top of that, there is an oscillation in  $\phi_2$ , which also means an oscillation in  $\phi_d$ . The amplitude can be estimated to  $\sim 0.6^\circ$  and the period to  $\sim 1$  ps. This oscillation shows that it is actually possible to initiate torsional motion by using ultrashort laser pulses, and that is the main result of the experiments described in [1, 2].

For the experiment of [3], the method has changed, as described in section 3.1. Since there is already 3D alignment before the kick pulse hits, the ion images will not be circularly symmetric, even before  $t = 0$ , as seen in figure 3.5. Note that the polarization axis of the kick pulse has been rotated  $90^\circ$  in this figure compared to figure 3.4 (a). The experimentalists managed to improve the quality of the ion images by changing the polarization axis of the probe pulse and making the sample of molecules more clean. In the experiment of [1, 2], the probe pulse was polarized in the  $Z$ -direction, but here it is polarized in the  $X$ -direction, the polarization direction of the kick pulse. The improvement might be caused by the probe pulse preferring to ionize the molecules that have the SMPA closely aligned to the  $X$ -axis.

As in the experiments of [1, 2], it is possible to see an oscillation in  $\phi_2$ , i.e. an oscillation of the fluorine ring (see figure 3.6). The increased precision makes it possible to estimate the oscillations of the bromine ring as well, even though the  $Br^+$  images do not show four dots. In fact there are still only two dots, but now it can be seen that the width of the  $Br^+$  images oscillates as a function of time. This oscillation is used to estimate how  $\phi_1$  oscillates as a

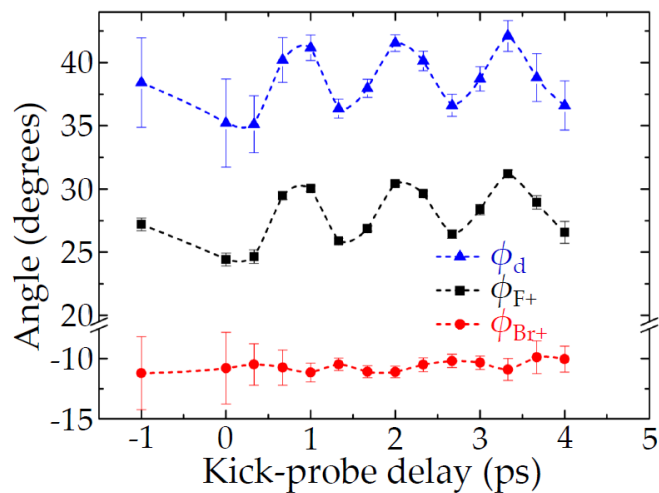


Figure 3.6: Experimental measurements of  $\phi_d$  (blue),  $\phi_2$  (black), and  $\phi_1$  (red) as functions of time. These results are from [3], which is for a 3D aligned initial state and uses the molecule DFDBrCNBPh. Note that the sign convention for  $\phi_d$  in this graph is different from the convention used in the rest of the thesis.

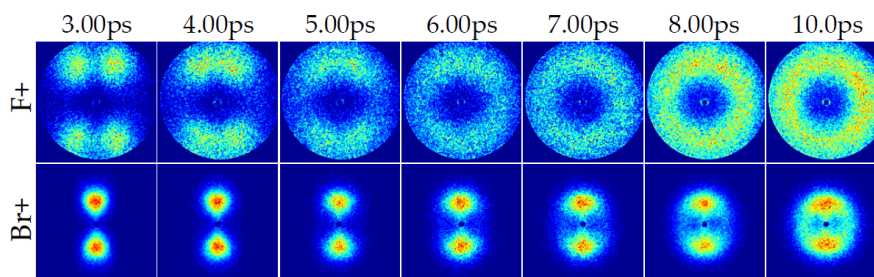


Figure 3.7: Ion images taken from [3] at different times. The times are later than the ones in figure 3.5. See the caption of figure 3.5 for further info.

function of time, and combining this with the oscillation of  $\phi_2$ , one can find the oscillation in  $\phi_d$ . The oscillations can be seen in figure 3.6, and the first thing to note is that the amplitude is larger than the  $\sim 0.6^\circ$  that was found in the first experiment. It is in fact  $3^\circ$ , which means that control of the torsional motion has improved significantly. The main cause of the improvement is probably the initial 3D alignment, and this idea will be investigated in further detail in the chapters to come. The period of the oscillation is 1.25 ps.

In figure 3.7, ion images at times above 3 ps are shown. One can observe that the 3D alignment disappears at larger times; the ion images experience delocalization. On top of that, the broadening is much slower for bromine ( $\phi_1$ ) than for fluorine ( $\phi_2$ ). This was also seen in figure 3.4 regarding the experiment in [1, 2]. One more thing to note is that there are still no ions at the center of the images, meaning that there is 1D alignment at large values of  $t$ . Initially, there was some degree of 3D alignment, which was improved by the kick pulse, but at later times, there is no 3D alignment.

The conclusion of these experiments is that it is possible to initiate torsional motion of biphenyl-like molecules using two short laser pulses. The motion can be measured in a time-resolved manner by using a third pulse. What is needed now is a theory that can reproduce the results and show in which direction future experiments should go.

### 3.4 Summary

In this chapter the experiments designed to obtain control of the torsional motion of biphenyl-like molecules have been presented. The basics of the theoretical model used in this thesis have also been described, and experimental results have been displayed and discussed. The rest of this thesis will be devoted to developing a theory and calculating results that can be compared to these experiments.





## Chapter 4

# Interaction between a non-ionizing laser and a gas of molecules

In the experiments described in [1, 2, 3] there are multiple lasers interacting with molecules (DFDBrBPh or DFDBrCNBPh). As described in section 3.2, we will only be concerned with the potential from one of these lasers, the kick pulse, but we definitely need a theory for that pulse to be able to do any calculations of the dynamics. What we need is a theory for the interaction between the laser and the molecule. Such a theory will be devised in this chapter, and it will be applied to the geometric situation of the experiments. The result is an effective interaction term that corresponds to the kick pulse,  $V_{\text{kick}}(\phi_1, \phi_2, t)$ .

This theory also applies to a general alignment of molecules, which was described in section 2.4.

### 4.1 Qualitative theory

What is sought here is an interaction that can lead to rotation and torsion of the molecule without breaking it into pieces. If the kick pulse could ionize the molecule, this reaction would disturb the control of the molecule, so it will be assumed that the laser does not ionize or dissociate the molecule. The pulses in the experiments are actually chosen such that there is no ionization or dissociation. They are near infrared, which means that each photon has an energy of 1.5 eV. The molecule consists of H, C, F, and Br atoms, which all have ionization energies in the range of 10–20 eV. The molecular ionization potential is expected to be in that region as well and might possibly be a bit higher because the atoms are bound. From [35] it can be estimated that the dissociation energy of the molecule will be  $\sim 100$  kcal/mol, which is  $\sim 4$  eV. We can conclude that the photon energy is far from the ionization potential and dissociation energy of the molecule. With an intensity of  $5 \times 10^{12} \text{ W cm}^{-2}$  or  $2 \times 10^{13} \text{ W cm}^{-2}$  in the two experiments, the kick pulse is not intense enough to do multiphoton ionization or dissociation either. The limit is around  $10^{14} \text{ W cm}^{-2}$ , so the kick pulse is definitely non-ionizing and non-dissociating.

The interaction between a non-ionizing laser pulse and a molecule has been described qualitatively in section 2.4. This description will be continued here and applied to the case where the degree of freedom to be controlled is torsion. In section 2.4, it was found that the interaction between the molecular system and the laser is governed by the polarizability. The interaction will cause the molecule to twist and rotate to minimize the energy, and in our case, the rotation will be about the fixed stereogenic axis. Since the MPA is already aligned with the

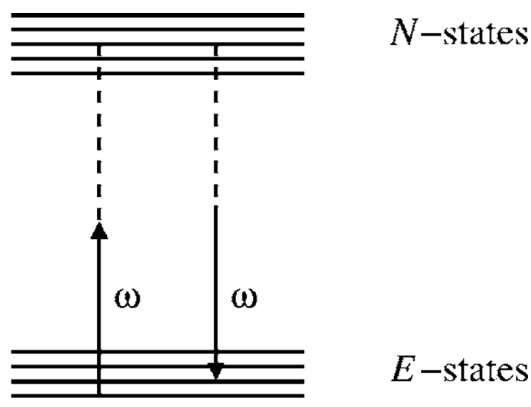


Figure 4.1: A stimulated Raman transition. Absorption of a photon with a frequency  $\omega$  (left arrow) is followed by stimulated emission (right arrow), and the net result is an excitation to an energy level that only has a slightly higher energy than the initial state. For the derivation in this chapter, the laser is assumed to be off resonance with any molecular transition. Then the states can be separated into essential states ( $E$ ) and non-essential states ( $N$ ). The transition described here is between two  $E$ -states, and the  $N$ -states are only used as stepping stones.

polarization of the alignment pulse in our case, the kick pulse will seek to align the SMPA of the molecule with its own polarization (see figure 3.3).

To get an interaction that is governed by polarizability, it turns out that we must focus on two-photon processes. The transition we are interested in is shown in figure 4.1; an absorption of a photon followed by a stimulated emission. The final state is not necessarily the same as the initial state, which means that such a coupling can result in an excitation of the molecule. This is a stimulated Raman process, and it can excite molecules to nearby rovibrational states. It is caused by the broad spectrum of the laser pulse, which means the absorbed and the emitted photon can have different energies. This effect is a coupling between two of the states in the  $E$ -manifold in figure 4.1 via a state in the  $N$ -manifold. The  $E$ -states are close to the the initial state and are called essential states, while the  $N$ -states are far from the initial state and thus called nonessential states. The Raman coupling is of second order in the field, since the field does the first excitation (absorption) and facilitates the de-excitation (stimulated emission).

Notice that the photon energy does not correspond to the energy difference between  $E$ -states and  $N$ -states. It is assumed that the photon energy is not resonant with any molecular transition. Otherwise, there would also be a direct interaction by absorption of a photon. Since the photon energy is smaller than the dissociation energy, it is possible that a rovibrational state is actually resonant with the laser pulse, see figure 2.3. The existence of such a state means that the assumption of non-resonance is not quite fulfilled, but the resonant dipole transition can still be neglected for other reasons: a highly excited rovibrational state will only be populated near the edge of the potential curve given by the electronic energy, and the ground state will only be populated near the center. The reason is that vibrational states can be approximated by harmonic oscillator states, and these states show such behaviour. The Franck-Condon principle tells us that the transition has to happen without changing the position of the nuclei, as seen in figure 4.2, so the direct absorption is not very likely. This has also been argued in [36]. We thus conclude that the dipole transition may be neglected. In the derivations to come, the pulse will

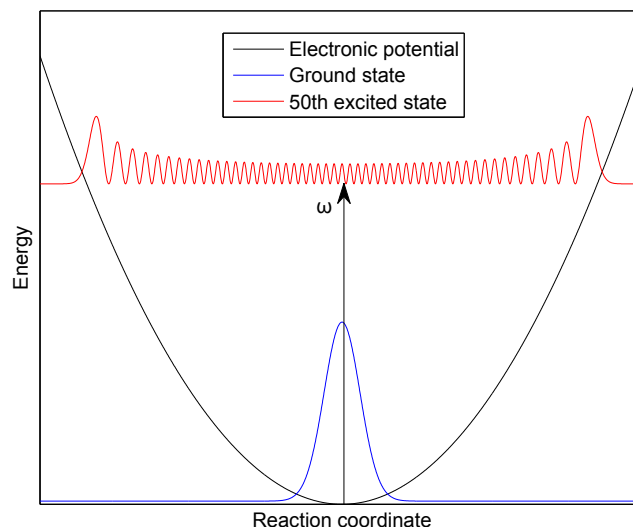


Figure 4.2: The norm squared of the ground state and the 50th excited state for the harmonic oscillator. These states resemble the vibrational states in molecules. A transition between the ground state and a highly excited vibrational state is unlikely because of the Franck-Condon principle. The excitation has to be vertical, and the excited state has almost no population in the middle of the potential well. The result is that the direct first-order coupling between the field and the molecule can be neglected.

be described as being off resonance, because the dipole transition is unimportant. We note that a theory including nearly resonant states has recently become available in the literature [37].

In the next section, the stimulated Raman effect will be studied in further detail. After doing some calculations, it turns out that the higher lying states can be adiabatically eliminated by integrating them out. These higher states will still have some influence, which can be written as a polarizability tensor. The final result is an interaction that depends on polarizability, just as was expected.

## 4.2 Quantitative approach

In this section we will put some more substance into the arguments presented at the end of the previous section. The derivation presented here is based on [38]. Unlike the rest of this thesis, this section will not be in atomic units. This is done to make the derivation clearer. What we want to describe is the interaction between the molecule and the kick pulse. We must remember that we are looking at a Raman coupling, see figure 4.1. The system is described by a Hamiltonian of the form

$$H = H_0 + V(t), \quad (4.1)$$

where  $H_0$  is the Hamiltonian (3.7), and  $V(t)$  is the potential corresponding to the interaction between the molecule and the laser, in this case the kick pulse. In the dipole approximation

and length gauge this potential is

$$V(t) = -\boldsymbol{\mu} \cdot \mathbf{F}(t), \quad (4.2)$$

as described in section 2.2. Here,  $\boldsymbol{\mu}$  is the electric dipole moment operator and  $\mathbf{F}(t)$  is the electric field from the kick pulse. The laser field can be written as

$$\mathbf{F}(t) = \frac{1}{2}eF_0(t) \left( e^{-i\omega t} + e^{i\omega t} \right), \quad (4.3)$$

where  $e$  is the polarization of the laser,  $F_0$  is the pulse envelope, and  $\omega$  is the central frequency of the pulse. This was discussed in section 2.1. This laser pulse will be assumed to be non-ionizing and non-resonant with any molecular transition.

We will assume that we already know a complete set of orthonormal eigenstates for the Hamiltonian  $H_0$ , the Hamiltonian without the kick pulse. These states are written as  $|n\rangle$  and the corresponding energies  $E_n$ , where  $n = (e, \nu, K)$ . This means that the state  $|n\rangle$  corresponds to the molecule being in a state given by the electronic index  $e$ , the vibrational index  $\nu$ , and the rotational index  $K$ . The states  $\{|n\rangle\}$  are orthonormal and form a complete set, which means that any other state of the system can be written as a sum of these states.

To describe what happens when the laser potential is included, we look at the time-dependent Schrödinger equation

$$i\hbar \frac{d}{dt} |\psi(t)\rangle = (H_0 + V(t)) |\psi(t)\rangle. \quad (4.4)$$

Initially, the molecule will be in an incoherent state, as described in section 2.6. This initial state is called  $|\psi(t_0)\rangle$  in this section. When the pulse hits the molecule, the state of the molecule is changed from  $|\psi(t_0)\rangle$  to the full time-dependent state  $|\psi(t)\rangle$ . This state can be described in the basis of eigenstates of  $H_0$ ,

$$|\psi(t)\rangle = \sum_n c_n(t) e^{-i\omega_n t} |n\rangle, \quad (4.5)$$

where  $\omega_n = E_n/\hbar$ . If we substitute (4.5) into (4.4) and project onto  $|n\rangle$ , a few steps of calculation lead us to the following differential equation for the coefficients  $c_n$ :

$$i\hbar \dot{c}_n(t) = \sum_{n'} V_{n,n'}(t) e^{-i(\omega_{n'} - \omega_n)t} c_{n'}(t), \quad (4.6)$$

where  $V_{n,n'}(t) = \langle n|V(t)|n'\rangle$ . Here, we have used that  $\{|n\rangle\}$  is an orthonormal set and that  $H_0|n\rangle = E_n|n\rangle$ .

The goal of the rest of this section is to do some calculations on this expression in the case of a non-resonant laser field. Because the field is non-resonant, one can divide the states into essential ( $E$ ) and non-essential ( $N$ ) states, as was already done in the previous section. The  $E$ -states are denoted by the index  $E = (e_E, \nu_E, K_E)$  and the  $N$ -states by  $N = (e_N, \nu_N, K_N)$ .

We will assume that no  $N$ -states are populated in the initial state, which means that the molecule is initially very cold. This condition is met in the experiments [1, 2, 3]. Another assumption to be used is that there is no coupling between two  $N$ -states, because it is just the Raman coupling we are interested in. The Raman coupling corresponds to a coupling of two  $E$ -states via an  $N$ -state. The following notation will be used:  $|n\rangle$  and  $|n'\rangle$  denotes any state in the basis of eigenstates of  $H_0$ ,  $|E\rangle$  and  $|E'\rangle$  are  $E$ -states and finally  $|N\rangle$  is an  $N$ -state.

There are two ways to proceed now: One can either look at (4.6) when  $|n\rangle$  is in the  $N$ -manifold or when  $|n\rangle$  is an  $E$ -state. The main idea of the derivation that will be carried out below is to start by studying (4.6) in the  $N$ -manifold. We will see that this approach gives an

expression for  $c_N$ , which can be used when looking at (4.6) in the  $E$ -manifold. In the end, the  $N$ -states will be eliminated from the problem.

So, as promised, let us start out by looking at (4.6) in the case where  $|n\rangle$  is in the  $N$ -manifold. By using the assumption of no coupling between two  $N$ -states, one finds

$$i\hbar\dot{c}_N(t) = \sum_E V_{N,E}(t)e^{-i(\omega_E-\omega_N)t}c_E(t). \quad (4.7)$$

The assumption that no  $N$ -states are initially populated assures that there is no constant of integration when this equation is integrated. The result is

$$c_N(t) = \frac{1}{i\hbar} \int_{-\infty}^t dt' \sum_E V_{N,E}(t')e^{-i(\omega_E-\omega_N)t'}c_E(t'). \quad (4.8)$$

By using (4.2) and (4.3) it is seen that the matrix element  $V_{N,E}(t)$  can be calculated as

$$V_{N,E}(t) = \langle N|V(t)|E\rangle = \frac{1}{2}\boldsymbol{\mu}_{N,E} \cdot \mathbf{e}F_0(t) \left( e^{-i\omega t} + e^{i\omega t} \right), \quad (4.9)$$

where  $\boldsymbol{\mu}_{N,E} = \langle N|\boldsymbol{\mu}|E\rangle$ . If we insert (4.9) into (4.8) and integrate by parts, we find

$$c_N(t) = \frac{1}{2\hbar} \sum_E \left( \frac{e^{-i(\omega_E-\omega_N+\omega)t}}{\omega_E-\omega_N+\omega} \boldsymbol{\mu}_{N,E} \cdot \mathbf{e}F_0(t)c_E(t) - \int_{-\infty}^t dt' \frac{e^{-i(\omega_E-\omega_N+\omega)t'}}{\omega_E-\omega_N+\omega} \boldsymbol{\mu}_{N,E} \frac{d}{dt'} [eF_0(t')c_E(t')] \right) + [\omega \rightarrow -\omega]. \quad (4.10)$$

If one keeps on integrating by parts, a series of derivatives of  $F_0(t')c_E(t')$  will occur:

$$\left( \frac{d}{dt'} \right)^s F_0(t')c_E(t'), \quad s = 0, 1, 2, \dots \quad (4.11)$$

The envelope function  $F_0(t')$  is usually slowly varying compared to the oscillations of the field. Therefore,  $F_0(t')c_E(t')$  is also slowly varying, so it is a good approximation to neglect all terms but the one with  $s = 0$ . Using this approximation, we find

$$c_N(t) = \frac{1}{2\hbar} \sum_E \left( \frac{e^{-i(\omega_E-\omega_N+\omega)t}}{\omega_E-\omega_N+\omega} \boldsymbol{\mu}_{N,E} \cdot \mathbf{e}F_0(t)c_E(t) \right) + [\omega \rightarrow -\omega]. \quad (4.12)$$

which relates  $c_N(t)$  to  $c_E(t)$ .

The next step is to look at (4.6) in the  $E$ -manifold. Here, the sum is not only over  $E$ -states but also over  $N$ -states:

$$i\hbar\dot{c}_E(t) = \sum_{E'} V_{E,E'}(t)e^{-i(\omega_{E'}-\omega_E)t}c_{E'}(t) + \sum_N V_{E,N}(t)e^{-i(\omega_N-\omega_E)t}c_N(t). \quad (4.13)$$

Now, we substitute (4.12) into the last term of (4.13), which gives a set of equations for  $c_E(t)$  that do not involve  $c_N(t)$ . This means that the  $N$ -states have been eliminated from the problem. The technique used here is called *adiabatic elimination*. The first term in (4.13) represents the direct dipole coupling between the  $E$ -states, and the second represents the Raman coupling which includes the  $N$ -states. Therefore, we write it as:

$$i\hbar\dot{c}_E(t) = \sum_{E'} \left( V_{E,E'}^{\text{dip}}(t) + V_{E,E'}^{\text{Ram}}(t) \right) c_{E'}(t) \quad (4.14)$$

where  $V_{E,E'}^{\text{dip}}(t)$  is the dipole coupling between the states  $|E\rangle$  and  $|E'\rangle$ , and  $V_{E,E'}^{\text{Ram}}(t)$  is the Raman coupling between  $|E\rangle$  and  $|E'\rangle$ . The term corresponding to the direct dipole coupling can be rewritten as:

$$\begin{aligned} V_{E,E'}^{\text{dip}}(t) &= \sum_{E'} V_{E,E'}(t) e^{-i(\omega_{E'} - \omega_E)t} c_{E'}(t) \\ &= \sum_{E'} \frac{1}{2} \boldsymbol{\mu}_{N,E} \cdot \mathbf{e} F_0(t) \left( e^{-i(\omega_{E'} - \omega_E + \omega)t} + e^{-i(\omega_{E'} - \omega_E - \omega)t} \right) c_{E'}(t). \end{aligned} \quad (4.15)$$

There are two terms here oscillating with the frequencies  $\omega_{E'} - \omega_E \pm \omega$ . When (4.14) is integrated to find  $c_E(t)$ , terms oscillating very fast compared to the time scale of interest will average to zero and can be neglected. This is the *rotating wave approximation*, and it can be used here to neglect  $V_{E,E'}^{\text{dip}}(t)$ . The reason is that our laser is assumed to be far off resonance, so

$$|\omega_{E'} - \omega_E| \ll \omega, \quad (4.16)$$

which means that both terms in  $V_{E,E'}^{\text{dip}}(t)$  oscillate with a frequency that is close to  $\omega$ . The time scale of interest is given by the energy difference  $\hbar(\omega_{E'} - \omega_E)$  (see section 2.3), and both terms in  $V_{E,E'}^{\text{dip}}(t)$  oscillate on a much smaller scale. Therefore, the rotating wave approximation is valid.

Equation (4.14) reduces to

$$i\hbar\dot{c}_E(t) = \sum_{E'} V_{E,E'}^{\text{Ram}}(t) c_{E'}(t). \quad (4.17)$$

The Raman term in (4.14) gives four terms that oscillate with different frequencies:  $\omega_{E'} - \omega_E + 2\omega$ ,  $\omega_{E'} - \omega_E - 2\omega$ , and two with  $\omega_{E'} - \omega_E$ . Because the laser is far off resonance, we can use the same arguments as above to neglect the first two terms. This leaves us with

$$V_{E,E'}^{\text{Ram}}(t) = -\frac{F_0^2(t)}{4} \sum_N \left( \frac{(\boldsymbol{\mu}_{E,N} \cdot \mathbf{e})(\boldsymbol{\mu}_{N,E'} \cdot \mathbf{e})}{\hbar(\omega_N - \omega_E + \omega)} + \frac{(\boldsymbol{\mu}_{E,N} \cdot \mathbf{e})(\boldsymbol{\mu}_{N,E'} \cdot \mathbf{e})}{\hbar(\omega_N - \omega_E - \omega)} \right). \quad (4.18)$$

Now, let us try to rewrite  $V_{E,E'}^{\text{Ram}}(t)$ . By looking at the numerators in (4.18), we see that each of the two terms is in itself a sum of nine terms. One is proportional to  $e_x e_x$ , another to  $e_x e_y$  and so on. Therefore,  $V_{E,E'}^{\text{Ram}}(t)$  can be rewritten as

$$V_{E,E'}^{\text{Ram}}(t) = -\frac{F_0^2(t)}{4} \mathbf{e}^T \boldsymbol{\alpha}_{E,E'} \mathbf{e} \quad (4.19)$$

where  $\boldsymbol{\alpha}_{E,E'}$  is a tensor expressed in a basis of eigenstates of  $H_0$ . The cartesian components  $\{a, b\}$  of this tensor are:

$$\alpha_{E,E'}^{ab} = \sum_N \left( \frac{\mu_{E,N}^a \mu_{N,E'}^b}{\hbar(\omega_N - \omega_E + \omega)} + \frac{\mu_{E,N}^b \mu_{N,E'}^a}{\hbar(\omega_N - \omega_E - \omega)} \right). \quad (4.20)$$

This rather complicated equation can be connected to a quantity we are more familiar with. If one expands the energy of a system to second order in terms of the applied electric field, one finds (see [39])

$$E(\mathbf{F}) = E(\mathbf{F} = 0) - \boldsymbol{\mu} \cdot \mathbf{F} - \frac{1}{2} \mathbf{F}^\dagger \boldsymbol{\alpha} \mathbf{F}, \quad (4.21)$$

where  $\boldsymbol{\alpha}$  is the polarizability tensor. Equation (4.19) is of the same form as the last term in (4.21), and the potential  $V_{E,E'}^{\text{Ram}}(t)$  is also an energy. This means that  $\alpha_{E,E'}$  is nothing but a polarizability tensor.

The difference of (4.19) and the last term in (4.21) by a factor of 2 is caused by a switch between the static and dynamic polarizabilities. In the static picture, one studies static electric fields, while oscillating fields are used in the dynamic picture. Strictly speaking, (4.21) is a static equation, while the polarizability found in the above calculations is dynamic. An oscillating field with the intensity  $F_0^2 \cos^2 \omega t$  corresponds, time averaged, to a static field with the intensity  $F_0^2/2$  [40].

The expression (4.20) can be simplified by noting that the vibrational and rotational energies are on a smaller scale than the electronic energies. Therefore, the quantities in (4.20) will mainly depend on the electronic states  $e_E$ ,  $e_{E'}$  and  $e_N$ . Assuming that both  $|E\rangle$  and  $|E'\rangle$  belong to the first electronic manifold  $e_1$ , we can write the polarizability as

$$\alpha_{e_1}^{ab} = \sum_{e_N} \left( \frac{\mu_{e_1,e_N}^a \mu_{e_N,e_1}^b}{\hbar(\bar{\omega}_{e_N,e_1} + \omega)} + \frac{\mu_{e_1,e_N}^b \mu_{e_N,e_1}^a}{\hbar(\bar{\omega}_{e_N,e_1} - \omega)} \right), \quad (4.22)$$

where  $\bar{\omega}_{e_N,e_1}$  is the average electronic energy splitting. Since the polarizability only depends on  $e_1$  we can now write (4.19) as

$$V_{e_1}^{\text{Ram}}(t) = -\frac{F_0^2(t)}{4} \mathbf{e}^T \boldsymbol{\alpha}_{e_1} \mathbf{e}. \quad (4.23)$$

One final approximation could be made: for a laser pulse in the near infrared regime ( $\lambda \sim 800$  nm), the frequency is low enough to neglect  $\omega$  in (4.22), i.e.

$$\bar{\omega}_{e_N,e_1} \gg \omega, \quad (4.24)$$

as long as  $e_N \neq e_1$ . With this approximation the dynamic polarizability is reduced to the static polarizability. This is a really useful approximation in many cases, because static polarizabilities can often be found in the literature. For the calculations in future chapters of this thesis we will not use a static polarizability, though, but the dynamic calculated at a wavelength of 800 nm. It is calculated in [2].

What we have done in this section is to write the matrix elements of (4.6) as an effective interaction Hamiltonian. Instead of solving the coupled differential equations in (4.6), we can now write down a normal Hamiltonian with an extra potential  $V_{e_1}^{\text{Ram}}(t)$ , which corresponds to the interaction between the molecule and the laser. The interaction between the molecule and the laser can thus be described by the following Hamiltonian:

$$H = H_0 + V_{e_1}^{\text{Ram}}(t) \quad (4.25)$$

where  $H_0$  is the Hamiltonian of the molecule. Such an interaction has the possibility of activating certain normal modes of the molecule, for example rotation or torsion, as described in section 2.4, because the molecule is not ionized or dissociated.

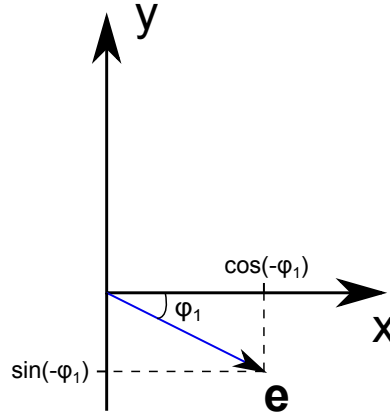


Figure 4.3: A figure of the components of  $e$  in the molecular frame. The axes in figure 3.3 have been rotated by about  $120^\circ$ . The vector  $e$  points along the  $X$ -axis of figure 3.3.

### 4.3 Application of the results to the experiments of interest

In this section, we will apply the result (4.23) to the experiments [1, 2, 3]. As mentioned in section 3.2, we assume that the molecules are already aligned, and then we want to describe the interaction between the molecule and the kick pulse. The kick pulse is polarized in the  $X$ -direction (in lab frame, see figure 3.3), but the following calculation will be carried out in the molecular frame  $(x, y, z)$ . Therefore, we will write down the  $x$ ,  $y$ , and  $z$  components of  $e$ . When we remember that the  $Z$ - and  $z$ -axes are coinciding, it is seen in figure 4.3 that these components are

$$e_x = \cos \phi_1, \quad e_y = -\sin \phi_1, \quad e_z = 0. \quad (4.26)$$

Next we note that the polarizability tensor is symmetric, so  $\alpha^{xy} = \alpha^{yx}$ . When this fact is used and (4.26) is inserted into (4.23), we obtain

$$V_{e_1}^{\text{Ram}}(t) = -\frac{F_0^2(t)}{4} \left[ \alpha_{e_1}^{xx} \cos^2 \phi_1 + \alpha_{e_1}^{yy} \sin^2 \phi_1 - 2\alpha_{e_1}^{xy} \cos \phi_1 \sin \phi_1 \right]. \quad (4.27)$$

The polarizabilities  $\alpha_{e_1}^{ab}$  have been calculated in [2] for DFDBrBPh, and it is seen that they only depend on  $\phi_d = \phi_1 - \phi_2$ , the dihedral angle. The result is

$$\alpha^{xx} = a_1 \cos(2\phi_d) + c_1 \quad \alpha^{yy} = a_2 \cos(2\phi_d) + c_2 \quad \alpha^{xy} = a_3 \sin(2\phi_d) + c_3, \quad (4.28)$$

where the coefficients are

$$\begin{aligned} a_1 &= 16.91 \text{ a.u.} & c_1 &= 200.9 \text{ a.u.} \\ a_2 &= -20.11 \text{ a.u.} & c_2 &= 112.6 \text{ a.u.} \\ a_3 &= -18.81 \text{ a.u.} & c_3 &= -0.009464 \text{ a.u.} \end{aligned} \quad (4.29)$$

The coefficients apply when the dihedral angle is measured in radians. Now, we have written the potential  $V_{e_1}^{\text{Ram}}(t)$  on a form where it only depends on the angles of the two phenyl rings:



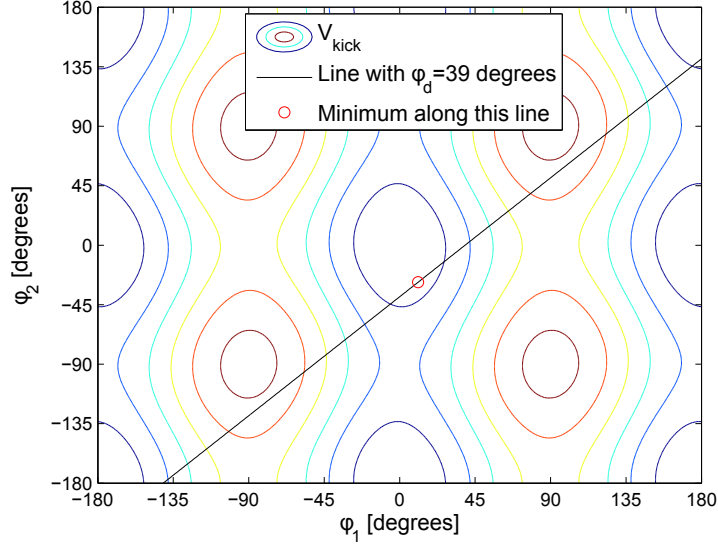


Figure 4.4: Contour plot of the kick potential  $V_{\text{kick}}$  as function of  $\phi_1$  and  $\phi_2$ . The red curves correspond to high values of  $V_{\text{kick}}$  and the blue ones to low values. By definition, the potential has a minimum at the SMPA, which for  $\phi_d = 39^\circ$  corresponds to  $\phi_1 = 11^\circ$  and  $\phi_2 = -28^\circ$ . This value is consistent with experiments.

$$V_{\text{kick}}(\phi_1, \phi_2, t) = -\frac{F_0^2(t)}{4} \left[ \alpha^{xx}(\phi_1 - \phi_2) \cos^2 \phi_1 + \alpha^{yy}(\phi_1 - \phi_2) \sin^2 \phi_1 - 2\alpha^{xy}(\phi_1 - \phi_2) \cos \phi_1 \sin \phi_1 \right]. \quad (4.30)$$

Here, the interaction has been renamed  $V_{\text{kick}}$  for consistency with the rest of this thesis. It will from now on be called the kick potential. The labelling by the electronic state  $e_1$  has also been abandoned to simplify the notation.

As noted in section 3.2, the kick pulse will align the SMPA with the kick pulse polarization, i.e. the X-axis. This means that the SMPA is simply the axis where (4.30) has a minimum. The kick potential is plotted in figure 4.4, where the minimum along the line given by  $\phi_d = 39^\circ$  is shown. This minimum is at  $\phi_1 = 11^\circ$  and  $\phi_2 = -28^\circ$ , which agrees with the experimental results in section 3.3.

## 4.4 Summary

In this chapter, the interaction between a non-ionizing laser field and a gas of molecules has been studied. An effective Hamiltonian was found, and it was applied to the particular geometry used in the experiments [1, 2, 3]. The resulting potential corresponds to an interaction between the field and the induced dipole of the molecule, as expected from section 2.4.



## Chapter 5

# A semiclassical model

### 5.1 Outline of the model

In this chapter, a semiclassical model for the interaction between the molecules (DFDBrBPh or DFDBrCNBPh) and the lasers will be discussed. This model is a continuation of the discussion in section 3.2, and it also relies on the separation of the Hamiltonian into a rotational and a torsional part. The rotational evolution is then treated classically, and the torsion is treated quantum mechanically. Solution of a one-dimensional time-dependent Schrödinger equation is required. The strategy is to solve the time-independent Schrödinger equation for a simpler problem first and then use the results to solve the entire problem. In this case, the simpler problem is ignoring the kick pulse, so the equation to study is (3.7) from section 3.2. The reason why the rotation and torsion can be separated is that the kick pulse is only present for a very short time, so the solution to the simpler problem can be used as an initial condition. The temperature of the molecular gas will be assumed to be 0 K, which means that effects of finite temperature are ignored. In the papers [1, 2, 3], this model was used to explain the experimental results.

Sections 5.2 and 5.3 will show how one can separate the torsion and rotation of the molecule, and the solution of the problem without the kick pulse, equation (3.7), will be described in sections 5.4 and 5.5. The total problem is solved in section 5.6, and the results are discussed and compared to experiments in section 5.7.

We will see that the separation of rotation and torsion shown in this chapter is not exact. A more thorough investigation of this problem is discussed in section 6.4.

### 5.2 The angles $\phi_d$ and $\Phi$

As discussed in section 3.2, the molecule DFDBrBPh can be described by a Hamiltonian of the form

$$H = -\frac{1}{2I_1} \frac{\partial^2}{\partial \phi_1^2} - \frac{1}{2I_2} \frac{\partial^2}{\partial \phi_2^2} + V_{\text{tor}}(\phi_1 - \phi_2), \quad (5.1)$$

where  $\phi_1$  and  $I_1$  are the angle and the moment of inertia of the bromine plane. The angle and moment of inertia of the iodine plane are called  $\phi_2$  and  $I_2$ , and  $V_{\text{tor}}$  is the torsional potential which is given by (3.1). The angles  $\phi_1$  and  $\phi_2$  are defined in figure 3.3 along with the axes of the molecular and laboratory frame.

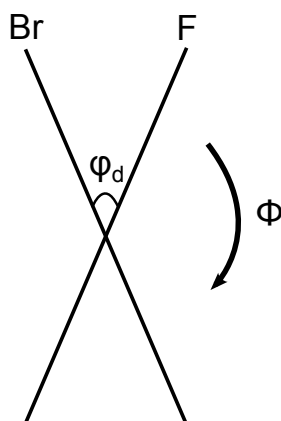


Figure 5.1: This figure shows the molecule DFDBrBPh viewed along the stereogenic axis. The angle  $\phi_d$  corresponds to torsion, and  $\Phi$  is a rotational angle for the entire molecule.

Instead of using  $\phi_1$  and  $\phi_2$ , one can change the coordinates to the dihedral angle and a rotational angle for the entire molecule, see figure 5.1. As described in section 3.2, the dihedral angle is defined as

$$\phi_d = \phi_1 - \phi_2. \quad (5.2)$$

The overall rotational angle is, as will be shown below,

$$\Phi = (1 - \eta)\phi_1 + \eta\phi_2, \quad (5.3)$$

where  $\eta = \frac{I_2}{I_1 + I_2}$ . A simple calculation shows that the transformation from  $(\phi_1, \phi_2)$  to  $(\phi_d, \Phi)$  is described by the matrix

$$\begin{pmatrix} 1 & -1 \\ 1 - \eta & \eta \end{pmatrix} \quad (5.4)$$

and the inverse transformation by

$$\begin{pmatrix} \eta & 1 \\ \eta - 1 & 1 \end{pmatrix} \quad (5.5)$$

The expression (5.3) for the overall rotational angle is found from the following argument: The two rings of the molecule each rotate about the Z-axis. We want to describe these two rings as *one* body rotating about this axis. It will have total moment of inertia  $I = I_1 + I_2$ , and the total angular momentum will be given by

$$L = I\omega = (I_1 + I_2)\omega, \quad (5.6)$$

where  $\omega$  is the angular velocity of the total molecule rotating about the Z-axis. We note that  $\omega \equiv d\Phi/dt$ . Since  $L$  can also be written as  $L = I_1\omega_1 + I_2\omega_2$ , this gives us

$$\omega = \frac{I_1\omega_1 + I_2\omega_2}{I_1 + I_2} = (1 - \eta)\omega_1 + \eta\omega_2. \quad (5.7)$$

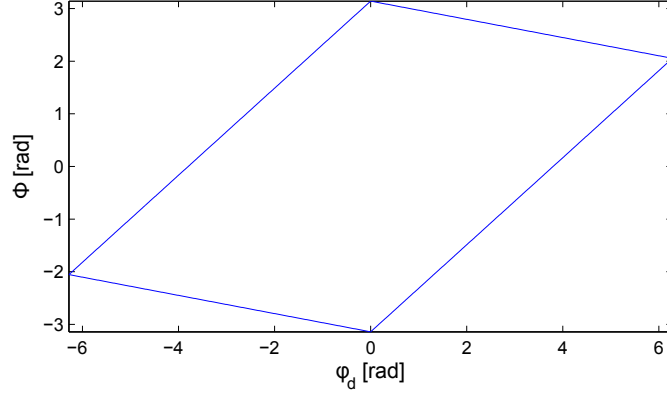


Figure 5.2: The area  $]-\pi, \pi[ \times ]-\pi, \pi[$  in the  $(\phi_1, \phi_2)$ -plane can be transformed to the  $(\phi_d, \Phi)$ -plane, and the result is shown here. It is not a cartesian product, meaning that the boundary conditions for  $\Phi$  depend on  $\phi_d$ .

We then integrate this equation from  $t_0$  to  $t$  to obtain

$$\Phi(t) - \Phi(t_0) = (1 - \eta)(\phi_1(t) - \phi_1(t_0)) + \eta(\phi_2(t) - \phi_2(t_0)). \quad (5.8)$$

It is readily seen that a solution to this is  $\Phi = (1 - \eta)\phi_1 + \eta\phi_2$ .

Something is missing in this derivation, though. When  $\Phi$  is kept constant and  $\phi_d$  is changed by  $2\pi$ , the two molecular planes do not return to the exact same position. This seems to contradict the interpretation of  $\Phi$  as an overall rotational angle, but for now, we stick to this choice of coordinates anyway. To think of  $\Phi$  as an overall rotational angle will at least be sensible for small variations in  $\Phi$ . The problems only occur when the movements in  $\Phi$  become so large that the periodicity plays a role.

The area of relevance in the  $(\phi_1, \phi_2)$ -plane is the cartesian product  $]-\pi, \pi[ \times ]-\pi, \pi[$ . If we try to describe this area in the  $(\phi_d, \Phi)$ -plane, we arrive at the area seen in figure 5.2. This means that the boundary conditions for  $\Phi$  depend on  $\phi_d$ , and thus, the angles are not independent of each other.

Even though there are such problems with the angles  $(\phi_d, \Phi)$ , we assume for the rest of this chapter that  $\phi_d$  and  $\Phi$  are both  $2\pi$ -periodic and independent of each other. The real periodicity and boundary conditions will be discussed further in section 6.4.

With the new angles  $\phi_d$  and  $\Phi$ , one can show that the Hamiltonian (3.7) can be rewritten as

$$H = -\frac{1}{2I} \frac{\partial^2}{\partial \Phi^2} - \frac{1}{2I_{\text{rel}}} \frac{\partial^2}{\partial \phi_d^2} + V_{\text{tor}}(\phi_d) = H_{\Phi} + H_{\phi_d}, \quad (5.9)$$

where  $I_{\text{rel}} = I_1 I_2 / I$  and we recall that  $I = I_1 + I_2$ .

The approximation that  $\phi_d$  and  $\Phi$  are both  $2\pi$ -periodic and independent of each other is motivated by the following facts: the kick pulse is very short, so the time scale of interest is very small; below a picosecond. From (5.9) we see that the energy scale which is relevant for rotation is given by  $\hbar^2 / (2I) = 1.3 \mu\text{eV}$ , so the relevant time scale for rotation is a few nanoseconds. For torsion, the energy scale is not determined by the kinetic term in (5.9), but by the potential term instead. A harmonic approximation of the torsional potential provides a

relevant energy scale of 3.1 meV, which corresponds to a time scale of about a few picoseconds. We can conclude that the molecule will not rotate very much at the time scale of the kick pulse, but there will be torsional motion. This means that the effect of the kick pulse is to excite the molecule into a higher torsional state, but it almost does not change the rotational state. The picture used in this chapter is that the rotation does not come into play before the kick pulse has disappeared. This argument shows that a separation of the torsional and rotational motion makes sense physically. It is also consistent with the considerations of section 2.3, since torsion is a type of vibrational motion, and vibration is faster than rotation.

### 5.3 Reduction to a 1D problem

The Hamiltonian (5.9) is a sum of the  $\Phi$ -dependent part,  $H_\Phi$ , and a  $\phi_d$ -dependent part,  $H_{\phi_d}$ . Since we have assumed that  $\phi_d$  and  $\Phi$  are independent of each other, this allows us to use a product ansatz,

$$\psi(\Phi, \phi_d) = X(\Phi)\chi(\phi_d). \quad (5.10)$$

When this state is inserted into the time-independent Schrödinger equation  $H\psi = E\psi$ , the result is

$$-\frac{1}{2I} \frac{\partial^2}{\partial \Phi^2} X(\Phi) - \frac{1}{2I_{\text{rel}}} \frac{\partial^2}{\partial \phi_d^2} \chi(\phi_d) + V_{\text{tor}} \chi(\phi_d) = E \quad (5.11)$$

We can separate the dependence on  $\Phi$  and  $\phi_d$  into two different terms whose sum is a constant. Therefore, each of the terms must be equal to a constant. This gives

$$-\frac{1}{2I} \frac{\partial^2}{\partial \Phi^2} X(\Phi) = \alpha X(\Phi), \quad -\frac{1}{2I_{\text{rel}}} \frac{\partial^2}{\partial \phi_d^2} \chi(\phi_d) + V_{\text{tor}}(\phi_d) \chi(\phi_d) = \beta \chi(\phi_d), \quad (5.12)$$

where  $\alpha + \beta = E$ . Now, we have two separate equations, one for  $\phi_d$  and one for  $\Phi$ . The numbers  $\alpha$  and  $\beta$  can be thought of as the rotational and torsional energy respectively. This separation was achieved by assuming  $\Phi$  and  $\phi_d$  to be independent of each other. We also assumed that they were both  $2\pi$ -periodic, which will be used when solving the problem numerically.

The first equation in (5.12) can be solved analytically, but instead of doing so, we treat  $\Phi$  classically. This is done because it simplifies the later derivations and calculations. The motivation is the same as for separating torsional and rotational motion: Rotation happens on a large time scale, and it may thus be accurate to treat it classically. Since the first equation is treated classically, we are left with a 1D quantum mechanical problem. The equation to be solved is the second equation in (5.12), which can be rewritten as

$$H_{\phi_d} \chi(\phi_d) = E_{\text{tor}} \chi(\phi_d), \quad (5.13)$$

where

$$H_{\phi_d} = -\frac{1}{2I_{\text{rel}}} \frac{\partial^2}{\partial \phi_d^2} + V_{\text{tor}}(\phi_d) = H_{\phi_d,0} + V_{\text{tor}} \quad (5.14)$$

and  $E_{\text{tor}} = \beta$ . Before we can include the kick pulse, we must solve equation (5.13). A description of how to do so is found in the next section.

### 5.4 Numerical solution of the 1D equation

Equation (5.13) can be solved numerically, and in this section we will see how this is done. We start by considering the much simpler problem where the torsional potential is not included. The only term left in  $H_{\phi_d}$  is then  $H_{\phi_d,0}$ , and the equation to solve is

$$H_{\phi_d,0}\chi_0(\phi_d) = \epsilon_0\chi_0(\phi_d), \quad (5.15)$$

where  $\chi_0$  is an eigenstate of  $H_{\phi_d,0}$  and  $\epsilon_0$  the corresponding energy. When this has been solved, we will use the solutions as basis functions for solving the entire problem (5.13). Equation (5.15) can be solved analytically, and the solutions can be written in two different ways:

$$\chi_0(\phi_d) = A \sin(m\phi_d) + B \cos(m\phi_d) \quad \text{or} \quad \chi_0(\phi_d) = A \exp(im\phi_d) + B \exp(-im\phi_d), \quad (5.16)$$

where  $A$  and  $B$  are constants and  $m = \sqrt{2I_{\text{rel}}\epsilon_0}$ . Because of the  $2\pi$ -periodic boundary conditions,  $m$  must be an integer. The two ways of writing the solutions correspond to two different choices of basis: sines/cosines or exponentials. For sines and cosines, we do not have to include the negative values of  $m$ , since sines are odd and cosines even. The value  $m = 0$  does not contribute for the sine, because  $\sin(0) = 0$ , but for cosine it gives a constant. For the exponential,  $m = 0$  also gives a constant. The normalized sine/cosine-basis is given by

$$\left\{ \frac{1}{\sqrt{2\pi}}, \frac{1}{\sqrt{\pi}} \sin(m\phi_d), \frac{1}{\sqrt{\pi}} \cos(m\phi_d) \right\}, \quad m \in \mathbb{N}, \quad (5.17)$$

and the normalized exponential basis is

$$\left\{ \frac{1}{\sqrt{2\pi}} \exp(im\phi_d) \right\}, \quad m \in \mathbb{Z}. \quad (5.18)$$

Since these bases consist of eigenstates of  $H_{\phi_d,0}$ , it is natural use them for solving (5.13) numerically. The idea behind this numerical strategy is to write  $H_{\phi_d}$  as a matrix in one of the bases and then find the eigenvalues and eigenvectors of this matrix, or, in other words, to diagonalize the matrix.

Here follows a derivation of how a quantum mechanical problem is solved in a basis. In later chapters we will refer to this derivation, because the method will be applied again. To simplify the formulas, the bra-ket notation will be used. We have a complete basis  $\{|m\rangle\}$ , which in this case could be either the sine/cosine or the exponential basis, and the kets corresponding to solutions of (5.13) will be denoted by  $|\chi_n\rangle$ . In this notation, (5.13) becomes

$$H_{\phi_d} |\chi_n\rangle = E_n |\chi_n\rangle. \quad (5.19)$$

The  $|\chi_n\rangle$ -states can be expanded in the  $m$ -basis as

$$|\chi_n\rangle = \sum_m c_{m,n} |m\rangle \quad (5.20)$$

When (5.20) is inserted into (5.19), we obtain

$$H_{\phi_d} \sum_m c_{m,n} |m\rangle = E_n \sum_m c_{m,n} |m\rangle. \quad (5.21)$$

This is projected onto  $|m'\rangle$ , and the result is

$$\sum_m \langle m' | H_{\phi_d} | m \rangle c_{m,n} = E_n c_{m',n}. \quad (5.22)$$

This can be interpreted as a matrix equation

$$H \mathbf{c}_n = E_n \mathbf{c}_n, \quad (5.23)$$

where  $H$  is a matrix whose  $(m', m)$  entry is  $\langle m' | H_{\phi_d} | m \rangle$ ,  $\mathbf{c}_n$  is an eigenvector of  $H$  whose  $m$ th entry is  $c_{m,n}$ , and  $E_n$  is the  $n$ th eigenvalue of  $H$ . For one matrix  $H$  there are several eigenvectors  $\mathbf{c}_n$  and eigenvalues  $E_n$ .

Now, we can find eigenvectors and eigenvalues of (5.23) by using a diagonalization routine on  $H$ . MATLAB has two routines that are relevant. One is called *eig*, and it finds all eigenvectors and eigenvalues. If the amount of elements in the basis is very large, one can make the calculations faster by using sparse matrices and the command *eigs*, which only returns specific eigenvectors and eigenvalues.

As can be seen from (5.18) and (5.17), the bases are infinite, which means that our matrix is infinitely large. To be able to do any practical calculations, we must have a finite matrix. The way to ensure that the results are still correct is to solve the problem with a certain number of basis elements  $N$  and then increase that number and solve the problem again. This process is repeated until a convergence of the result is seen. Such a procedure can only be expected to work if one orders the basis in a smart way. The eigenfunctions we want to find do not vary infinitely fast as a function of  $\phi_d$ , so basis states with a high value of  $|m|$  only play a minor role. Therefore, we must order the basis by increasing  $|m|$ .

There is one last thing we have to do before the computer can start calculating, and that is to find the matrix elements  $\langle m' | H_{\phi_d} | m \rangle$ . This has been done analytically, using the formula for  $V_{\text{tor}}$  in (3.1). For the exponential basis the calculation is

$$\begin{aligned} \langle m_1 | V_{\text{tor}} | m_2 \rangle &= \frac{1}{2\pi} \int_{-\pi}^{\pi} d\phi_d e^{i(m_2 - m_1)\phi_d} [a \cos(4\phi_d) + b \cos(2\phi_d) + d \cos(6\phi_d) + e \cos(8\phi_d) + c] \\ &= \frac{1}{2\pi} \int_{-\pi}^{\pi} d\phi_d \left[ \frac{a}{2} \left( e^{i(m_2 - m_1 + 4)\phi_d} + e^{i(m_2 - m_1 - 4)\phi_d} \right) \right. \\ &\quad + \frac{b}{2} \left( e^{i(m_2 - m_1 + 2)\phi_d} + e^{i(m_2 - m_1 - 2)\phi_d} \right) + \frac{d}{2} \left( e^{i(m_2 - m_1 + 6)\phi_d} + e^{i(m_2 - m_1 - 6)\phi_d} \right) \\ &\quad \left. + \frac{e}{2} \left( e^{i(m_2 - m_1 + 8)\phi_d} + e^{i(m_2 - m_1 - 8)\phi_d} \right) + c e^{i(m_2 - m_1)\phi_d} \right] \\ &= \frac{a}{2} (\delta_{m_2 - m_1, 4} + \delta_{m_2 - m_1, -4}) + \frac{b}{2} (\delta_{m_2 - m_1, 2} + \delta_{m_2 - m_1, -2}) \\ &\quad + \frac{d}{2} (\delta_{m_2 - m_1, 6} + \delta_{m_2 - m_1, -6}) + \frac{e}{2} (\delta_{m_2 - m_1, 8} + \delta_{m_2 - m_1, -8}) + c \delta_{m_2, m_1}. \end{aligned}$$

Here,  $\delta_{n,m}$  is Kronecker's delta. For the basis of sines and cosines, the calculation is more difficult. This is mainly because there are different kinds of basis elements. Some are sines, others are cosines, and the integrals have to be done independently. The corresponding matrix elements are seen in appendix A. The reason why we still bother using the basis of sines and cosines is that the resulting wave functions become real valued, and thus, the wave function itself is easily plotted. For the exponential basis, it is harder to visualize the wave functions, and one usually plots their norms squared instead.



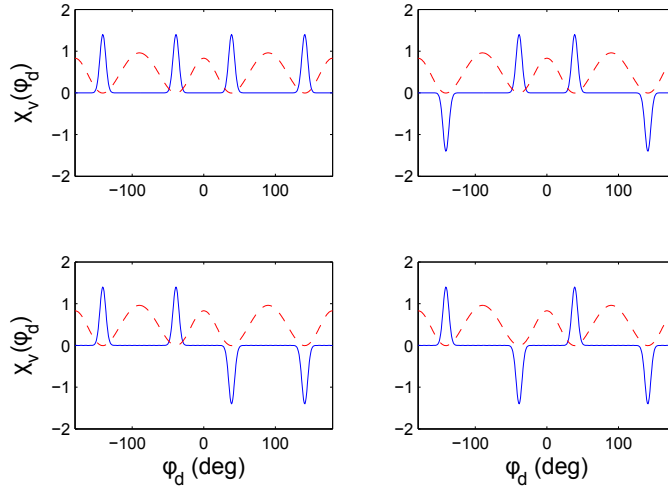


Figure 5.3: The blue curves are the four lowest eigenstates  $\chi_v$  of (5.13). They are only non-zero near the bottom of the four wells in the torsional potential, which is marked by the red dashed line. It is obvious from this figure that localized states can be created as simple superpositions of these four states. The results shown in this figure are calculated using the basis of sines and cosines, which is why the wave functions are real valued.

Now, we have everything we need to do the numerical calculations. The number of basis elements needed for convergence of the first few eigenstates turns out to be about 100 for both choices of basis.

## 5.5 Results: Eigenvalues and eigenstates

In this section, we discuss the eigenvalues and eigenfunctions of (5.14) that come out of the numerical calculation described in the previous section. As discussed in section 3.2, the torsional potential has four minima (see figure 3.2), and we therefore expect four almost degenerate eigenstates at the lowest energy. This has in fact been found using both bases. In fact, all eigenstates come in groups of four that are almost degenerate. At least for the lower energy states, we see that the energies resemble those of a harmonic oscillator,

$$E_j = 2E_0(j + 1/2), \quad (5.24)$$

where  $E_0$  is the ground state energy and  $j$  is a non-zero integer telling which manifold of four almost degenerate states we are talking about. This is expected, since each well in the torsional potential can be approximated by a harmonic oscillator near the bottom.

The four eigenstates with lowest energies, calculated in the basis of sines and cosines, are seen on figure 5.3. They have an energy 1.725 meV above the minimum of the torsional potential, and the difference between these energy levels is of the order of  $10^{-13}$  eV. This is consistent with what is found in [2], using the exact same theory. All four states have a non-zero probability density in all four wells. For the states calculated in the basis of exponentials, everything is the same, except that they also have an imaginary part.

One can create states that only reside in one of the four wells as simple superpositions of the four lowest eigenstates. These localized states will have a long lifetime because the energies of the eigenstates are close to each other, meaning that the different eigenstates will not interfere much with each other. The notation for the localized states is  $|L_j^{(i)}\rangle$ , where  $j$  is the number of the fourfold almost degenerate manifold, and  $i$  denotes which well the state is localized in. For the rest of this chapter, we will use one of these localized states as the initial state when solving the full time-dependent problem.

For the solutions obtained using the exponential basis, the superpositions are not as simple, and the coefficients belonging to each eigenstate cannot immediately be guessed. They can be found numerically, though, using a solving routine for a set of non-linear equations. The equations to be solved correspond to fixing the value of  $\langle\phi_d\rangle$  to be in one of the minima and minimizing  $|\chi(\phi_d)|^2$  in the three other minima.

## 5.6 Inclusion of the kick pulse

The strategy used in this section is still based on treating  $\Phi$  classically and  $\phi_d$  quantum mechanically, as mentioned in section 5.3. We will start out with  $\phi_d$ . Until now, we have found eigenstates for (5.14), the Hamiltonian that does not include the kick pulse, and we have discussed the localized states. Now we will describe the interaction with the kick pulse. This interaction is given by a potential  $V_{\text{kick}}$ , that will be added to the Hamiltonian (5.14) to give

$$H_{\phi_d, \text{kick}} = -\frac{1}{2I_{\text{rel}}} \frac{\partial^2}{\partial \phi_d^2} + V_{\text{tor}}(\phi_d) + V_{\text{kick}}(\phi_d, \Phi, t). \quad (5.25)$$

The eigenstates for (5.14) that were found in section 5.5, can be used as a basis for describing (5.25). They can also be used to find the correct initial state.

In section 4.3, we found a formula for the kick pulse potential, (4.30). It can easily be transformed to  $(\phi_d, \Phi)$ -coordinates, and the result is

$$V_{\text{kick}}(\phi_d, \Phi, t) = -\frac{F_0^2(t)}{4} \left[ \alpha^{xx}(\phi_d) \cos^2(\Phi + \eta\phi_d) + \alpha^{yy}(\phi_d) \sin^2(\Phi + \eta\phi_d) - 2\alpha^{xy}(\phi_d) \cos(\Phi + \eta\phi_d) \sin(\Phi + \eta\phi_d) \right], \quad (5.26)$$

where  $F_0(t)$  is the envelope of the kick pulse, and  $\alpha$  is the polarizability tensor of the molecule, see (4.28).

This time, we are interested in the time-dependent Schrödinger equation for the molecule and the kick pulse,

$$i \frac{\partial}{\partial t} |\psi\rangle = \left( -\frac{1}{2I_{\text{rel}}} \frac{\partial^2}{\partial \phi_d^2} + V_{\text{tor}}(\phi_d) + V_{\text{kick}}(\phi_d, \Phi, t) \right) |\psi\rangle. \quad (5.27)$$

This equation becomes a 1D equation if we solve it while keeping  $\Phi$  constant. This will in fact be a good approximation, since the time evolution of  $\Phi$  happens on a larger time scale than the time evolution of  $\phi_d$ . Then, equation (5.27) only depends on  $\phi_d$  and  $t$ .

To describe the initial state of the system, we refer to sections 2.6 and 3.2. From the discussions in these sections, we seen that the gas of molecules will initially be in a state described by the density matrix

$$\rho(t_0) = \sum_{\nu} P_{\nu} |\chi_{\nu}\rangle \langle\chi_{\nu}|, \quad (5.28)$$

where  $|\chi_\nu\rangle$  are eigenstates of the Hamiltonian without the kick pulse, in this case (5.14), and  $P_\nu$  the corresponding probabilities. If the gas is very cold, we can neglect all terms but the four almost degenerate states with the lowest energy. Since the localized states  $|L_j^{(i)}\rangle$  are almost eigenstates of the Hamiltonian without the kick pulse, they will almost constitute a complete basis, and one can expand in these states as well. Then, the density matrix has the form

$$\rho(t_0) = \sum_{i=1}^4 P_0^{(i)} |L_0^{(i)}\rangle \langle L_0^{(i)}|, \quad (5.29)$$

that is a sum of the four lowest localized states weighted by the probabilities  $P_0^{(i)}$ . Each term in the sums (5.28) and (5.29) evolves in time without being affected by the other terms, so we only have to propagate one term at a time. In the end, we can add the results incoherently. From now on, we will actually limit ourselves to studying the propagation of *one* localized state which is a pure state, not a mixed state. We will not even do the calculations for all localized states and then add the results incoherently, because the results are expected to be the same because of symmetry. There is no apparent reason why a molecule with  $\phi_d = 39^\circ$  should be affected differently by the kick pulse than a molecule with  $\phi_d = -39^\circ$ . Since the four lowest energy eigenstates are not completely degenerate, it is an approximation to use the localized states as basis, and thus, a problem to focus on a single localized state. This problem will be discussed further in section 8.6.

Since the localized states are almost eigenstates of  $H_{\phi_d}$ , as defined in (5.14), let us now discuss how such an eigenstate  $|\chi_n\rangle$  evolves in time. When the kick pulse hits the molecule, the state of the molecule is kicked into a superposition of  $|\chi_n\rangle$ -states. We will have a wave packet, and the coefficients will depend on the value of  $\Phi$  chosen in the kick pulse potential. We therefore call it  $|\chi_n^\Phi\rangle$ . So

$$|\chi_n\rangle \rightarrow |\chi_n^\Phi\rangle = \sum_{n'} c_{n',n}^\Phi(t) e^{-iE_{n'}(t-t_0)} |\chi_{n'}\rangle, \quad (5.30)$$

where  $c_{n',n}^\Phi(t)$  is the amplitude for the state  $|\chi_n\rangle$  to evolve into  $|\chi_{n'}\rangle$  after a time  $t$ . This amplitude also depends on  $\Phi$ . If (5.30) is inserted into (5.27) instead of  $|\psi\rangle$ , and the result is projected onto  $|\chi_{n''}\rangle$  we get

$$i \frac{\partial}{\partial t} c_{n'',n}^\Phi(t) = \sum_{n'} \langle \chi_{n''} | V_{\text{kick}}(\phi_d, \Phi, t) | \chi_{n'} \rangle c_{n',n}^\Phi(t) e^{i(E_{n''} - E_{n'}) (t - t_0)}. \quad (5.31)$$

The calculation is exactly the same as in (4.4)-(4.6).

This differential equation in  $c_{n',n}^\Phi$  is what we need to solve. Before we do that, let us look at the classical evolution of  $\Phi$ . We treat this angle classically, because the evolution will be relatively slow, as described in section 5.2. The molecule experiences a torque from the kick pulse,

$$\tau = - \frac{\partial \langle V_{\text{kick}} \rangle (\Phi, t)}{\partial \Phi}. \quad (5.32)$$

The expression  $\langle V_{\text{kick}} \rangle (\Phi, t)$  should be understood as the expectation value of  $V_{\text{kick}}$ , and this expectation value is a function of  $\Phi$  and  $t$ . The torque will give rise to a rotation, since

$$I \ddot{\Phi} = \tau = - \frac{\partial \langle V_{\text{kick}} \rangle (\Phi, t)}{\partial \Phi}. \quad (5.33)$$

Remember that  $I = I_1 + I_2$ . Now, we have an equation of motion for the classical rotation. It can be simplified by making the assumption that  $\Phi$  is equal to the constant  $\Phi_0$  while the kick pulse is affecting the system. This assumption makes sense, because the kick pulse is short, and rotation happens on a larger time scale. Then, we can integrate (5.33) twice to obtain

$$\Phi(t) = \Phi_0 - t \frac{1}{I} \left( \frac{\partial}{\partial \Phi} \int_{-\infty}^{\infty} dt' \langle V_{\text{kick}} \rangle (\Phi, t') \right) \Big|_{\Phi=\Phi_0} \quad (5.34)$$

Equations (5.31) and (5.34) are the ones we have to solve. They are not coupled to each other.

The initial  $\phi_d$ -dependence has been discussed above, the result being that we will just look at one localized state  $|L_0^{(i)}\rangle$ . The initial  $\Phi$ -dependence should also be found, and since the rotation is treated classically,  $\Phi$  must initially be fixed to a certain value  $\Phi_0$ . This means that the initial state is 3D-aligned, which corresponds well to the experiment in [3], but not 1D-aligned as in the experiment in [1, 2]. It is therefore expected that the results will be a better match to the new experiment in [3], even though the torsional potential of the wrong molecule is used, as described in section 3.2.

When solving the two equations, the idea is to start from the initial state and propagate both equations forward in time. The solution of  $\Phi$  is achieved by noting that  $\langle V_{\text{kick}} \rangle (\Phi, t')$  only has a non-zero value around  $t = 0$ , where the kick pulse peaks at  $t = 0$ . The reason is that the kick pulse is so short, and it is even a good approximation to only use the value at exactly  $t = 0$ .

Equation (5.31) is a system of ordinary differential equations, and there are many methods available for solving such systems. Many routines are based on Runge-Kutta methods or the Euler method, where the kick potential is described as a matrix in a basis of eigenstates of (5.14). The main disadvantage of these methods is that one has to find the matrix elements  $\langle \chi_n | V_{\text{kick}}(\phi_d, \Phi, t) | \chi_{n'} \rangle$ .

Another approach was chosen for this work. Equation (5.31) was solved on a numerical grid using a split step routine and Fourier transforms. This will be described in further detail in chapter 7. The method of propagating on a grid has the disadvantage that the coefficients  $c_{n',n}^{\Phi}(t)$  are not found; only the final wave function is.

To compare the theoretical results to experiments, for example figure 3.6, we need to find the expectation value of  $\phi_d$ . Since we have chosen to describe the propagation of a single pure state, it is simply the numerical integral

$$\langle \phi_d(t) \rangle = \int d\phi_d \chi_n^{\Phi*}(\phi_d, t) \phi_d \chi_n^{\Phi}(\phi_d, t), \quad (5.35)$$

where  $\chi_n^{\Phi}(\phi_d, t)$  was found by propagating on a grid. When the integral is computed at different times, the time dependence of the expectation value of the dihedral angle can be found. As a result, a solution of the two equations (5.31) and (5.34) gives us  $\langle \phi_d \rangle$  and  $\Phi$  as functions of time.

## 5.7 Results: Time-dependent simulations

The simulations described below were carried out on a grid with the size of 1024 points. The time steps were chosen to be  $\tau/100$ , where  $\tau$  is the pulse length (FWHM). The time steps chosen to be smaller for the experiment [3], which uses a smaller  $\tau$ , because the pulse intensity is also larger in that experiment.

Our main interest is control of the dihedral angle, so let us look at the expectation value of  $\phi_d$  as a function of time. This is shown in figure 5.4 for a kick pulse intensity of  $5 \times 10^{12} \text{ W cm}^{-2}$ ,

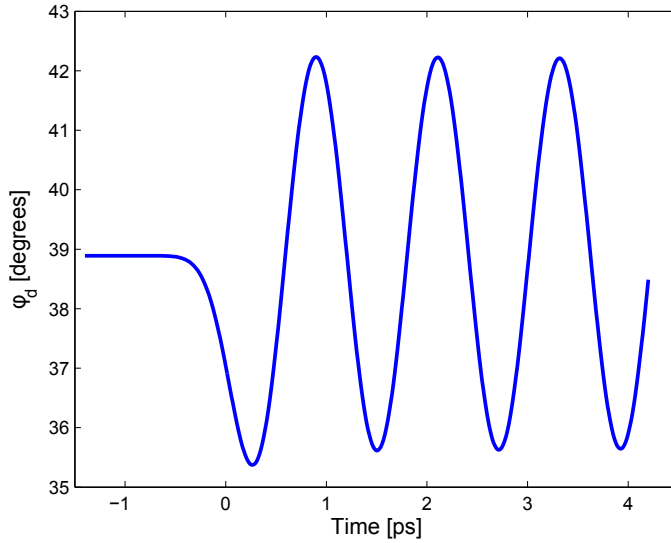


Figure 5.4: Theoretical expectation value of  $\phi_d$  as a function of time. The parameters of the kick pulse are the same as in the experiment in [1, 2], but the initial state is different: in these calculations,  $\Phi$  has a fixed value in the initial state, which was not the case in the experiment.

kick pulse length of 0.7 ps, and the initial state being a localized state with  $\langle\phi_d\rangle = 39^\circ$  and  $\Phi = 4.3^\circ$ . The kick pulse is centered around  $t = 0$ . This numerical simulation takes my computer less than a minute to do. The value of  $\Phi$  chosen here corresponds to having the SMPA of the molecule aligned with the X-axis (see figure 3.3). The reason for this choice is that the kick pulse will act to align these two axes, as described in section 3.2. The choice of parameters described here fits the experiment presented in [1, 2], except for the initial state. In the experiment, the initial state was delocalized in  $\Phi$ . Figure 5.4 shows oscillations in  $\langle\phi_d\rangle$  with an amplitude of  $3.1^\circ$  and a period of 1.22 ps. These oscillations show that the kick pulse can actually trigger torsional motion. In [1, 2] the oscillations were theoretically found to have an amplitude of  $2.45^\circ$  using the exact same model as has been described in this chapter. The calculations shown in this thesis have been thoroughly checked for convergence, so the difference is ascribed to the possible use of different fits to the torsional potential and the polarizability (see (3.1) and (4.28)). Because of this dependence on these parameters, the theoretical results are not expected to agree exactly with the experimental ones.

Oscillations in  $\langle\phi_d\rangle$  were also found experimentally, and they have a period that is about 1 ps. The amplitude is much smaller, though, about  $0.6^\circ$ . One reason for this discrepancy could be that  $\Phi$  is not fixed in the experiment, but it is very hard to quantify from this simulation alone whether this is the main reason. Another explanation could be that the kick pulse has a certain width in position. The peak intensity is only reached at the centre of the molecular beam, which means that we expect our theoretical calculations to give too large an amplitude of the oscillations. In the experiment, the alignment pulse does not align the molecules perfectly; only to a certain extent. This imperfect alignment might also play a role in diminishing the amplitude of the oscillations that are observed experimentally, because the model assumes perfect alignment. One final thing that could cause larger oscillations in theory than in exper-

iments is the fact that the model ignores the potential of the alignment pulse, as described in section 3.2.

A question one might ask is whether we can understand why the oscillations have a period of about 1.2 ps. This has to do with wave function revival, which was described in section 2.4. It was shown that expectation values are periodic with a period of

$$T_{\text{rev}} = \frac{2\pi}{\Delta E} \quad (5.36)$$

where  $\Delta E$  is the energy difference between the two closest energy levels. In this case, the energy difference is 3.45 meV according to (5.24) and the fact that  $E_0 = 1.725$  meV. Therefore, the period is

$$T_{\text{rev}} = 1.20 \text{ ps}. \quad (5.37)$$

The period (5.37) is consistent with what is observed in experiments (1.25 ps) and theory (1.22 ps) as described above.

The experimental ion images shown in section 3.3 can be integrated radially to obtain density plots, like figure 3.4 (b). This plot shows the probability density as a function of  $\phi_2$ , and similarly a probability density as a function of  $\phi_1$  could have been found by radially integrating the bromine ion image. The values of  $\phi_d$  and  $\Phi$  are found from such plots by fitting to Gaussian functions and transforming from  $(\phi_1, \phi_2)$  to  $(\phi_d, \Phi)$ . The experimentally found density plots can only be translated to  $\langle \phi_d \rangle$  and  $\Phi$  when they show a clear four-dot structure. They only do so for a few picoseconds after the kick pulse. Then, the angular distributions become so broad that the error of the fitted Gaussian functions is too large.

With this semiclassical model, one can also obtain density plots. The strategy is to find  $\langle \phi_d(t) \rangle$  and  $\Phi(t)$  for many different values of  $\Phi_0$ . In each case, the final value of  $\langle \phi_d \rangle$  and  $\Phi$  is transformed to find a final value of  $\phi_1$  and  $\phi_2$ . All of the final values of  $\phi_1$  and  $\phi_2$  are then plotted on a circle to make the plots resemble the ion images from the experiments. In the work behind this thesis, such calculations have not been done for this model, but it is shown in [1, 2] that one can reproduce such density plots theoretically in this way. These theoretical plots show that the angular distributions are more confined at 1.5 ps than at 2.5 ps, which is also observed experimentally. At large times, there is a difference between theory and experiments, most notably in the fact that the experimental delocalization happens faster for the fluorine ring than for the bromine ring, and that effect is not seen theoretically. There are many possible reasons for this difference, but the most compelling idea at this level of theory is that the separation between  $\Phi$  and  $\phi_d$  described in sections 5.2 and 5.3, breaks down at large times. The reason for this breakdown could be that the rotation happens on a larger time scale than vibration. This means that the molecule will only rotate slightly during the first few picoseconds after the kick pulse, and thus, it is a good approximation to separate rotation and torsion. At larger times, this approximation does not work as well. There are other possible explanations of the difference between theory and experiment, though. One idea is that the general model described in section 3.2 can not be used to describe this kind of behaviour. It builds on some approximations in itself, and these may also break down. Which explanation to use will be discussed further in chapter 8.

In the more recent experiment described in [3], the measurements were reproduced for an initial state that was 3D-aligned, as described in section 3.3. This corresponds to localization in both  $\Phi$  and  $\phi_d$ , and one would therefore expect such an experiment to yield results that are closer to what is found using the model described in this chapter. This turns out to be true when it comes to the oscillations in  $\langle \phi_d \rangle$ . The kick pulse has been made more intense and more narrow for this experiment, with a peak intensity of  $2 \times 10^{13} \text{ W cm}^{-2}$  and a pulse length

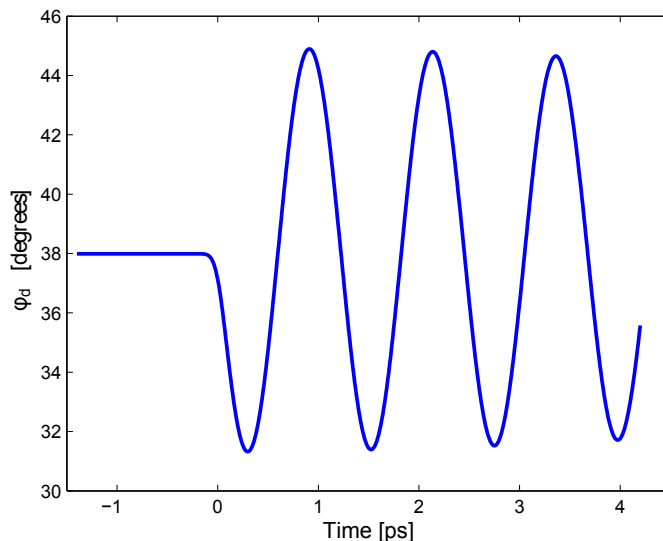


Figure 5.5: Oscillations in  $\langle \phi_d \rangle$  from a simulation that is designed to fit the experiment in [3]. The laser pulse has a peak intensity of  $2 \times 10^{13} \text{ W cm}^{-2}$  and a pulse length of 0.2 ps, and  $0.9^\circ$  has been subtracted from the simulation result. The amplitude of the oscillations is about twice of what is seen experimentally in [3].

of 0.2 ps. This changes the theoretical amplitude of the oscillation from  $3.1^\circ$  to  $6.8^\circ$ , as can be seen in figure 5.5. The experimentally found amplitude is about  $3^\circ$ , so it is still not quite the same as the theoretical value. At least the results have now come closer to each other, only deviating by a factor of two, not by a factor of almost ten.

As a side remark, it is noted that the theoretical results of [2] show that only the first few torsional states are occupied. This is one of the reasons why it is a good approximation to use the torsional potential of DFDBrBPh when describing DFDBrCNBPh. Such a result was not found in the calculations done in this thesis, because they were done on a grid and not in a basis.

## 5.8 Problems with the semiclassical model

The experimental results are not perfectly described by the theory, especially not at large times. For instance, the delocalization process in theoretical calculations in [1, 2] is different from what is seen experimentally. There are probably many reasons why these differences are seen, for example a lower kick pulse intensity in experiments due to focal width of the laser beam. It would be interesting if some of the errors could be ascribed to problems with the theory of this chapter, and such problems do indeed exist. The first problem is that one has to fix  $\Phi$ , and this is not done in all experiments. It seems that it is possible to obtain larger oscillations in  $\langle \phi_d \rangle$  by fixing  $\Phi$ , and since one wants better control of the dihedral angle, this is the way to go. Therefore, this problem is not too significant.

Another problem is that  $\Phi$  is treated classically. The importance of this will be investigated in the chapters to come.

The separation between  $\Phi$  and  $\phi_d$  is not handled very accurately in this chapter. In fact, the separation breaks down at large times, so  $\Phi$  and  $\phi_d$  seem to couple to each other. The breakdown can also be thought of as a consequence of propagating in time with boundary conditions that are only almost correct. The results may be good for the first period of time, but the error keeps on growing. Other arguments for the breakdown are given in [3].

Other approximations are used in section 3.2 when showing the main ideas of modelling the experiments [1, 2, 3]. One of these approximations is the total 1D alignment of the molecules. This may cause a small error on the theoretical results, and there could also be errors because the potential of the alignment pulse is completely ignored in the theory.

Some of these approximations can be avoided by not using the  $(\phi_d, \Phi)$ -coordinates, which will in fact be the strategy of the following chapters. This approach allows for a test of the approximations that are specific for the semiclassical model.

## 5.9 Summary

In this chapter, we have used a semiclassical model to describe the experiments in [1, 2, 3]. It is based on separating the torsional and rotational motion and then treating the rotational motion classically. Since one coordinate is treated classically, the problem is reduced to a 1D quantum problem, which is relatively simple to solve numerically. The results seem reasonable, but there are differences between experiment and theory. An improvement of the model is needed, for us to obtain further understanding of the problem. In the next chapters, we will look at improvements of the theoretical model that can improve the results found here.



## Chapter 6

# 2D quantum mechanical models: The torsional potential

The goal of this chapter and the next is to devise a theory that can give better agreement with the experimental results than the model described in chapter 5. The idea is to start from the basics developed in section 3.2, and then proceed in a different direction than what was done in chapter 5. We will look at a 2D quantum mechanical model of the molecule; we do not want to treat one of the angles classically. This approach leads to a model that will be called the 2D quantum model or just the 2D model, in contrast to the semiclassical 1D model.

In this chapter, we look at the Hamiltonian without the kick pulse, which in  $(\phi_1, \phi_2)$ -coordinates reads

$$H = -\frac{1}{2I_1} \frac{\partial^2}{\partial \phi_1^2} - \frac{1}{2I_2} \frac{\partial^2}{\partial \phi_2^2} + V_{\text{tor}}(\phi_1 - \phi_2), \quad (6.1)$$

and in  $(\phi_d, \Phi)$ -coordinates it reads

$$H = -\frac{1}{2I} \frac{\partial^2}{\partial \Phi^2} - \frac{1}{2I_{\text{rel}}} \frac{\partial^2}{\partial \phi_d^2} + V_{\text{tor}}(\phi_d) = H_{\Phi} + H_{\phi_d}. \quad (6.2)$$

These two equations are fully equivalent and based on precisely the same approximations. We will be interested in solving the time-independent Schrödinger equation,  $H\psi = E\psi$ , i.e. finding eigenvalues and eigenvectors of  $H$ . In chapter 7, the solutions obtained here will be used to solve the time-dependent Schrödinger equation where the kick pulse is included.

The problem will be solved with different sets of angles used to describe the system. In the first section, the angles  $(\phi_d, \Phi)$  will be used, just like in chapter 5. This time both angles will be treated quantum mechanically, though. The eigenstates and eigenvalues of (6.2) that will be found are only approximate, since the separation of the Hamiltonian is not exact. The second section uses the angles  $(\phi_1, \phi_2)$ , and the results obtained here will be exact eigenstates and eigenvalues of (6.1). The only approximations they rely on are the ones described in section 3.2, where the first steps were taken in modelling the molecule. In the third section, a third choice of angles that will also yield exact eigenstates and eigenvalues of (6.1) is described. Section 6.4 contains a detailed study of the  $(\phi_d, \Phi)$ -coordinates. This last section will explain why the energies calculated using  $(\phi_d, \Phi)$  are very similar to the ones found using  $(\phi_1, \phi_2)$ . We will show how an exact separation of  $\phi_d$  and  $\Phi$  can be achieved.

## 6.1 The dihedral angle $\phi_d$ and the overall rotational angle $\Phi$

In chapter 5, we used the two angles  $\phi_d$  and  $\Phi$  in our description of the molecule, where  $\Phi$  was treated classically. The simplest generalization is to make no assumption about a classical behaviour of  $\Phi$ , so that case is the first for us to study.

The Hamiltonian (without the kick pulse) in  $(\phi_d, \Phi)$ -coordinates, (6.2), is a sum of a  $\Phi$ -dependent part and a  $\phi_d$ -dependent part. We assume that  $\phi_d$  and  $\Phi$  are independent and both  $2\pi$ -periodic, just like in chapter 5. Then the Hamiltonian can be separated, as described in section 5.3. This time both equations in (5.12) will be treated quantum mechanically. The solutions of the second equation of (5.12) have been discussed in chapter 5, so in this section we can focus on the first equation of (5.12). It is essentially the same equation as (5.15), which we have already solved analytically in section 5.4. The solution can be written in two ways:

$$X(\Phi) = A \sin(m\Phi) + B \cos(m\Phi) \quad \text{or} \quad X(\Phi) = A \exp(im\Phi) + B \exp(-im\Phi), \quad (6.3)$$

where  $A$  and  $B$  are constants, and  $m = \sqrt{2I\alpha}$ . The constant  $\alpha$ , which we might think of as a rotational energy, is thus given by

$$\alpha = m^2/2I. \quad (6.4)$$

Because of the  $2\pi$ -periodic boundary conditions,  $m \in \mathbb{Z}$ . We can think of  $m$  as the  $\Phi$  quantum number. The total energy is given by  $E = \alpha + \beta$ , and  $\beta$  has already been found in section 5.5. It is approximately given by (5.24). As a result, we can find the total energy by adding (5.24) and (6.4), i.e.

$$E_{j,m} = 2E_{0,0}(j + 1/2) + \frac{1}{2I}m^2, \quad j \in \mathbb{N} \cup \{0\}, \quad m \in \mathbb{Z} \quad (6.5)$$

where  $E_{0,0}$  is the ground state energy. The index  $j$  tells which fourfold degenerate  $\phi_d$ -manifold the state belongs to, just like in (5.24). Note that  $m = 0$  has a fourfold degeneracy, but for all other values of  $m$  there is an eightfold degeneracy. This is because  $m$  and  $-m$  give the same energy. The energies found here will later be compared with the results of other theories.

The eigenstates will be the same as in section 5.5, except that they are multiplied by (6.3).

For comparison with a discussion in section 6.4, we combine (6.4) with (5.12) to find:

$$\left[ \frac{m^2}{2I} - \frac{1}{2I_{\text{rel}}} \frac{\partial^2}{\partial \phi_d^2} + V_{\text{tor}}(\phi_d) \right] \chi(\phi_d) = E\chi(\phi_d). \quad (6.6)$$

This is way of formulating the two equations (5.12) as just one.

## 6.2 Simple coordinates: $\phi_1$ and $\phi_2$

We are on a path to get rid of some of the approximations made in chapter 5. The next approximation to avoid is the one regarding the the boundary conditions of  $\Phi$  and  $\phi_d$ . In this section, it will be avoided by choosing a different set of coordinates,  $(\phi_1, \phi_2)$  (see figure 3.3). These coordinates are easier to use, since we know that they are both  $2\pi$ -periodic, and the results will therefore be more accurate than what was found in the previous section. The disadvantage is that the equation to solve becomes more difficult to handle, and furthermore, it may not be so simple to interpret the results in terms of torsion and rotation.

The equation we want to solve is

$$\left( -\frac{1}{2I_1} \frac{\partial^2}{\partial \phi_1^2} - \frac{1}{2I_2} \frac{\partial^2}{\partial \phi_2^2} + V_{\text{tor}}(\phi_1 - \phi_2) \right) \psi = E\psi \quad (6.7)$$

It is possible to solve this 2D time-independent Schrödinger equation in  $(\phi_1, \phi_2)$ -coordinates. The Hamiltonian (6.1) is not separable, so one has to deal with a 2D quantum mechanical problem. Such a problem is more complicated to solve numerically than the 1D problem solved in chapter 5, but it can be done. The approach to be used is the same as in section 5.4, generalized to two dimensions. The first step is to solve the problem

$$H_0\psi_0(\phi_1, \phi_2) = \epsilon_0\psi_0(\phi_1, \phi_2), \quad (6.8)$$

where

$$H_0 = -\frac{1}{2I_1} \frac{\partial^2}{\partial \phi_1^2} - \frac{1}{2I_2} \frac{\partial^2}{\partial \phi_2^2} \quad (6.9)$$

and  $\epsilon_0$  is the corresponding energy. The solutions will be used as a basis for solving (6.7). Just like in section 5.4, the solutions to the non-interacting problem can be written as either sines and cosines or as exponential functions. This time, we choose the exponential basis, because it is simpler to work with. So the basis for solving (6.7) is

$$\left\{ \frac{1}{2\pi} \exp(im_1\phi_1) \exp(im_2\phi_2) \right\}, \quad m_1, m_2 \in \mathbb{Z}. \quad (6.10)$$

The quantum state corresponding to the basis function  $\frac{1}{2\pi} \exp(im_1\phi_1) \exp(im_2\phi_2)$  will be denoted  $|m_1, m_2\rangle$ .

Now, we want to write the Hamiltonian (6.1) as a matrix in this basis. How this works in general is explained in section 5.4. The matrix can then be diagonalized using the *eig* or *eigs* command in MATLAB. Such a calculation is repeated for an increasing number of basis states until convergence is reached. In section 5.4, the basis functions were ordered by the value of  $|m|$ . Here, we have both  $m_1$  and  $m_2$  to focus on, so the choice of ordering becomes slightly more complicated. In this thesis, it has been chosen to order the states by the maximum value of  $|m_1|$  and  $|m_2|$ .

Before the numerical solution of (6.7) can commence, we need to do a calculation of the matrix elements of the Hamiltonian. This has been done, and it is shown in detail in appendix A. Here, the result is just shown:

$$\begin{aligned} \langle m_1, m_2 | V_{\text{tor}} | m_3, m_4 \rangle = & \frac{a}{2} (\delta_{m_3-m_1,4} \delta_{m_4-m_2,-4} + \delta_{m_3-m_1,-4} \delta_{m_4-m_2,4}) \\ & + \frac{b}{2} (\delta_{m_3-m_1,2} \delta_{m_4-m_2,-2} + \delta_{m_3-m_1,-2} \delta_{m_4-m_2,2}) \\ & + \frac{d}{2} (\delta_{m_3-m_1,6} \delta_{m_4-m_2,-6} + \delta_{m_3-m_1,-6} \delta_{m_4-m_2,6}) \\ & + \frac{e}{2} (\delta_{m_3-m_1,8} \delta_{m_4-m_2,-8} + \delta_{m_3-m_1,-8} \delta_{m_4-m_2,8}) + c \delta_{m_3,m_1} \delta_{m_4,m_2}. \end{aligned}$$

In this two dimensional case, the number of basis states needed for convergence of the lower states is rather large. In one dimension, the number of needed states was about 100, so in two dimensions one could expect that 10,000 basis states is needed to ensure convergence. This turns out to be true, so the problem at hand is diagonalizing a  $10,000 \times 10,000$  matrix, which

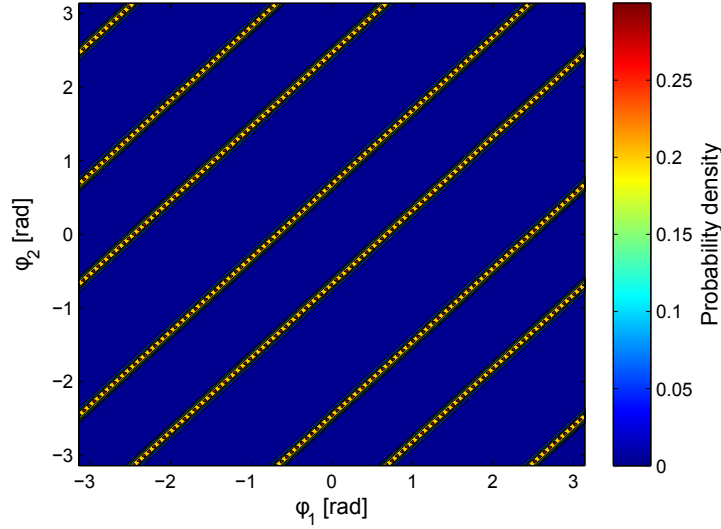


Figure 6.1: A plot of the norm squared of one of the eigenstates of (6.1) with the lowest energy. Note that the state only has peaks in the minima of the torsional potential, just like figure 5.3. It has an energy of 1.725 meV above the bottom of torsional potential.

takes a long time. The matrix has rather many zero entries, as is seen from the calculation above. This means that it is a computational advantage to use it as a sparse matrix; only saving the non-zero entries. One can then use the MATLAB routine *eigs* to find some of the eigenstates and eigenvalues; not them all. This can be done faster than finding them all, and in a few minutes, one can find many eigenstates.

Equation (6.7) has been solved using the method described here, and the results will now be compared with previous calculations. The four lowest states are approximately degenerate, which was also found using the 1D semiclassical model of chapter 5. The norm squared of the wave function  $\psi_n$  for one of these states can be seen in figure 6.1. Their energy is 1.725 meV above the minimum of the torsional potential, which is exactly the same as was found in section 5.5. The energy differences between the four lowest states are of the order of  $10^{-8}$  eV, which is a bit larger than the result of section 5.5. The state seen in figure 6.1 resembles the ones seen on 5.3, it has just been transformed to  $(\phi_1, \phi_2)$ -coordinates. The energies can be seen in figure 6.2, where they are compared to the energies found using the  $(\phi_d, \Phi)$ -coordinates. These energies are practically the same as the ones found previously. The boundary conditions for  $\Phi$  and  $\phi_d$  were not correct in the  $(\phi_d, \Phi)$ -model, so it actually seems strange that the same energies are found. This will be explained in section 6.4. The approximate degeneracies are not the same as the ones found in section 6.1, though. For the new-found states, there is a general fourfold approximate degeneracy, but many of the previous states were eightfold approximately degenerate. This makes sense, because the periodicities of  $(\phi_d, \Phi)$  used in section 6.1 do not correspond to the ones used in this section. Based on (6.5), the energies found using  $(\phi_1, \phi_2)$  can approximately be written as

$$E_{j,m} = 2E_{0,0}(j + 1/2) + \frac{1}{2I}m^2, \quad j \in \mathbb{N} \cup \{0\}, \quad m \in \mathbb{N} \cup \{0\}, \quad (6.11)$$

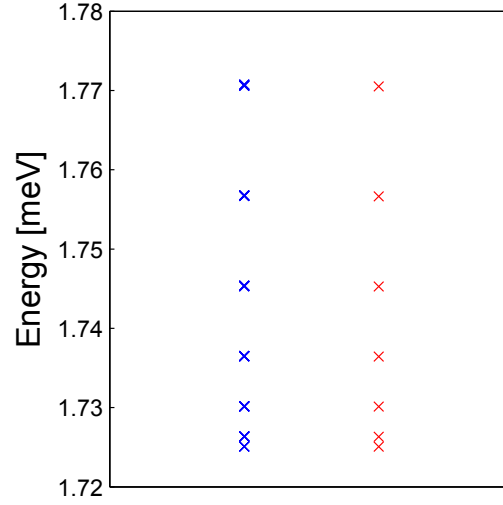


Figure 6.2: Energies found using the coordinates  $(\phi_1, \phi_2)$  (blue) compared to the energies found using the coordinates  $(\phi_d, \Phi)$  (red). Only the lowest energies are shown. It is seen that the energies of the two methods are almost identical. The only real difference is the degeneracies, and they can not be seen in this figure. The zero point for energy is chosen to be the bottom of the torsional potential wells.

This approximation of the energies is at least true for the lowest  $j$ -states.

From the four eigenstates with the lowest energy, it is possible to create states that are localized in  $\phi_d$  and almost eigenstates, just as in chapter 5. These 2D states that are localized in  $\phi_d$  are denoted by  $|L_{j,m}^{(i)}\rangle$ , where the  $i$  tells which of the wells in the torsional potential the state is localized in. Just as in chapter 5, the localized states are a sum of four delocalized states,

$$|L_{j,m}^{(i)}\rangle = \sum_n c_{j,m}^{(i)} \psi_n, \quad (6.12)$$

where the sum in  $n$  only includes the states that have an energy of approximately  $E_{j,m}$ . In fact, we do not need to do a new calculation to find the coefficients  $c_{j,m}^{(i)}$ . The eigenstates are found in an exponential basis, and we also solved the 1D problem in such a basis. Therefore, we can just re-use the coefficients from the 1D problem in section 5.5 where the exponential basis was used.

One of the localized states can be seen in figure 6.3. It is the one with  $\langle \phi_d \rangle = 39^\circ = 0.69$  rad. As we can see, there are two lines. One of them is at a value of  $\phi_d = 0.69$  rad, but the other is at  $\phi_d = -5.6$  rad  $= -321^\circ$ . These two lines correspond to the same value of  $\phi_d$ , because the upper line is just a continuation of the lower one, when the boundary conditions are kept in mind. We note that the  $\phi_d$ -behaviour is not always obvious from a plot in  $(\phi_1, \phi_2)$ -coordinates. The problem is that  $\phi_d$  runs from  $-2\pi$  to  $2\pi$ . On the other hand, we cannot use  $(\phi_d, \Phi)$ -coordinates to do the calculations, since we do not know a good way of incorporating the

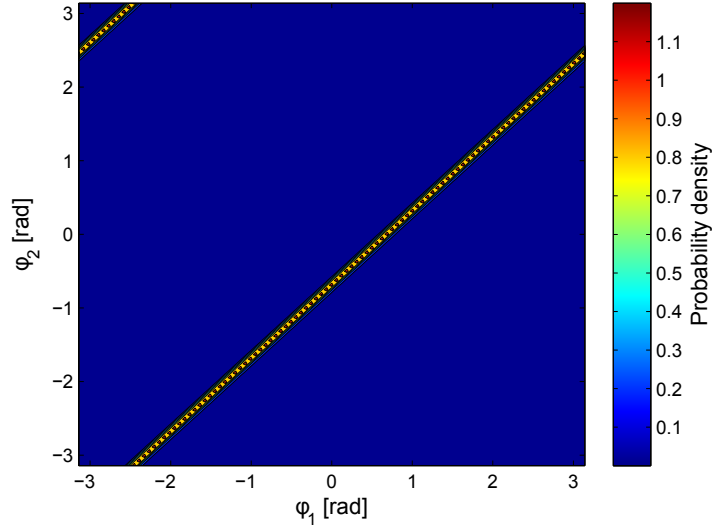


Figure 6.3: The norm squared of a localized state in  $\phi_d$  for  $\langle \phi_d \rangle = 39^\circ$ , which is denoted  $|L_{0,0}^{(1)}\rangle$ . This state is a superposition of the four lowest eigenstates of the Hamiltonian without the kick pulse. By making linear combinations of the eigenstates, one can make four different localized states, localized in the four different wells of the torsional potential.

correct boundary conditions. The solution is to use  $(\phi_1, \phi_2)$ -coordinates for the calculations and transform to  $(\phi_d, \Phi)$  when we need to interpret the results.

In this section, we have found exact eigenfunctions and eigenvalues of the Hamiltonian without the kick pulse, (6.1). This is a more accurate result than what was found in the previous section, since no approximations are made. With these more precise eigenfunctions in place, we can now proceed to solve the time-dependent Schrödinger equation including the kick pulse, which will be done in chapter 7. Before doing that, we will discuss another possible choice of coordinates (section 6.3) and study the  $(\phi_d, \Phi)$ -coordinates a bit further (section 6.4). This will show why the energies of the model in section 6.1 are the same as the energies found in this section, even though an approximate separation of  $\phi_d$  and  $\Phi$  is used.

### 6.3 Another choice of coordinates

Other types of coordinates can be used to describe the system. Here, a choice will be shown which has the possibility of simplifying the numerical calculations. The coordinates are

$$\phi_d = \phi_1 - \phi_2 \quad (6.13)$$

$$\phi_s = \frac{1}{2}(\phi_1 + \phi_2). \quad (6.14)$$

This choice keeps  $\phi_d$  as one of the coordinates, and we will see that exact eigenvalues of the Hamiltonian (6.1) can be found in a simple way.

In these new coordinates, the angle  $\phi_d$  is  $4\pi$ -periodic and  $\phi_s$  is  $2\pi$ -periodic. There is one problem, though: These periodicities do not exactly correspond to the periodicities of  $\phi_1$  and

$\phi_2$ . From the periodicities of  $\phi_1$  and  $\phi_2$  it is seen that a change in  $\phi_d$  by  $2\pi$  and in  $\phi_s$  by  $\pi$ , will take us back to the same point. That is not included in the periodicities of  $\phi_d$  and  $\phi_s$ . As a result, a solution found in this way will not necessarily give the correct number of degenerate states.

Another price to pay is that  $\phi_s$  does not correspond to rotation of the entire molecule. It would do so if the two rings had the same moment of inertia, but they are different. Therefore this is not a separation of torsion and rotation, it is just another way to find the eigenstates of the Hamiltonian without the kick pulse. Since the eigenstates have already been found using the method of section 6.2, there is no need to find them in this new way. The main use of this section is therefore to show that it is possible to find the eigenstates with less numerical calculations.

Now, let us look at the formal solution in these coordinates:  $\exp(im\phi_s)$  ( $m$  integer) is an eigenstate for  $L_z$ , and  $L_z = -i\frac{\partial}{\partial\phi_1} - i\frac{\partial}{\partial\phi_2}$  can be shown to commute with the Hamiltonian (6.1). Common eigenstates of  $L_z$  and the Hamiltonian will thus exist, and furthermore, all eigenstates of  $L_z$  can be written as

$$\exp(im_1\phi_1 + im_2\phi_2) = \exp(i(m_1 + m_2)\phi_s) \exp\left(i\frac{m_1 - m_2}{2}\phi_d\right) \quad (6.15)$$

where  $m_1, m_2 \in \mathbb{Z}$ . These facts lead to the conclusion that all eigenfunctions of (6.1) can be written as

$$\exp(im\phi_s)f^m(\phi_d), \quad m \in \mathbb{Z} \quad (6.16)$$

When this is inserted into the Hamiltonian one finds

$$-\frac{1}{2I_{\text{rel}}}\frac{\partial^2 f}{\partial\phi_d^2} - \frac{im}{2}\left(\frac{1}{I_1} - \frac{1}{I_2}\right)\frac{\partial f}{\partial\phi_d} + V_{\text{tor}}(\phi_d)f(\phi_d) = \left[E - \frac{m^2}{8I_{\text{rel}}}\right]f(\phi_d). \quad (6.17)$$

The system is thus well-described by a free particle in  $\phi_s$  and the solution to a 1D-equation in  $\phi_d$ . There are many solutions for each value of  $m$ . They will be labelled by  $k$  as  $f_k^m$ , so

$$Hf_k^m(\phi_d) = E_k f_k^m(\phi_d) \quad (6.18)$$

where  $H$  is (6.1). The solution of equation (6.18) is a correct solution of the time-independent Schrödinger equation of (6.1), except for the degeneracy. We only need to solve a 1D equation to obtain this solution. This means that fewer basis states will be needed in the calculations, which will lead to smaller matrices. The approach described in this section has not been pursued very far in this thesis, because the entire problem was solvable in  $(\phi_1, \phi_2)$ -coordinates, as will be shown in the next chapter.

## 6.4 Correct boundary conditions and periodicities of $\phi_d$ and $\Phi$

In the previous sections, and especially in chapter 5, we have used the coordinates  $(\phi_d, \Phi)$ , but it has been unclear how the periodicities and boundary conditions should be. They will be derived in this section. The derivation is a general extension of the theory developed in [41] but used on a completely different physical problem.

The equation of interest is still the time independent Schrödinger equation without the kick pulse, (6.1).

We will end up with an equation that is very similar to (6.6), and thus explains why the energies previously found using the  $(\phi_d, \Phi)$ -coordinates are so similar to the ones found using the coordinates  $(\phi_1, \phi_2)$ .

The system is described by  $\phi_1$  and  $\phi_2$ , which are both  $2\pi$ -periodic. The Hamiltonian (6.1) is therefore  $2\pi$ -periodic in both  $\phi_1$  and  $\phi_2$ . Now, we will change to another set of coordinates

$$\phi_d = \phi_1 - \phi_2, \quad \Phi = (1 - \eta)\phi_1 + \eta\phi_2, \quad (6.19)$$

as described in section 5.2. The inverse transformation is

$$\phi_1 = \Phi + \eta\phi_d, \quad \phi_2 = \Phi - (1 - \eta)\phi_d. \quad (6.20)$$

The challenge is to handle the periodicity of these new coordinates correctly. In sections 5.2 and 6.1, we assumed that  $\phi_d$  and  $\Phi$  were both  $2\pi$ -periodic. This is not the case, as discussed earlier.

The Hamiltonian can be rewritten in terms of  $\phi_d$  and  $\Phi$ , as has already been done in equation (6.2). The periodicity in  $\phi_1$  leads to

$$H(\phi_d, \Phi) = H(\phi_d \pm 2\pi, \Phi \pm (1 - \eta)2\pi), \quad (6.21)$$

and the periodicity in  $\phi_2$  gives us

$$H(\phi_d, \Phi) = H(\phi_d \mp 2\pi, \Phi \pm \eta 2\pi). \quad (6.22)$$

The restrictions in (6.21) and (6.22) are not enough to keep the symmetry intact when doing the coordinate transformation, but they are necessary conditions. The approach followed here is to start out with this periodicity, and then, one can pick the solutions that fulfil the total symmetry in the end.

Let us assume that  $\eta$  and  $1 - \eta$  are commensurable, meaning that numbers  $M$  and  $N$  exist such that

$$\eta M = (1 - \eta)N \quad (6.23)$$

This is definitely true in any numerical implementation, since  $\eta$  will be a rational number. It allows us to translate (6.21) and (6.22) into conditions on  $\phi_d$  and  $\Phi$ . If we start from  $H(\phi_d, \Phi)$  and use (6.21) and then afterwards use (6.22), we arrive at

$$H(\phi_d, \Phi) = H(\phi_d, \Phi \pm 2\pi). \quad (6.24)$$

This shows that  $\Phi$  is  $2\pi$  periodic. The periodicity for  $\phi_d$  is found by applying (6.21)  $N$  times and then (6.22)  $M$  times, but with opposite signs. This gives

$$H(\phi_d, \Phi) = H(\phi_d \pm (M + N)2\pi, \Phi), \quad (6.25)$$

so  $\phi_d$  is  $(M + N)2\pi$ -periodic. These periodicities of  $\phi_d$  and  $\Phi$  are not sufficient to describe the original  $2\pi$ -periodicity of  $\phi_1$  and  $\phi_2$ , but they are a necessary for the periodicities in  $(\phi_1, \phi_2)$  to be fulfilled.

### The area of interest in the $(\phi_d, \Phi)$ -plane

Now, we have established a necessary periodicity of  $\phi_d$  and  $\Phi$  that does not in itself correspond to the boundary conditions of the physical system. There are further restrictions to be



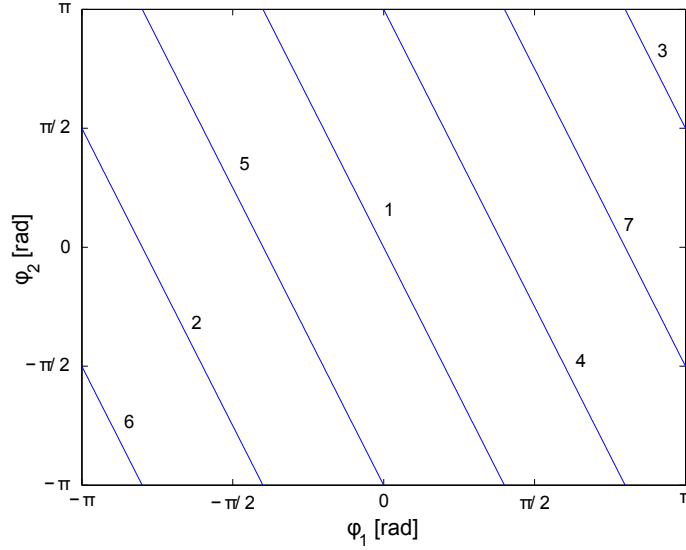


Figure 6.4: This figure shows how the  $\phi_d$ -axis can be folded into the area (6.26) in the  $(\phi_1, \phi_2)$ -plane. Here it is done for  $N = 2$  and  $M = 5$ . We start with the line labelled by 1 and move upwards. When the top is reached, the  $2\pi$ -periodicity of  $\phi_2$  is used to move on to line number 2. Using the periodicities of  $\phi_1$  and  $\phi_2$  we can move onto line 3 and 4 and so on, until the 7th line leads us back to line number 1.

made, and one of these is to look at a smaller area in the  $(\phi_d, \Phi)$ -plane than demanded by the periodicity. In the  $(\phi_1, \phi_2)$ -plane, the area of interest is the cartesian product

$$]-\pi, \pi[ \times ]-\pi, \pi[. \quad (6.26)$$

The rest of the  $(\phi_1, \phi_2)$ -plane consists of copies of this area. Directly mapped to the  $(\phi_d, \Phi)$ -plane, (6.26) is not a cartesian product, as seen in figure 5.2. Cartesian products are easier to handle than such complicated areas.

If we follow the  $\phi_d$ -axis through  $M$  vertical and  $N$  horizontal copies of (6.26), we return to our starting point. This is because  $\phi_d$  is  $(M + N)2\pi$ -periodic, as described in (6.25). The line created by following the  $\phi_d$ -axis can be folded into the area (6.26), which is seen in figure 6.4 for the case  $M = 5$  and  $N = 2$ . For the molecule we are studying, the numbers  $M$  and  $N$  are much larger, since the moments of inertia of the two rings are  $I_1 = 8911925$  a.u. and  $I_2 = 1864705$  a.u.. so there will be many more lines than the ones seen in figure 6.4.

The first line above the  $\phi_d$ -axis (line 4 in figure 6.4) is described by

$$\phi_2 = \frac{2\pi}{N} + \frac{\eta - 1}{\eta} \phi_1. \quad (6.27)$$

In total, we see a lot of parallel lines that are separated by  $2\pi/N$  in the  $\phi_2$ -coordinate. Each line has a constant value of  $\Phi$ . Using (6.27), we see that the first line above the  $\phi_d$ -axis has a value of

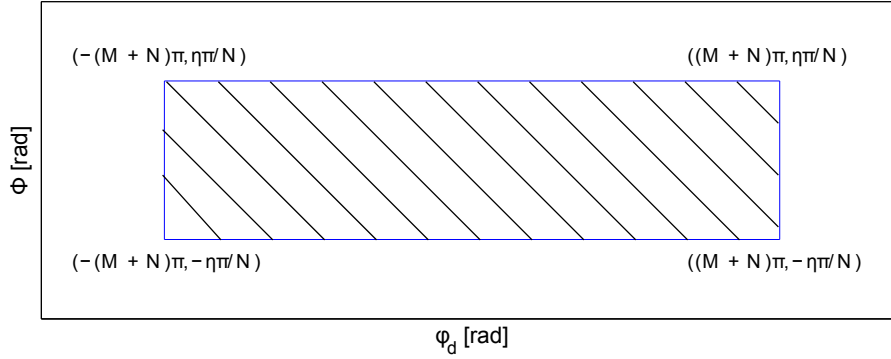


Figure 6.5: The solution of the Schrödinger equation can be restricted to this hatched area in the  $(\phi_d, \Phi)$ -plane. This does not mean that  $\Phi$  is periodic with a period of  $\frac{\eta 2\pi}{N}$ . One has to change  $\phi_d$  by  $(M + N)2\pi$  or change both  $\Phi$  and  $\phi_d$  to return to the initial orientation of the two rings of the molecule.

$$\Phi = (1 - \eta)\phi_1 + \eta\phi_2 = \frac{\eta 2\pi}{N}. \quad (6.28)$$

In the  $(\phi_d, \Phi)$ -plane, these parallel lines will be vertical and separated by a distance of  $\frac{\eta 2\pi}{N}$ . If we place a band of width  $\frac{\eta 2\pi}{N}$  symmetrically around the lines, it is possible to cover the entire area described by (6.26). The relevant area in the  $(\phi_d, \Phi)$ -plane therefore becomes

$$\left] - (M + N)\pi, (M + N)\pi \left[ \times \left] - \frac{\eta\pi}{N}, \frac{\eta\pi}{N} \left[ , \quad (6.29)$$

which is seen in figure 6.5. This is a cartesian product. Notice that the relevant interval in  $\Phi$  is smaller than the periodicity in (6.24) would lead to. The points  $(0, -\eta\pi/N)$  and  $(0, \eta\pi/N)$  do not correspond to the same orientation of the two rings of the molecule, since the general periodicity of  $\Phi$  is  $2\pi$ . Because (6.29) shows the relevant area, the point  $(0, -\eta\pi/N)$  must correspond to the same orientation as some other point in (6.29). This other point is found by changing  $\Phi$  from  $-\eta\pi/N$  to  $\eta\pi/N$  and also changing  $\phi_d$ . In other words, there is another restriction on the Hamiltonian than (6.24) and (6.25). This restriction will not be derived in detail here.

### Solution of the Schrödinger equation in $(\phi_d, \Phi)$ -coordinates

As seen from (6.2), the time independent Schrödinger equation without the kick pulse has the following form in  $(\phi_d, \Phi)$ -coordinates:

$$\left( -\frac{1}{2I} \frac{\partial^2}{\partial \Phi^2} - \frac{1}{2I_{\text{rel}}} \frac{\partial^2}{\partial \phi_d^2} + V_{\text{tor}}(\phi_d) \right) \Psi(\phi_d, \Phi) = E\Psi(\phi_d, \Phi). \quad (6.30)$$

One of the reasons why this is a good choice of coordinates is that the Hamiltonian does not contain any terms that are dependent on both  $\phi_d$  and  $\Phi$ . The potential  $V_{\text{tor}}(\phi_d)$  is  $2\pi$ -periodic, and the solution  $\Psi(\phi_d, \Phi)$  has to fulfil the same periodicity conditions as the Hamiltonian

does, which is described by (6.24) and (6.25). So  $\Psi(\phi_d, \Phi)$  is  $(M + N)2\pi$ -periodic in  $\phi_d$  and  $2\pi$ -periodic in  $\Phi$ . The solution also has to fulfil an extra condition, such that the original boundary conditions of  $\phi_1$  and  $\phi_2$  are met, and the idea here is to find solutions that fit with the periodicities of  $\phi_d$  and  $\Phi$ , and then afterwards to choose the solutions that fulfil the extra condition.

Since  $\Psi(\phi_d, \Phi)$  is  $2\pi$ -periodic in  $\Phi$ , it can be expanded in plane waves in  $\Phi$ :

$$\Psi(\phi_d, \Phi) = \sum_k c_k e^{ik\Phi} \psi_k(\phi_d), \quad (6.31)$$

where  $k$  is an integer, and  $\psi_k(\phi_d)$  is a  $(M + N)2\pi$ -periodic function. The only  $\Phi$ -dependent term in (6.30) is the kinetic term, and it does not couple different plane waves to each other. This means that each term in (6.31) is in itself a solution to (6.30). As a consequence, we can make the ansatz

$$\Psi(\phi_d, \Phi) = e^{ik\Phi} \psi_k(\phi_d). \quad (6.32)$$

Notice that this is only possible because  $V_{\text{tor}}$  depends solely on  $\phi_d$ . Inserting this ansatz into (6.30) gives

$$\left( \frac{k^2}{2I} - \frac{1}{2I_{\text{rel}}} \frac{\partial^2}{\partial \phi_d^2} + V_{\text{tor}}(\phi_d) \right) \psi_k(\phi_d) = E \psi_k(\phi_d). \quad (6.33)$$

This equation is almost the same as (6.6), the only difference being the periodicity of  $\psi_k(\phi_d)$ . The next thing to do is to look more into this periodicity of  $\phi_d$ . Because  $\psi_k(\phi_d)$  is  $(M + N)2\pi$ -periodic and  $V_{\text{tor}}(\phi_d)$  is  $2\pi$ -periodic, we can apply Bloch's theorem. It states that the solution can be written as a product of a plane wave and a function with the same periodicity as  $V_{\text{tor}}(\phi_d)$  [42]. In other words,

$$\psi_k(\phi_d, \Phi) = e^{il\phi_d/(M+N)} \chi_k(\phi_d). \quad (6.34)$$

$\chi_k(\phi_d)$  is a  $2\pi$ -periodic function, and  $l$  is an integer. One can find restrictions on  $k$  and  $l$  by using the periodicity of the total wave function  $\Psi(\phi_d, \Phi)$ , but that will not be done here. These restrictions show that for each  $k$  there is a number of allowed values of  $l$ . The main result of this section is that a separation between  $\phi_d$  and  $\Phi$  has been achieved, and this will only be used for interpretation, not for calculations.

Now, we will insert (6.34) into (6.33). A few steps of calculation show that (6.33) becomes

$$\left[ \frac{k^2}{2I} - \frac{1}{2I_{\text{rel}}} \left( -\frac{l^2}{(M+N)^2} + \frac{2il}{M+N} \frac{\partial}{\partial \phi_d} + \frac{\partial^2}{\partial \phi_d^2} \right) + V_{\text{tor}}(\phi_d) \right] \chi_k(\phi_d) = E \chi_k(\phi_d). \quad (6.35)$$

The two first terms in the rounded brackets are damped by a factor of  $(M + N)^{-2}$  and  $(M + N)^{-1}$  respectively. For the molecule of interest, these numbers are very small, because  $M$  and  $N$  are large. As a result, the two terms can be neglected. The allowed  $l$ -indices depend on  $k$ , so by neglecting these two terms we have removed the  $k$ -dependence of  $\chi_k(\phi_d)$ . Now, the only role of  $k$  is to raise the energy by a constant, and an overall change of the zero point energy does not alter the eigenfunctions. This means that (6.35) reduces to (6.6), which was found assuming that  $\Phi$  and  $\phi_d$  were both  $2\pi$ -periodic. Since  $\chi_k(\phi_d)$  is  $2\pi$ -periodic, the equations are exactly the same. This shows that (6.6) will give the right energies, even though it is based on questionable boundary conditions. One difference between (6.35) and (6.6) is that the solution

to (6.6) includes the entire  $\phi_d$ -dependence, and  $\chi_k(\phi_d)$  only contains some of it. There is an additional exponential factor, as seen in (6.34). With this in mind, we cannot trust the actual wave functions that emerge from (6.6), but the energies will almost be correct.

There is one more thing to remember when solving the equation (6.30), and that is the extra constraint mentioned in the previous section. After solving the equation, one has to discard the solutions that do not satisfy the original symmetry, that is  $2\pi$ -periodicity in  $\phi_1$  and  $\phi_2$ . Now, the states are grouped in bunches of almost degenerate states because of the four wells of the torsional potential. Since the energies found in sections 6.1 and 6.2 are almost identical, there are apparently states in each degenerate bunch of  $(\phi_d, \Phi)$ -solutions that satisfy the original symmetry. The number of states in these bunches is four for the  $(\phi_1, \phi_2)$ -solutions, but for the higher excited bunches of  $(\phi_d, \Phi)$ -solutions it is eight. This means that only half of these states fulfil the  $2\pi$ -periodicity in  $\phi_1$  and  $\phi_2$ .

The approach used in this section actually resembles the Born-Oppenheimer (BO) approximation, as described in section 2.3. First of all, this is a separation of a slowly varying degree of freedom  $\Phi$  from the more rapidly varying  $\phi_d$ , which is also the idea in the BO approximation. In the derivation given here, the separation between  $\Phi$  and  $\phi_d$  is exact, i.e. (6.32) and (6.35) follow directly from (6.2) without any additional approximations. The only approximation made in this section is to neglect some terms in (6.35) to obtain an equation that can be compared to (6.6). In the BO approximation, some terms in the Hamiltonian had to be neglected to separate the degrees of freedom (see (2.7) and the text just below this equation). Otherwise, the two separation techniques are similar.

The separation of  $\phi_d$  and  $\Phi$  that was described in this section only worked because the torsional potential is independent of  $\Phi$ . This is not the case for the kick potential, so one might not be able to find eigenstates for a Hamiltonian including this potential using  $\phi_d$  and  $\Phi$ .

The way the results of this section will be used in the chapters to come, is mainly as a proof that the eigenstates of (6.1) can be labelled as  $|n, m\rangle$  where  $n$  is an index referring to  $\phi_d$  and  $m$  is referring to  $\Phi$ . The wave function corresponding to this state is

$$\langle \phi_d, \Phi | n, m \rangle = e^{im\Phi} \psi_{m,n}(\phi_d), \quad (6.36)$$

in accordance with (6.32). This eases the interpretation of the results.

## 6.5 Summary

In this chapter, we have found eigenstates and eigenvalues of the Hamiltonian without the kick pulse, (6.1) or (6.2). It has been done in  $(\phi_d, \Phi)$ -coordinates, which was quite simple once we had the solutions from last chapter, and in  $(\phi_1, \phi_2)$ -coordinates. The coordinates  $(\phi_d, \phi_s)$  were also described as an alternate possibility, but not used to find any solutions. For  $(\phi_1, \phi_2)$ , we had to solve a 2D quantum mechanical problem numerically, which means diagonalizing a very large matrix. The results in the two cases  $(\phi_1, \phi_2)$  and  $(\phi_d, \Phi)$  are very similar, even though the  $(\phi_d, \Phi)$ -solutions are based on an additional approximation. In section 6.4, it was shown analytically that this approximation does not alter the energies very much. It was also shown that a separation of  $\phi_d$  and  $\Phi$  could be done without any approximations, so it makes sense to interpret the results in terms of  $\phi_d$  and  $\Phi$ .

The best way to solve the problem is to use  $(\phi_1, \phi_2)$ -coordinates, since this approach finds exact eigenstates of (6.1). The  $(\phi_d, \Phi)$ -coordinates are better for interpretation of the results, so in the next chapter, we will use those coordinates as well when it comes to discussing results.

## Chapter 7

# 2D quantum mechanical models: Inclusion of the kick pulse

In the previous chapter, we found eigenstates and eigenvalues of the Hamiltonian without the kick pulse (6.1) in different 2D quantum mechanical models. Now, we will use these results to solve the time dependent Schrödinger equation including the kick pulse,

$$i \frac{\partial}{\partial t} \psi = H_{\text{kick}} \psi, \quad (7.1)$$

where the Hamiltonian in  $(\phi_1, \phi_2)$ -coordinates is

$$H_{\text{kick}} = -\frac{1}{2I_1} \frac{\partial^2}{\partial \phi_1^2} - \frac{1}{2I_2} \frac{\partial^2}{\partial \phi_2^2} + V_{\text{tor}}(\phi_1 - \phi_2) + V_{\text{kick}}(\phi_1, \phi_2, t). \quad (7.2)$$

The torsional potential is given by (3.1) and (3.2), the kick potential can be seen in (4.30) and the polarizability in this equation is found in (4.28) and (4.29).

The coordinates  $(\phi_1, \phi_2)$  will be used, since an exact solution of (6.1) was possible in these coordinates. The initial state of the molecular gas is a mixed state given by the density operator

$$\rho(t_0) = \sum_n P_n |\psi_n\rangle \langle \psi_n|, \quad (7.3)$$

where  $|\psi_n\rangle$  are eigenstates of (6.1), the Hamiltonian without the kick pulse. As in section 5.6, we will not include temperature effects and only study the four ground states. In addition to that, we will only study *one* of the in  $\phi_d$  localized states  $|L_{0,0}^{(i)}\rangle$ , see figure 6.3. This is discussed in further detail in sections 5.6 and 8.6.

As mentioned in chapter 3, the experiment in [3] uses an initial state that is 3D-aligned. The state  $|L_{0,0}^{(i)}\rangle$  is not 3D-aligned, so for comparing with this experiment we need a different initial state. The idea is to multiply  $|L_{0,0}^{(i)}\rangle$  by a Gaussian in  $\Phi$ , such that the state becomes confined in both  $\phi_1$  and  $\phi_2$ . The only problem with this approach is that such an initial state is not an eigenstate of (6.1), which we have seen in section 3.2 that it should be. We will simply ignore that, and use a 3D-aligned initial state anyway when comparing to the experiment in [3].

In the following section finding a solution of (7.1) will be attempted in a basis, and we will see that the problem can be formulated as solving a system of ordinary differential equations. The conclusion is that too many basis states are required. In section 7.2, another method will

be described, and this method turns out to work well. It is based on representing the wave function on a numerical grid and propagating forward in time in small steps. Section 7.3 shows a trick that is used when representing the states found in section 6.2 on the grid, and section 7.5 discusses whether one could have solved (7.1) by using the coordinates  $(\phi_d, \Phi)$  instead.

## 7.1 Solving in a basis

Equation (7.1) for the Hamiltonian (7.2) can be transformed into a set of differential equations in a way very similar to (5.27). This is done by using a basis of eigenstates  $|\psi_n\rangle$  of (6.1), the Hamiltonian without the kick pulse. As initial state we use a state localized in  $\phi_d$ ,  $|L_{0,0}^{(i)}\rangle$ . Since the localized states  $|L_{j,m}^{(i)}\rangle$  are almost eigenstates of (6.1), the initial state can, for now, be treated as an eigenstate of the Hamiltonian without the kick pulse. When a molecule in such an eigenstate is hit by the kick pulse, it will immediately be kicked into a superposition of eigenstates,

$$|\psi_n\rangle \rightarrow \sum_{n'} c_{n',n}(t) e^{-iE_{n'}(t-t_0)} |\psi_{n'}\rangle. \quad (7.4)$$

Equation (7.4) can be inserted into (7.1), and, by projecting onto another eigenstate  $|\psi_{n''}\rangle$  of (6.1), we find

$$i \frac{\partial}{\partial t} c_{n'',n}(t) = \sum_{n'} \langle \psi_{n''} | V_{\text{kick}}(\phi_1, \phi_2, t) | \psi_{n'} \rangle c_{n',n}(t) e^{i(E_{n''} - E_{n'})(t-t_0)}, \quad (7.5)$$

which is very similar to (5.31). It is (7.5) that we want to solve. Unlike the semiclassical model of chapter 5, there are not two equations; only one. Since both angles are treated quantum mechanically, there is no classical equation here.

The equation to solve is a large system of ordinary differential equations. This can be solved in a basis, meaning that the kick pulse is described as a matrix in the basis of eigenstates  $|\psi_n\rangle$  of (6.1), as written in (7.5). As in section 5.6, the problem can be solved using standard methods of propagating in small steps. There is a problem with this approach, though. We simply need way too many basis states to get a proper convergence of the results. In section 6.2 we needed 10,000 basis states to get a convergence of a few eigenstates of (6.1), but to be able to use the eigenstates as a basis, the convergence of many more states is needed. The basis will therefore become immensely large, which means that the size of the matrix in (7.5) becomes a problem.

If one really wants to solve this problem in a basis there are a few other ways to go. One is to use the coordinates  $(\phi_d, \phi_s)$  that were introduced in section 6.3. This might lead to a smaller basis, but it has not been investigated in detail for this thesis. It might also be possible to use the coordinates  $(\phi_d, \Phi)$  with the correct boundary conditions, as described in section 6.4. This approach will be discussed in section 7.5

## 7.2 Split-step method

The method described in the previous section seemed to be too hard to implement, but there are other ways of solving the time dependent Schrödinger equation. One of them involves discretizing space into a grid and doing the numerical calculations on this grid. The solution will be found by taking small steps forward in time, starting from the initial time  $t_0$ . The Hamiltonian is split into two parts, the kinetic and the potential part, and to account for them both in a clever way, we use Fourier transforms. This method is a split-step method, called so

because the propagation is done in small steps, and the operator  $H$  is split into its kinetic and potential parts [43].

The first thing to do is to discretize space. Quantum mechanical states belong to the Hilbert space, which has an infinite number of dimensions, but when we use numerical computations, we have to do a truncation. This means only looking at a finite number of dimensions, for example by choosing the basis to consist of a finite number of elements. The same idea lies behind discretization of space. We choose to represent  $\phi_1$  by a vector with  $N_d$  entries from  $-\pi$  to  $\pi$ , where the  $i$ th entry is  $\phi_{1,i} = (i-1)d\phi_1 - \pi$ . Here,  $d\phi_1$  is the difference in the  $\phi_1$ -value between two neighbouring vector entries. The coordinate  $\phi_2$  is represented in a completely analogous way. The wave function  $\Psi(\phi_1, \phi_2)$  depends on both coordinates, so it has to be represented by an  $N_d \times N_d$  matrix whose  $(i, j)$ th entry is  $\Psi(\phi_{1,i}, \phi_{2,j})$ . The wave function has now been represented on a 2D grid.

Now, we want to be able to propagate the wave function  $\Psi$  in time. This means that we want  $\Psi(t_0)$  to evolve in time to  $\Psi(t)$ :

$$\Psi(t) = U(t, t_0)\Psi(t_0), \quad (7.6)$$

where  $U(t, t_0)$  is the time evolution operator that evolves the wave function from time  $t_0$  to time  $t$ . The time evolution operator is given by [31]

$$U(t, t_0) = e^{-iH(t-t_0)}. \quad (7.7)$$

Equation (7.6) shows an operator acting on a state, and the usual way to calculate the effect of the operator in quantum mechanics is to represent the state  $\Psi(t_0)$  by a vector and the operator  $U(t, t_0)$  by a matrix. At this point, the state is represented by a  $N_d \times N_d$  matrix, and such a representation makes it simple to visualize the state as function of  $\phi_1$  and  $\phi_2$ . To represent this state by a vector, the vector must have length  $N_d^2$ , where each entry corresponds to a point in  $(\phi_1, \phi_2)$ -space. Now, we need to find a way to represent (7.7) as a  $N_d^2 \times N_d^2$  matrix, and then the calculation can be done numerically.

A frequently used approximation is that this operator is constant during small time steps  $\Delta t$ , where  $M_t \Delta t + t_0 = t$ . The operator (7.7) can now be separated into  $M_t$  factors,

$$U(t, 0) = \underbrace{e^{-iH\Delta t} e^{-iH\Delta t} \dots e^{-iH\Delta t}}_{M_t \text{ times}}. \quad (7.8)$$

What we would like to do now, is to act  $M_t$  times with the operator  $e^{-iH\Delta t}$  on the initial state  $\Psi(t_0)$ . We must find the  $N_d^2 \times N_d^2$  matrix that corresponds to  $e^{-iH\Delta t}$  and apply it  $M_t$  times to  $\Psi(t_0)$ . The Hamiltonian (7.2) consists of two types of terms, kinetic and potential terms. The potential terms  $V_{\text{tor}}$  and  $V_{\text{kick}}$  can be represented on the 2D grid by  $N_d \times N_d$  matrices, just like  $\Psi$ , so they can also be thought of as vectors of length  $N_d^2$ . Now, we must remember that the potentials are operators, and when states are represented by vectors, operators are represented as matrices. Since  $V_{\text{tor}}$  and  $V_{\text{kick}}$  have an associated value at each of the  $N_d^2$  points in the grid, they are *local* operators represented by diagonal matrices. Therefore,  $e^{-i(V_{\text{tor}}+V_{\text{kick}})\Delta t}$  can also be represented by a diagonal  $N_d^2 \times N_d^2$  matrix. When the matrix is diagonal, the multiplication in (7.6) is simple. For the kinetic terms  $T$ , it is not so simple, so we would like to separate the kinetic parts  $T$  from the potential parts  $V$  of  $e^{-iH\Delta t}$ . It can be done by invoking the relation

$$e^{-iH\Delta t} = e^{-iV\Delta t/2} e^{-iT\Delta t} e^{-iV\Delta t/2} + O(\Delta t^3), \quad (7.9)$$

where  $O(\Delta t^3)$  is a correction term. It occurs because  $T$  and  $V$  do not commute. That the correction term becomes third order in  $\Delta t$  can be seen by comparing the Taylor expansions of

the left and right hand side of (7.9) (see [44]). By making  $\Delta t$  very small, it can become a really good approximation to neglect the correction term.

We already know how to handle the potential part of (7.9). To deal with the kinetic part, we use the Fourier transform. A Fourier transform is an expansion of a function onto a set of waves,  $e^{ik\phi}$ , where  $k$  is the wavenumber. A Fourier transformed function can be represented on a Fourier grid, where the numbers at the grid points correspond to wavenumbers,  $k_1$  and  $k_2$  for  $\phi_1$  and  $\phi_2$  respectively. Each Fourier component  $e^{ik_1\phi_1}e^{ik_2\phi_2}$  is an eigenfunction of  $T$ ,

$$Te^{ik_1\phi_1}e^{ik_2\phi_2} = \left( -\frac{1}{2I_1} \frac{\partial^2}{\partial \phi_1^2} - \frac{1}{2I_2} \frac{\partial^2}{\partial \phi_2^2} \right) e^{ik_1\phi_1}e^{ik_2\phi_2} = \left( \frac{k_1^2}{2I_1} + \frac{k_2^2}{2I_2} \right) e^{ik_1\phi_1}e^{ik_2\phi_2}, \quad (7.10)$$

which means that  $T$  is a diagonal  $N_d^2 \times N_d^2$  matrix in Fourier space. The diagonal elements of  $T$  are  $k_1^2/2I_1 + k_2^2/2I_2$ .

Now we have to construct a Fourier grid that corresponds to the real space grid. There will be two 1D grids, corresponding to  $\phi_1$  and  $\phi_2$  respectively, and they can be combined to give a 2D grid, which can also be interpreted as a vector of size  $N_d^2$ . The distance between the two end points of the  $\phi_1$ -grid is  $2\pi$ , and the distance between neighbouring points is  $d\phi_1$ . We have periodic boundary conditions, so the largest wavelength the grid allows is  $2\pi$ . Then the smallest allowed wavenumber is

$$k_{\min} = \frac{2\pi}{N_d d\phi_1} = \frac{2\pi}{2\pi} = 1. \quad (7.11)$$

This means that the numbers  $k_1$  of the  $\phi_1$  Fourier grid have to be integers. The grid must be symmetric about 0, because both positive and negative values of  $k_1$  and  $k_2$  are allowed. The 1D grid for  $\phi_2$  is the same, and when they are combined we obtain an  $N_d \times N_d$  2D grid.

To shift between the real space grid and the Fourier grid, we use Fourier transforms. One multiplication by  $e^{-iH\Delta t}$  is done in the following way:

1. Multiply the original state by  $e^{-iV\Delta t/2}$
2. Fourier transform
3. Multiply by  $e^{-iT\Delta t}$
4. Inverse Fourier transform
5. Multiply by  $e^{-iV\Delta t/2}$

Then, the state has been propagated  $\Delta t$  forward in time. By repeating these steps  $M_t$  times, one can propagate the initial state from  $t_0$  to the final time  $t$ .

Since we are dealing with representations on a grid, we must of course use the discrete Fourier transform (DFT), for example the fast Fourier transform (FFT). It can be done efficiently in MATLAB by using the built in functions `FFT` or `FFT2`. The latter is a 2D version of the former. The speed of the calculation will be improved if we choose  $N_d^2$  to be a power of two (see [45] p. 267-270).

This method turns out to work quite well; the only disadvantage is that it does not give the relation to the eigenstates of the Hamiltonian without the kick pulse. This disadvantage is not too significant in this thesis, since the basis states were merely a step on the way, not a goal in themselves.



When doing the propagation, one has to pick the size of the grid and the time steps such that the calculations can be done as quickly as possible, but the results still have to be correct. An acceptable grid is one that provides results that are the same as the results of a much larger grid, but it still has to be as small as possible. The time steps have to be as large as possible for swifter calculations but must still yield the correct results.

The results will be discussed in chapter 8.

### 7.3 Propagation in "imaginary time"

The split-step method described in the previous section works, but there is one final finesse to be discussed. As mentioned in the beginning of this chapter, we want to start out in an eigenstate of (6.1). When we find an eigenstate using the method of chapter 6 it is the coefficients in a given basis that are found. To use this for propagating on a grid, we must represent that state on the grid, and doing so means that it is no longer an exact eigenstate. We can correct this by using a technique called propagation in "imaginary time".

A wave function  $\Psi$  propagating in time can be expanded in energy eigenstates  $\psi_n e^{-iE_n t}$  of the Hamiltonian of the system,

$$\Psi(t) = \sum_n c_n \psi_n e^{-iE_n t}. \quad (7.12)$$

Now the variable  $\tau = it$ , which can be interpreted as a sort of "imaginary time" is introduced. This yields

$$\Psi(\tau) = \sum_n c_n \psi_n e^{-E_n \tau}, \quad (7.13)$$

so if  $\tau$  is real valued, the complex exponentials of (7.12) will be turned into exponentially decreasing functions for  $E_n > 0$ . We will assume that  $\tau$  is real valued. If  $\tau$  increases, the terms with the largest energies will be suppressed, and if  $\tau$  becomes large enough only the ground state term in (7.13) will contribute to  $\Psi$ . The contribution of the ground state term will also have become very small, but this issue can be avoided by normalizing  $\Psi$  after each time step. In conclusion the ground state of a system can be found by starting with a random wave function of the form (7.12) where the ground state term is not exactly zero and propagating in imaginary time.

The propagation will be done on a grid as described in section 7.2, with the time  $t$  is replaced by the imaginary time  $\tau$ .

This technique is used to find the initial state where the kick pulse has not been applied yet, so the energy eigenstates  $\psi_n$  are the states found in chapter 6. There are four almost degenerate ground states, so one should take care when propagating this system in imaginary time. The state that is propagated in imaginary time in this thesis is almost an in  $\phi_d$  localized state,  $|L_{0,0}^{(i)}\rangle$ , and the goal is to find the exact localized state. Since the state is almost an eigenstate already, the other three lowest states will not have much of an influence, so the state  $|L_{0,0}^{(i)}\rangle$  will be found.

### 7.4 Comparing to experiments

When the wave function has been propagated on a grid, there is still something left to do before the results can be compared to experiments. In section 3.3, it was seen that the experimental results are ion images, and they can be translated to plots of the probability density as a

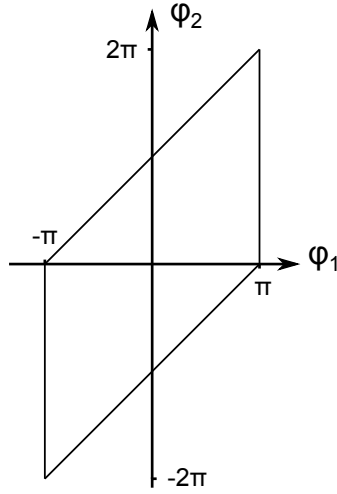


Figure 7.1: This figure shows the 2D grid after it has been reshaped. The upper sloping line corresponds to  $\phi_d = -\pi$  and the lower to  $\phi_d = \pi$ , which means that the state seen in figure 6.3 becomes one continuous line when transformed to this new grid. It is thus easier to calculate the expectation value of  $\phi_d$ .

function of  $\phi_1$  or  $\phi_2$  like figure 3.4 (b). The norm squared of the theoretical final wave function is the probability density as a function of both  $\phi_1$  and  $\phi_2$ , so density plots that can be directly compared to the experiments can be obtained by integrating the wave function over either  $\phi_1$  or  $\phi_2$ .

To find the expectation value of  $\phi_d$  as a function of time, one has to perform an integral over both  $\phi_1$  and  $\phi_2$ ,

$$\langle \phi_d \rangle = \int d\phi_1 \int d\phi_2 \psi^*(\phi_1, \phi_2, t) \phi_d \psi(\phi_1, \phi_2, t), \quad (7.14)$$

since the initial state corresponds to a pure state. The only problem is that  $\phi_d$  runs from  $-2\pi$  to  $2\pi$  in the grid that is used, so an in  $\phi_d$  localized state will have peaks at two different values of  $\phi_d$ , see figure 6.3. These two peaks correspond to the same value of  $\phi_d$ , but that is not seen in (7.14). Using this formula will therefore give an expectation value that is somewhere between the two peaks in  $\phi_d$ . To get the correct result, we have to translate the upper of the two lines in figure 6.3 so that it has the correct value of  $\phi_d$ , which is done by decreasing  $\phi_2$  by  $2\pi$ . To do that, a reshaping of the grid is needed. Every grid point that lies above the line  $\phi_2 = \phi_1 + \pi$  will have its value of  $\phi_2$  decreased by  $2\pi$ . At the same time all points below the line  $\phi_2 = \phi_1 - \pi$  get their value of  $\phi_2$  increased by  $2\pi$ . This new grid is seen in the  $(\phi_1, \phi_2)$ -plane in figure 7.1. The correct expectation value can now be found using (7.14), if the integration over  $\phi_2$  is done first. The technique only works because the wave function is zero around  $\phi_d = \pm\pi$ , and the reason for these zero points is that the torsional potential peaks at  $\phi_d = \pm\pi$ .

## 7.5 Discussion of the $(\phi_d, \Phi)$ -coordinates

In section 6.4, it was shown analytically that  $\phi_d$  and  $\Phi$  could be separated. It was also shown that the approach of chapter 5 would give the correct eigenvalues of (6.2), but not the correct

eigenstates. The next question to ask is whether it is possible to find exact solutions to (7.1) in the  $(\phi_d, \Phi)$ -coordinates. When the  $2\pi$ -periodicity of  $\phi_d$  and  $\Phi$  is used, as in chapter 5, the eigenstates of (6.2) are not exact, so solving the equation a basis (section 7.1) of these eigenstates will not give the desired result. If the split-step method (section 7.2) is tried, the solution will not be exact either, because the grid will have a wrong periodicity. This means that the results from the 1D model in chapter 5 and the  $(\phi_d, \Phi)$ -model of section 6.1 can not be expected to be exact solutions of (7.1), as has already been discussed.

To get the exact solution, one must use the periodicities described in section 6.4, i.e. a  $(M + N)2\pi$ -periodicity of  $\phi_d$  and  $2\pi$ -periodicity of  $\Phi$ . Since  $M$  and  $N$  are rather large, such an approach is not desirable when solving on a grid, because it will lead to an immensely large grid. One final possible approach for finding exact solutions of (7.1) in the  $(\phi_d, \Phi)$ -coordinates, is to use basis functions that possess the correct periodicities in  $\phi_d$  and  $\Phi$ . It might work, but this approach will not be studied further in this thesis. Instead, the coordinates  $(\phi_1, \phi_2)$  will be used, as has already been done throughout this chapter. After the calculation, the results can be expressed in  $(\phi_d, \Phi)$ -coordinates, which is as good as solving the problem in  $(\phi_d, \Phi)$ -coordinates in the first place.

## 7.6 Summary

This chapter has shown how the propagation of the molecular state in the kick pulse potential can be done. The method used is propagation on a grid, because the problem is too large to be solved in a basis. The calculations are done in the  $(\phi_1, \phi_2)$ -coordinates.



## Chapter 8

# Results of a 2D quantum mechanical model

The results of the 2D quantum model in  $(\phi_1, \phi_2)$ -coordinates described in chapters 6 and 7 are discussed in this chapter. Since the  $(\phi_1, \phi_2)$ -coordinates are used, equation (7.1) is solved exactly. The approximations used are all listed in section 3.2. This model, using the coordinates  $(\phi_1, \phi_2)$ , will from now on be referred to as the 2D model.

The discussion of the results will mainly be done in terms of  $\phi_d$  and  $\Phi$ , since these coordinates simplify the discussion of torsional and rotational motion. The results will be compared to the experimental results from [1, 2, 3] presented in section 3.3 and the semiclassical results of section 5.7.

The first four sections will describe the oscillations in  $\langle \phi_d \rangle$ , i.e. the torsional motion of the molecules. In section 8.5, the delocalization at large times is discussed, and finally the validity of the initial state chosen in the calculations is investigated in section 8.6.

All calculations have been done using a 2D grid of  $4096 \times 4096$  points. The difference between two adjacent grid point in such a grid is

$$d\phi_1 = d\phi_2 = \frac{2\pi}{4096} = 0.0015 \text{ rad} = 0.088^\circ, \quad (8.1)$$

which corresponds to the precision of the calculations. This is enough to study oscillations in  $\langle \phi_d \rangle$  with an amplitude of about  $0.6^\circ$ , as was found experimentally (see section 3.3). Since one complex number (double precision) takes up 16 byte of memory, a matrix defined on this grid uses more than 250 MB of memory, which is little enough to be handled by any computer. The problem is that this matrix needs to be updated at every time step, and that takes a lot of time for such a large matrix.

The size of the time steps is chosen to be  $\Delta t = \tau/50$ , where  $\tau$  is the pulse length (FWHM). The reason why the step size depends on  $\tau$  is that the short, but intense pulse from the experiments in [3] makes the angles  $\phi_1$  and  $\phi_2$  change faster than the pulse from [1, 2]. A faster change in the variables means that a smaller time step is needed. Some calculations have been made with much larger time steps, and since these calculations gave the same results as with a time step of  $\tau/50$ , it is safe to assume that convergence will be achieved for  $\Delta t = \tau/50$ .

### 8.1 Oscillations in $\langle \phi_d \rangle$

Oscillations in the dihedral angle as a function of time were found experimentally and using the semiclassical model (see figures 3.4 and 5.4). They are very important, since they show that torsional motion is actually initiated by ultrashort laser pulses. Therefore, we would like to find such oscillations when using a 2D quantum mechanical model, and we actually do,

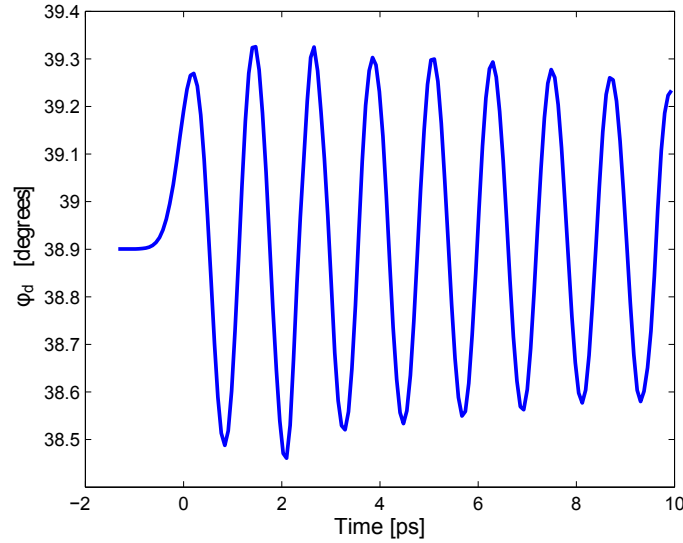


Figure 8.1: Oscillations in  $\langle \phi_d \rangle$  as a function of time, as found in the 2D model. Both kick pulse parameters and the initial state are chosen to fit the experiment in [1, 2], so the initial state is a localized state in  $\phi_d$ , but delocalized in  $\Phi$ . The program took some hours to run.

as is seen in figure 8.1. The calculation behind this figure uses parameters that are chosen to fit the experiment in [1, 2]. The kick pulse has a length of 0.7 ps and a peak intensity of  $5 \times 10^{12} \text{ W cm}^{-2}$  and is centered around  $t = 0$ , as it will be in all calculations to come. Furthermore, the initial state is localized in  $\phi_d$ , but delocalized in  $\Phi$ . Such an initial state could not be chosen in the semiclassical model, since  $\Phi$  was treated classically, so one would expect the oscillations found here to be closer to the experimental results than the oscillations found in chapter 5. The oscillations in figure 8.1 have an amplitude of  $0.4^\circ$ , and the corresponding experiment in [1, 2] reveals an amplitude of about  $0.6^\circ$ . Thus, the result of the 2D model is significantly closer to the experiment than the amplitude of  $3.1^\circ$  found using the semiclassical model (see figure 5.4). This was expected, since the 2D model allows the choice of an initial state that fits the experiment.

Even in the 2D model, there is a difference between the theoretical and experimental result. This is most probably caused by the rather uncertain experimental result. It is found by making a fit to few data points, and the quality of the fit is not too impressive, as is seen in figure 3.4 (c). Therefore, we only expect a qualitative agreement with this experimental result. If the experimental result had been more precise, we would actually expect to see an amplitude that is a bit lower than what is found theoretically. This is because the pulse has a certain width in space, and only the molecules that are spatially in the middle of the laser beam are exposed to the peak intensity. Other molecules will experience a lower intensity. To get a more precise theoretical result, one would have to do focal volume averaging. Another problem is that the model assumes perfectly aligned molecules, which is only an approximation, and finally the potential of the alignment pulse is ignored. All these factors could contribute to a different amplitude in theory than in the experiments. The period of the oscillation in figure 8.1 is 1.22 ps, which is close to the experimental estimate of  $\sim 1$  ps. We also notice from figure 8.1

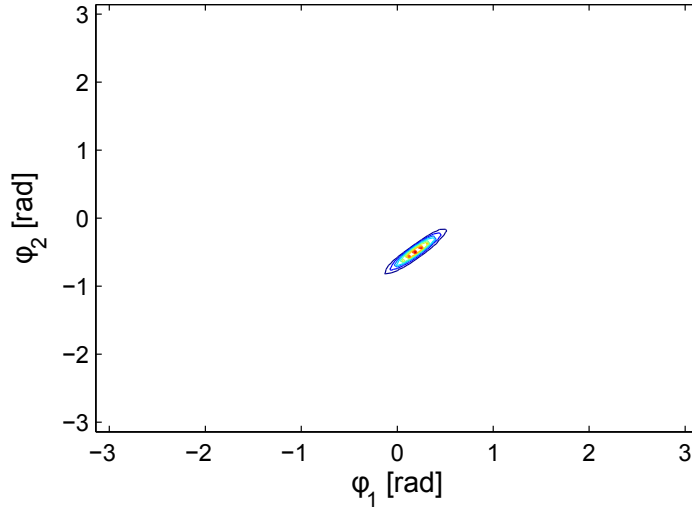


Figure 8.2: The norm squared of a state that is initially localized in both  $\Phi$  and  $\phi_d$ , here shown in the  $(\phi_1, \phi_2)$ -plane. Blue curves correspond to low probability density and red curves to a high probability density. In this figure the state is localized along the SMPA of the molecule, and such a state is used as initial state when comparing the theory to the experiments of [3]. The state is obtained by multiplying the localized state  $|L_{0,0}^{(1)}\rangle$  seen in figure 6.3 by a Gaussian in  $\Phi$ .

that the amplitude is damped over time.

Results of the 2D quantum model in  $(\phi_1, \phi_2)$ -coordinates can also be compared to the size of the oscillations seen in the experiment in [3]. For this experiment, the initial state has to be a localized in both  $\phi_d$  and  $\Phi$ , the length of the kick pulse has to be 0.2 ps, and the peak intensity  $2 \times 10^{13} \text{ W cm}^{-2}$ . We choose a state localized around  $(\phi_d, \Phi) = (39^\circ, 4.3^\circ)$ , which corresponds to aligning the SMPA with the polarization of the kick pulse. The initial state is found by multiplying a localized state in  $\phi_d$ , like the one seen in figure 6.3, by a Gaussian in  $\Phi$ . The result is an initial state that is confined to a peak instead of a line, see figure 8.2. Since the pulse length is shorter than in [1, 2], a different initial time is chosen, and that is  $t = -0.4$  ps. There is a free parameters to adjust, though, and that is the width of the peak in the  $\Phi$ -direction. For now, we set it to be  $0.5 \text{ rad} \approx 30^\circ$ , which is a bit wider than the width in  $\phi_d$  of the state in figure 6.3. The result is, as can be seen in figure 8.3, an amplitude of  $6.5^\circ$  and a period of 1.22 ps. The experimental value is  $3^\circ$ , as seen in figure 3.6, and the semiclassical model gave a result of  $6.8^\circ$  (figure 5.5). The first thing we note is that the semiclassical model and the 2D model now give approximately the same amplitude. This is because the initial states in the two calculations are similar, having a fixed value of both  $\phi_d$  and  $\Phi$ . The experimental value is lower, which is expected due to effects of the focal volume of the kick pulse, the imperfect alignment, and effects of the alignment pulse potential. Another possible reason for the deviations of the theoretical result from the experiment one is the use of a wrong torsional potential, as described in section 3.2. The torsional potential used here corresponds to the DFDBrBPh-molecule, but in this experiment, the molecule DFDBrCNBPh is used instead. For a better comparison between theory and experiment,  $0.9^\circ$  have been subtracted from  $\langle\phi_d\rangle$ . Finally,

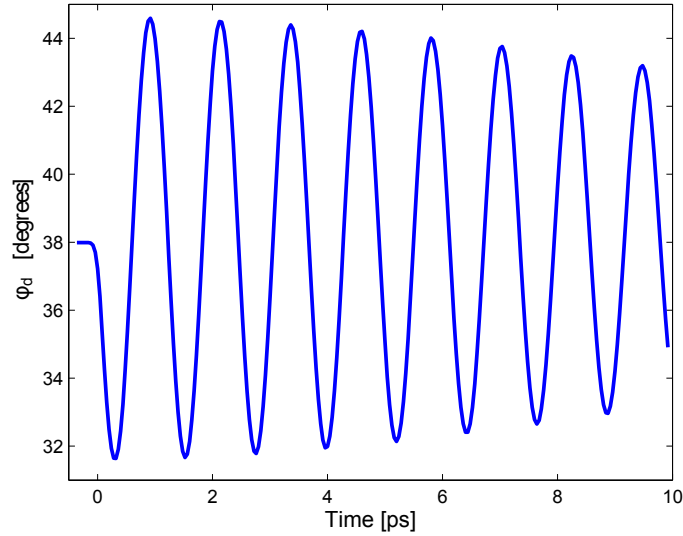


Figure 8.3: Oscillations in  $\langle \phi_d \rangle$  as a function of time for a simulation designed to resemble the experiment in [3]. The initial state is a localized state in both  $\phi_d$  and  $\Phi$ , and the parameters of the kick pulse are identical to the experiment in [3]. To account for the use of a torsional potential for the wrong molecule,  $0.9^\circ$  have been subtracted from  $\langle \phi_d \rangle$ . The program took some hours to run.

we remember that the state seen in 8.2 is not an eigenstate of the Hamiltonian without the kick pulse, (6.1), which the initial state should actually be. This might also cause a difference between theory and experiment.

It is striking that the amplitude of the oscillation has become so much larger by fixing the initial value of  $\Phi$ . This actually means that the control of the torsional motion has improved significantly. An understanding of this phenomenon relies on quantum interferences, and it will be discussed in section 8.3.

## 8.2 The period of the oscillations

The period is 1.22 ps in figures 8.1 and 8.3, and a similar value was also found in experiments and in the theory from chapter 5. In section 5.7, there is a discussion of this period, and it is argued that the period corresponds to the difference between the two lowest energies of the 1D Hamiltonian without the kick pulse, (5.14). We can actually understand why the 2D model should give the same result as the 1D model.

To derive the period of the oscillations in  $\langle \phi_d \rangle$  using the 2D model, we must remember that the initial state might not be an eigenstate of the Hamiltonian without the kick pulse, (6.1). If the initial state is not an eigenstate, it might actually change before the kick pulse starts playing a role. In the derivation to come, the eigenstates of (6.1) will be named  $|n, m\rangle$ , where the index  $n$  refers to  $\phi_d$ , and the index  $m$  refers to  $\Phi$ . This is in accordance with the exact decoupling of  $\Phi$  and  $\phi_d$  made in section 6.4. The kick pulse interacts with the molecule at  $t = t_0$ .

Since the initial state is not an eigenstate of (6.1), it is a superposition of eigenstates,



$$|\psi(t < t_0)\rangle = \sum_{n,m} c_{n,m}(t) |n, m\rangle. \quad (8.2)$$

The coefficients  $c_{n,m}(t)$  are time-dependent, because each of the eigenstates in the sum will evolve as stationary states, meaning that they will obtain different phase factors as time goes by. This continues until  $t = t_0$ , when the short kick pulse hits and non-adiabatically excites the molecule. This gives rise to a superposition of even more different eigenstates,

$$|\psi(t_0)\rangle = \sum_{n,m} a_{n,m} |n, m\rangle, \quad (8.3)$$

where the coefficients  $a_{n,m}$  include both the excitation by the kick pulse and the relative phase changes of the different terms in (8.2), i.e. the  $c_{n,m}$  factors. Because the kick pulse is so short, it does nothing but excite the quantum state. The molecule has no time to propagate in the kick potential. Therefore, the state (8.3) evolves under influence of the Hamiltonian without the kick pulse from  $t_0$  and onward, so that each eigenstate in the sum experience different phase changes. So:

$$|\psi(t)\rangle = \sum_{n,m} a_{n,m} \cdot \sum_{n',m'} e^{-iE_{n',m'}(t-t_0)} |n', m'\rangle. \quad (8.4)$$

The energy  $E_{n,m}$  is, as described in section 6.2, approximately given as

$$E_{n,m} = 2E_{0,0}(n + 1/2) + \frac{1}{2I}m^2, \quad n = 0, 1, 2, \dots \quad m = 0, 1, 2, \dots \quad (8.5)$$

where  $E_{0,0}$  is the ground state energy. Just like in section 2.4, the expectation value of the dihedral angle becomes periodic in time:

$$\langle \phi_d \rangle = \langle \psi(t) | \phi_d | \psi(t) \rangle = |a_{n,m}|^2 \sum_{n'',m''} \sum_{n',m'} e^{i(E_{n'',m''} - E_{n',m'}) (t-t_0)} \langle n'', m'' | \phi_d | n', m' \rangle. \quad (8.6)$$

This is a sum of terms that are periodic with period

$$\frac{2\pi}{E_{n'',m''} - E_{n',m'}} \quad (8.7)$$

Now, it is time to use the exact shape of the states, (6.32). This equation can be used to show that the matrix elements  $\langle n'', m'' | \phi_d | n', m' \rangle$  do not couple states with  $m'' \neq m'$ , since

$$\begin{aligned} \langle n'', m'' | \phi_d | n', m' \rangle &= \int d\Phi e^{i(m' - m'')\Phi} \cdot \int d\phi_d \psi_{n''}^*(\phi_d) \phi_d \psi_{n'}(\phi_d) \\ &= 2\pi \delta_{m', m''} \int d\phi_d \psi_{n''}^*(\phi_d) \phi_d \psi_{n'}(\phi_d). \end{aligned} \quad (8.8)$$

The conclusion is that only energy differences corresponding to the same value of  $m$  will control the period of  $\langle \phi_d \rangle$ . These energy differences are the same that were used in section 5.7 to find the period in the semiclassical model, so the result will be the same as (5.37),

$$T_{\phi_d} = \frac{\pi}{E_{0,0}} = 1.20 \text{ ps}. \quad (8.9)$$

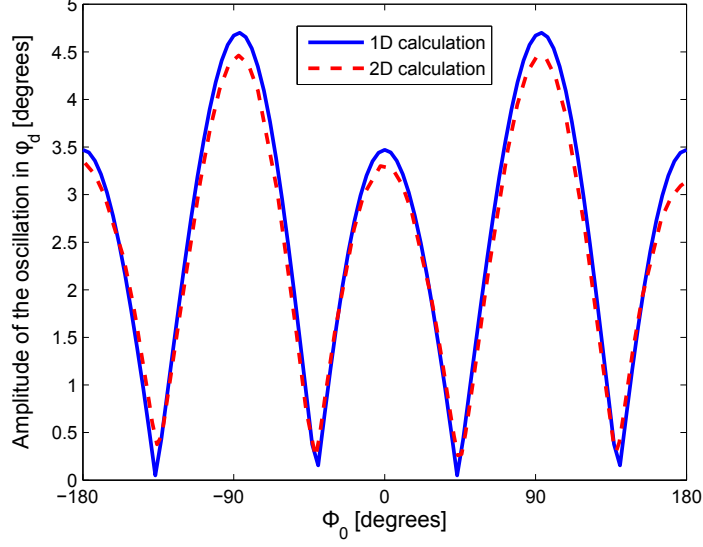


Figure 8.4: The amplitude of the oscillation in  $\langle \phi_d \rangle$  as a function of the initial angle,  $\Phi_0$ , for 3D-aligned initial states. The initial value of  $\langle \phi_d \rangle$  is  $39^\circ$ . Results are shown for both the semiclassical 1D model (blue) and the 2D quantum mechanical model (red). The calculations were done for a kick pulse with an intensity and length corresponding to the experiment in [1, 2]. The width of the Gaussian in the  $\Phi$ -direction is 0.5 rad.

This value comes from the energy difference between the two lowest eigenstates with different  $\phi_d$ -dependence. An excitation of the molecular wavefunction into different  $\Phi$ -states is not visible in period of the oscillations of  $\langle \phi_d \rangle$ .

The derivation above shows why the period found in both experiments and all theoretical calculations is about 1.2 ps.

### 8.3 Oscillation amplitude for different initial values of $\Phi$

In sections 3.3 and 5.7, we have seen that the amplitude of the oscillation in  $\langle \phi_d \rangle$  is larger when the initial value of  $\Phi$  is fixed to correspond to alignment of the SMPA with the polarization of the kick pulse, i.e. the  $X$ -axis, than when the initial state is delocalized in  $\Phi$ . What happens if we fix the initial value  $\Phi_0$  at some other value? This means rotating the initial state of the molecule, and we will see that it makes quite a difference. In figure 8.4, the amplitude of the oscillation as a function of  $\Phi$  is shown in the case where the initial value of  $\langle \phi_d \rangle$  is  $39^\circ$ . The calculations have been made in the semiclassical 1D model and in the 2D quantum mechanical model, both with a kick pulse corresponding to [1, 2]. Both show the same trend: The amplitude is very large around  $\Phi_0 = -180^\circ, -90^\circ, 0^\circ, 90^\circ, 180^\circ$ . In between these peaks, the amplitude of the oscillation drops to a much lower value.

The peaks at  $\Phi_0 = -90^\circ$  and  $\Phi_0 = 90^\circ$  can be understood qualitatively in the following way: The kick pulse potential (4.30) has a maximum value when the molecule is far away from the SMPA, which it is around  $\Phi = \pm 90^\circ$ . This is seen in figure 4.4 when remembering that  $\Phi = (1 - \eta)\phi_1 + \eta\phi_2$ . At these angles, the molecule will thus be hit harder by the kick pulse, so

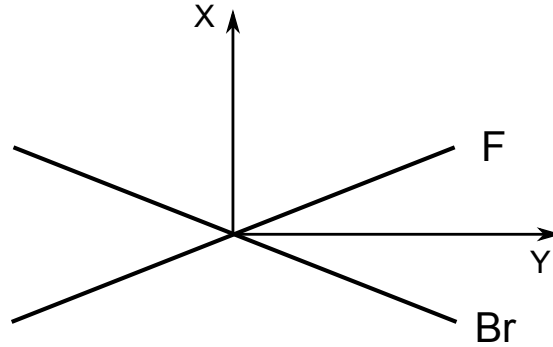


Figure 8.5: A biphenyl-like molecule is rotated so that it is just about perpendicular to the X-axis, which is the axis of polarization of the kick pulse. At this angle, the classical torque from the laser on the two rings is expected to be maximized, which means faster rotation of the two rings and also a larger amplitude of the oscillation in  $\phi_d$ .

the degree of induced rotational and torsional motion will be increased. Another way to think of these peaks is that the molecules are perpendicular to the polarization of the kick pulse at the position of the peaks, see figure 8.5. In a classical picture, the applied force from the laser pulse will result in a larger torque than if the molecule was parallel to the axis of polarization. This is because the torque is

$$\boldsymbol{\tau} = \boldsymbol{r} \times \boldsymbol{F}, \quad (8.10)$$

where  $\boldsymbol{F}$  is the force and  $\boldsymbol{r}$  is the point on the molecule where the force acts. If the molecule is perpendicular to the X-axis the force can hit the molecule at points where  $\boldsymbol{r}$  and  $\boldsymbol{F}$  are almost perpendicular, which will result in a faster rotation of the two rings. This will also lead to a larger amplitude of the oscillation in  $\langle \phi_d \rangle$  for  $\Phi = \pm 90^\circ$ , which explains two of the peaks seen in figure 8.4. The peaks at  $0^\circ$  and  $\pm 180^\circ$  in figure 8.4 cannot be understood in the same simple picture.

The experiment in [3] was carried out with the SMPA pre-aligned with the X-axis, which, for  $\phi_d = 39^\circ$ , corresponds to  $\Phi_0 = 4.3^\circ$ . This choice was made to increase the amplitude of the oscillations in  $\langle \phi_d \rangle$ , since the goal was an improved control of the dihedral angle. An increased amplitude is seen in both the 1D and 2D models when the SMPA is pre-aligned with the X-axis, so the approach seems sensible. As seen in figure 8.4, the oscillations in  $\langle \phi_d \rangle$  do however not have the maximum amplitude at  $\Phi_0 \approx 4.3^\circ$ . At  $\Phi \approx 90^\circ$ , the amplitude is larger, so by changing the localization of the initial state, one can improve the experimental amplitude of the oscillation in  $\langle \phi_d \rangle$  compared to what is found in [3]. This is important, because the main goal of the experiments [1, 2, 3] is to obtain control of the torsional motion. The way to change  $\Phi_0$  experimentally is to change the polarization of the elliptically polarized 3D alignment pulse such that the the minor axis of the ellipse is perpendicular to the polarization of the kick pulse.

The difference between the experimental results for a state localized in  $\phi_d$  and in  $\Phi$  (3D-aligned) and a state only localized in  $\phi_d$  (1D-aligned) can be understood in the following way: The 1D-aligned state is an eigenstate of (6.1). The state can be assumed to be one of the four lowest eigenstates, because the temperature in the experiment is so low, meaning that the state lies at the bottom of one of the potential wells in the torsional potential (see figure 3.2). The 3D-aligned state, on the other hand, is a linear combination of many different eigenstates. Therefore, it will not lie at the bottom of a potential well; higher lying states will

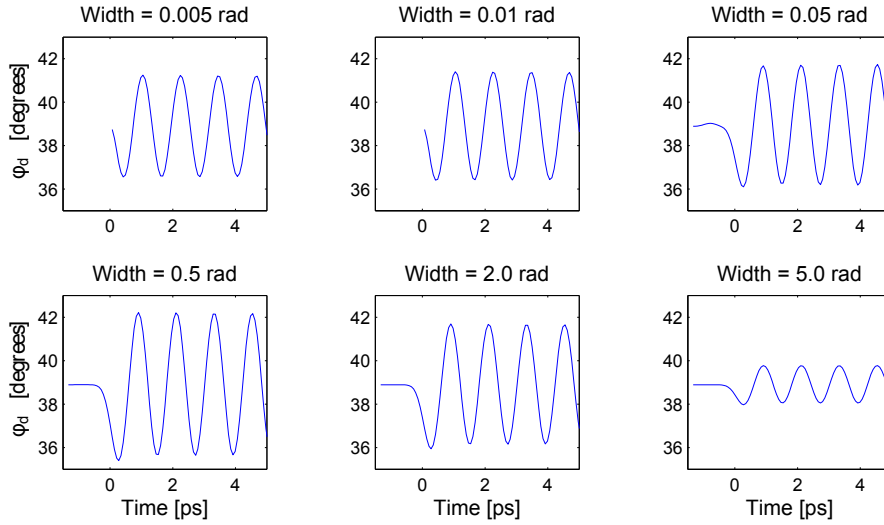


Figure 8.6: This figure shows the oscillation in  $\langle \phi_d \rangle$  for 3D-aligned initial states with different widths of the Gaussian in  $\Phi$ . In each case, the Gaussian is centered around  $\Phi = 4.3^\circ$ , and the width is stated above the graph. At both small and large widths, the amplitude is lower than in the intermediate region. The calculations were done with kick pulse parameters identical to the experiment in [1, 2], i.e. a pulse length of 0.7 ps and an intensity of  $5 \times 10^{12} \text{ W cm}^{-2}$ . For the widths 0.005 rad and 0.01 rad the initial time was chosen to be  $t = 0$ , while the rest of the graphs are calculated with the initial time  $-1.4$  ps. The kick pulse peaks at  $t = 0$ .

also be occupied. Since the torsional potential consists of potential wells in  $\phi_d$ , it makes sense that such a state can experience larger oscillations in  $\phi_d$ . The oscillations might also achieve a smaller amplitude if some of the occupied states interfere destructively. In other words, the peaks and dips in figure 8.4 can be interpreted as results of quantum interferences.

#### 8.4 Variation of the degree of initial 3D alignment

For calculations with a 3D aligned initial state, the initial  $\Phi$ -dependence was chosen to be Gaussian in section 8.1. The width of this Gaussian can be varied to understand what difference the  $\Phi$ -dependence of the initial state can make. It turns out that the amplitude of the oscillation after the kick pulse depends on the width of this Gaussian, as seen in figure 8.6. In the calculations behind the results shown here, the kick pulse parameters are identical to those in the experiment in [1, 2]. It is noted that the amplitude is largest for a width around  $0.5 \text{ rad} \approx 30^\circ$ . The maximum amplitude is  $3.3^\circ$ , and for a width of  $5.0 \text{ rad}$ , the amplitude has dropped to  $0.9^\circ$ . This drop is expected, since a very wide initial state is starting to resemble the delocalized state in  $\Phi$  (figure 6.3) used in the calculations behind figure 8.1, for which the amplitude is  $0.4^\circ$ . In the case of a very narrow Gaussian, the oscillations also become smaller, as seen to the top left in figure 8.6.

The graphs with the widths 0.005 rad and 0.01 rad have been made using an initial time of 0 ps, because the oscillations were more irregular if the simulations were started at  $-1.4$  ps like the rest. These irregularities are mainly caused by changes in the state before the kick

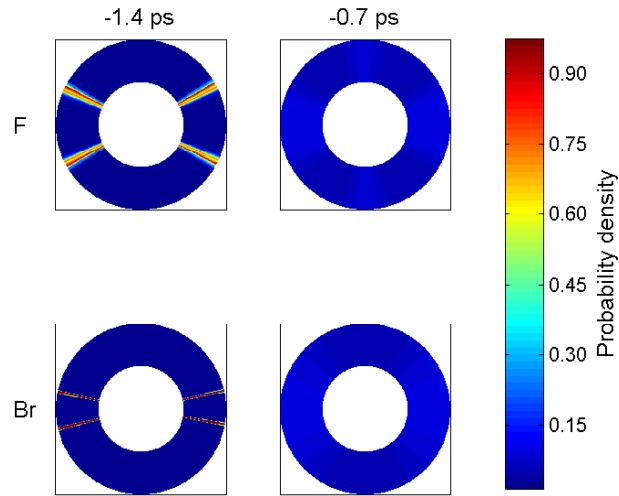


Figure 8.7: Plots of the calculated probability density for the two phenyl rings, marked by F and Br. Each plot depends on one parameter,  $\phi_2$  for F and  $\phi_1$  for Br, and since that parameter is an angle, the probability density has been plotted on a circle. The zero-point for  $\phi_1$  (Br) and  $\phi_2$  (F) is at the right hand side of each plot, and the angles increase in the counter-clockwise direction. Another way to say this is that the X-axis points to the right and the Y-axis points upwards (see figure 3.3). The initial state is 3D-aligned with a Gaussian width of 0.01 rad in the  $\Phi$ -direction, and the simulation is started at  $-1.4$  ps and the kick pulse has its maximum at  $t = 0$ . The probability densities are seen at two different times,  $t = -1.4$  ps and  $t = -0.7$  ps. At  $-0.7$  ps, which is before the kick pulse has a significant intensity, the state has already delocalized a lot. Consequently, the kick pulse does not hit the desired initial state, and it would be better to simply start the simulation at  $t = 0$ .

pulse hits. An initial state with a sharp peak will not be an eigenstate of (6.1), the Hamiltonian without the kick pulse. It will be a sum of many different eigenstates, which means that the state will change shape before the effects of the kick pulse set in. When that finally happens, the state will not contain a peak as narrow as before, and the oscillation will therefore be of smaller amplitude. In figure 8.7, the initial state for a Gaussian in  $\Phi$  with a width of 0.01 rad (at  $-1.4$  ps) can be seen along with the state at time  $-0.7$  ps, which is still 0.7 ps before the kick pulse reaches its maximum. The seemingly two-dimensional plots are actually just plots of one variable,  $\phi_1$  for the figures labelled Br and  $\phi_2$  for the figures labelled F. The angles are plotted on a circle, such that  $\phi_1 = 0$  or  $\phi_2 = 0$  corresponds to the horizontal direction to the right. This is done to ensure an easier comparison with figures 3.4, 3.5 and 3.7. As can be seen in figure 8.7, the state has dispersed considerably at  $-0.7$  ps, so it is an actual problem for the theoretical calculations with the widths of 0.005 rad and 0.01 rad.

When the initial state is not an eigenstate of (6.1), the expectation value of  $\phi_d$  might actually oscillate as a function of time even if there is no kick pulse. This is to some extent seen in the upper right panel of figure 8.6. The period of these oscillations will be the same as the period

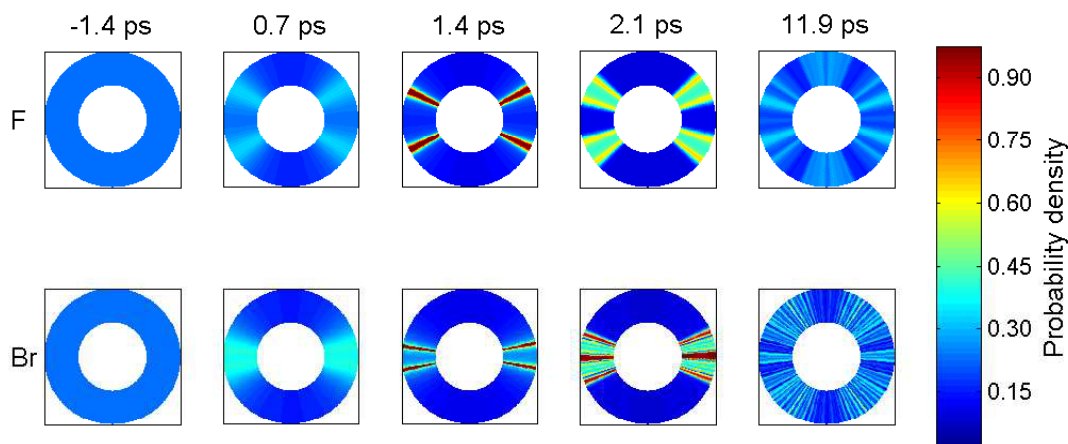


Figure 8.8: Probability density at different times for the fluorine ( $\phi_2$ ) and bromine ( $\phi_1$ ) rings. These are theoretically calculated and have been plotted on a circle for easier comparison with the experimental results of figure 3.4. The X-axis points to the right and the Y-axis points upwards, which means that the zero-point for the angles is to the right in each plot and the angles increase in the counter-clockwise direction. In order to get four peaks, the state had to be added to its own reflection in the horizontal axis.

calculated in section 8.2. Only the amplitude may vary, and we might expect it to be smaller than for a state that is hit by a kick pulse. The reason is that the initial state is only affected by the low-intensity alignment pulse and, thus, at a lower energy than a state that has been hit by the more intense kick pulse.

For the experiment in [3], the 3D alignment pulse is very weak compared to the kick pulse, and therefore, the Gaussian in  $\Phi$  used in the simulations that are compared to this experiment should not be too narrow. This is also seen in the ion image at  $-1.00$  ps in figure 3.5. The width chosen in the simulations in sections 8.1 and 8.3 is  $0.5$  rad  $\approx 30^\circ$ , which is maybe a bit more narrow than the ion image at  $-1.00$  ps in figure 3.5. This could be another reason for the too large oscillation seen in figure 8.3, but as is seen in figure 8.6, the change in amplitude is not substantial unless the peak in  $\Phi$  becomes very wide.

## 8.5 Four-dot structure and delocalization

In the experiments [1, 2, 3], the measurements of  $\langle \phi_d \rangle$  can only be done when the probability amplitude has a clear four-dot structure, as described in section 3.3, meaning that the molecules are 3D-aligned. In [1, 2], this four-dot structure is not visible before the kick pulse sets in, because the initial state is delocalized in  $\Phi$ . Then the kick pulse 3D-aligns the molecules for a few picoseconds, and after that the four-dot structure disappears again, as seen in figure 3.4. This is also found theoretically using the 2D quantum model, see figure 8.8. This figure shows the probability density of the quantum state at different times. The plots show a function of one variable, but plotted on a circle, where the X-axis points to the right and the Y-axis upwards. The plotting technique is the same as the one used in figure 8.7.

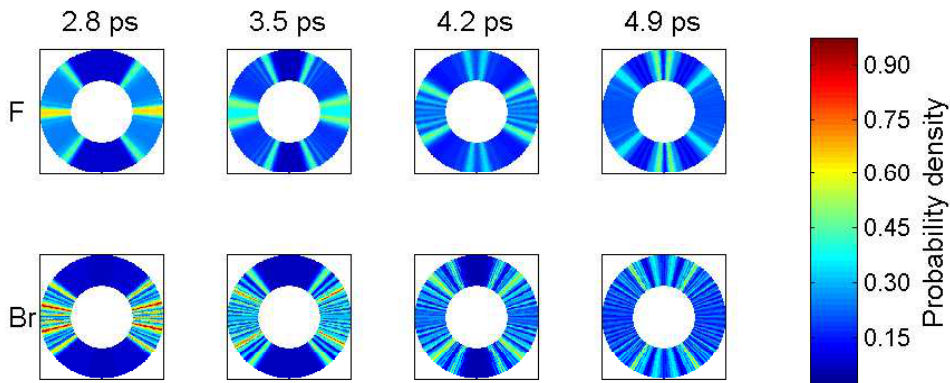


Figure 8.9: Probability densities at  $t > 3$  ps as functions of  $\phi_2$  (F) and  $\phi_1$  (Br) found by using the 2D model with kick pulse parameters identical to the ones used in the experiment in [1, 2]. The zero-point of the angles is to the right, and the angles increase in the counter-clockwise direction.

In the calculations behind figure 8.8, the initial state is delocalized in  $\Phi$  for consistency with the experiment in [1, 2] and the kick pulse parameters are also the same as in that experiment. We notice that the 3D alignment peaks around 1.5 ps, and at larger times, the state starts to delocalize, which is consistent with the ion images of figure 3.4 (a). One can also find the probability density from the semiclassical theory of chapter 5. As described in section 5.7, this has been done in [2], showing that the 3D alignment is better at 1.5 ps than at 2.5 ps. Theoretical results of both models agree qualitatively with the experimental data: the maximal 3D alignment is around 1.5 ps, and there is delocalization at larger times.

Quantitatively, there are however differences between the theoretical results shown in this section and the experiment in [1, 2]. First of all, the theoretical degree of 3D alignment at  $t = 1.4$  ps is a lot better than what is found experimentally at  $t = 1.47$  ps. Secondly, there are differences when it comes to the delocalization process. This is shown in figure 8.9, where we note that the delocalization seems to be quite fast compared to figure 3.4 (a). The width of the peaks increases until the entire circle is covered by both the fluorine and the bromine ring at  $t = 4.9$  ps. This should be compared to the experimental ion image at  $t = 5.6$  ps, where the bromine ring is still quite localized, but the fluorine ring is almost delocalized. We also note that the large difference between the delocalization rates of F and Br seen experimentally are not reproduced by the theory. Another feature of the theoretical calculations is that the wide peaks in the probability density seen in figure 8.9 each consist of many narrow peaks. It remains so until large times, as seen in figure 8.8 at  $t = 9.8$  ps. Such a structure of many narrow peaks is not seen experimentally in 3.4 (a) at any times.

The 2D model can also be used to find probability density plots to compare to the ion images found in the experiment in [3]. In the experiment, the ion images show some initial degree of 3D alignment. This degree of 3D alignment is increased shortly after, when the kick pulse hits the molecules. After a few picoseconds, the degree of 3D alignment decreases (see figures 3.5 and 3.7). Theoretical calculations of the same phenomena are seen in figure 8.10 for parameters that fit the experiment. At  $t = -0.2$  ps, there is some degree of 3D alignment, and at about 1.4 ps the degree of alignment reaches a maximum. At later times, the delocalization

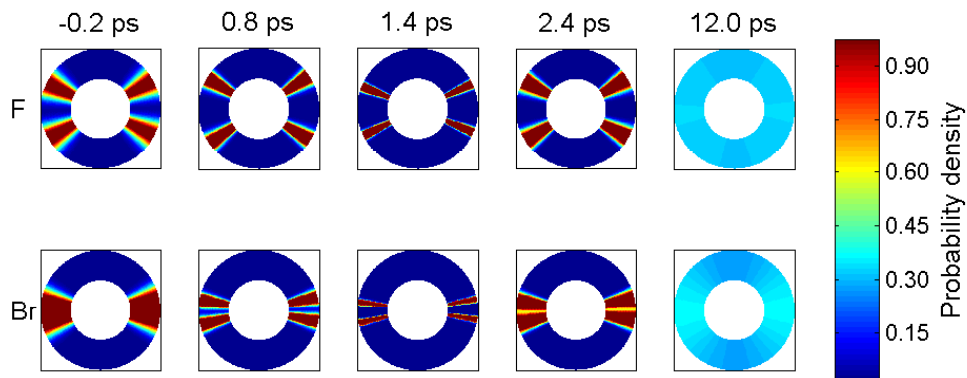


Figure 8.10: Calculated probability density plotted as a function of  $\phi_2$  (F) and  $\phi_1$  (Br) at different times, with the zero-point for the angles being to the right in each plot. The calculations were done with laser parameters identical to the experiment in [3] and an initial state that is 3D aligned. The Gaussian in  $\Phi$  of the initial state has a width of 0.5 rad, and the calculations were started at  $t = -0.4$  ps. The circular plots were created by adding the probability density to itself reflected in the vertical and in the horizontal axis (see section 8.6 for a more thorough discussion). When comparing this figure to [3], please note that the experimental ion images correspond to a different torsional potential with minimum at a dihedral angle of about  $38^\circ$ . For the calculations in this figure, the torsional potential has a minimum at  $\phi_d = 39^\circ$ .

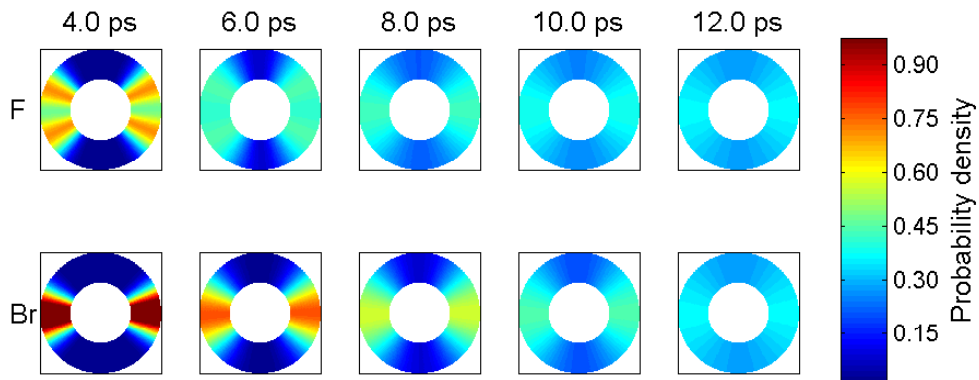


Figure 8.11: A continuation of figure 8.10 to larger times showing delocalization. For further information, see the caption of figure 8.10.



process starts, and finally at 12.0 ps, there is almost total delocalization. We conclude that there is a qualitative agreement between theory and experiment, though deviations are also seen. One of these deviations is that the 3D alignment seen at 1.4 ps is much better than what is seen experimentally in figure 3.5. This can be ascribed to the fact that the kick pulse also has a spatial width, so that only the molecules in the centre of the laser beam will be hit with the peak intensity, and the theoretical assumption of total initial 1D alignment described in section 3.2 also plays a role. The argument for explaining the high degree of 3D alignment in figure 8.8 at 1.4 ps is the same as for figure 8.10.

In figure 8.11, theoretical probability densities at larger times are shown. The calculations behind this figure use the same parameters as the experiment in [3], but note that a wrong torsional potential is used in the model, see the caption of figure 8.10. There is delocalization in both figure 3.7 and 8.11, and they also both show a slower delocalization for Br than for F. However, the tendency is not as obvious in the theoretical results as in the experiment. The theoretical delocalization is faster than what is seen experimentally for the bromine ring and slightly slower for the fluorine ring. The result is much better than what the 1D model could achieve in [2] at large times. In [2], it was concluded that the 1D model could not be expected to fit the experimental results at large times because the separation between  $\phi_d$  and  $\Phi$  would break down. The 2D model does not separate rotation and torsion, and the results are also better, as seen in figure 8.11.

When it comes to the figure 8.9, there are differences, as already mentioned. The main problem is the many narrow peaks that are seen. They start appearing right after the maximal 3D alignment has been reached, and their origin is not completely understood. They may be related to the very good 3D alignment achieved at 1.4 ps, because the maximal 3D alignment in figures 8.11, 3.4 and 3.7 is not quite as good as in figure 8.9. Also, the narrow peaks appear in the  $\phi_1$ -images first, and  $\phi_1$  is more localized than  $\phi_2$ . The peak in  $\phi_1$  at 1.4 ps in figure 8.9 has a width of approximately  $2^\circ$ , while the corresponding peak in figure 8.11 has a width of about  $3.5^\circ$ . Another difference is that delocalization rates of F and Br are not quite as different as in 3.4. This was also a problem in figure 8.11, though a smaller one. It is not clear which of the approximations from section 3.2 is the cause of this difference between theory and experiments.

## 8.6 Discussion of more general initial states

In the theoretical calculations that have been compared to the experiment in [1, 2], the initial state has been chosen as a localized state in  $\phi_d$ ,  $|L_{0,0}^{(1)}\rangle$ , see figure 6.3. As mentioned in section 5.6, this is just an approximation, because the localized states are not part of a complete basis, which means that an expansion of the initial state (5.28) in  $|L_{j,m}^{(i)}\rangle$  is not exact. They are not eigenstates of (6.1), the Hamiltonian without the kick pulse, because the four eigenstates with the lowest energy are not completely degenerate. It would therefore be more precise to use an eigenstate as the initial state instead. The reason why the localized initial state is chosen, is that the calculation of the expectation value of  $\phi_d$  becomes simpler when the wave function only has one peak in  $\phi_d$ .

The experimental initial states are of such a character that when 3D alignment sets in, four dots are visible in the angular distributions of the two rings, as seen in figures 3.4 (a) and 3.5. These four dots actually correspond to four different values of  $\phi_d$  and  $\Phi$ , but they are, nevertheless, turned into one expectation value of  $\phi_d$  in the data processing, as seen in figures 3.4 (c) and 3.6. This involves fitting the angular distributions to Gaussians at every point in

time where  $\langle \phi_d \rangle$  is wanted, which is time-consuming and can be difficult when the peaks are not well resolved, like the bromine ion images of figure 3.4.

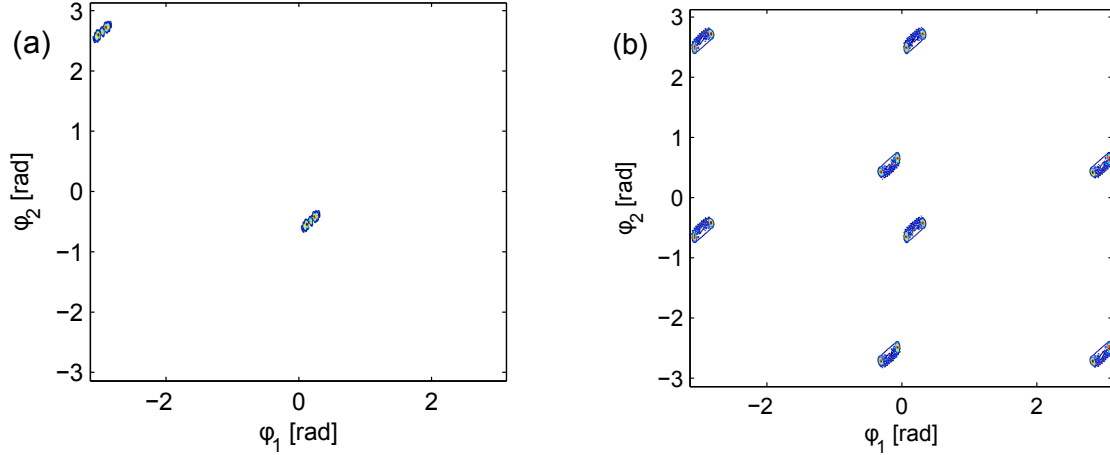


Figure 8.12: Contour plot of the norm squared of the wave function for calculations with different initial states at about 1.5 ps, where 3D alignment is very clear. The red lines show a large probability density, and the blue lines show a small one. The kick pulse parameters are matching the experiment in [1, 2]. (a) The initial state is the localized state  $|L_{0,0}^{(1)}\rangle$  (see figure 6.3). (b) The initial state is one of the four bottom eigenstates of the Hamiltonian without the kick pulse, (6.1) (see figure 6.1).

When a localized state like  $|L_{0,0}^{(1)}\rangle$  is propagated, and the kick pulse starts to 3D-align the molecules, the angular distributions of the bromine and fluorine ring do not show four peaks, but only two. This is because the dihedral angle is restricted to one of the wells in the torsional potential, so the wave function only contains two peaks, separated by  $180^\circ$  in  $\Phi$ . These peaks are seen in figure 8.12 (a), and they appear because the kick pulse 3D-aligns the molecules, it does not 3D-orient them. The theoretically found angular distributions of figure 8.8 show four peaks, not just two. They have been obtained by reflecting the distribution in the  $X$ -axis and adding the result to the original distribution. The reflection of the angular distribution would be the expected result of using one of the other localized states  $|L_{0,0}^{(i)}\rangle$ , so this procedure corresponds to adding the results incoherently. This is in agreement with (5.29), and the only problem is that the localized states are not exact eigenstates of (6.1). Since they are almost eigenstates, the error on the results is expected to be very small.

To check the position of the peaks occurring from 3D-aligning an initial state which is an eigenstate of (6.1), such a state has been propagated in the kick potential. In figure 8.12 (b) the resulting wave function is seen at the time of 3D alignment, and it is noticed that there are in fact eight peaks. Two peaks are seen in each well of the torsional potential, which makes sense because of the 3D alignment. One can also see that integration over  $\phi_1$  or  $\phi_2$  would give angular distributions with four peaks, which is what is seen experimentally.

In the theoretical calculations that are compared to [3], the initial state contains only one peak, see figure 8.2. In figure 8.10, this peak is seen four times by reflecting it in both the  $X$ - and  $Y$ -axes. This corresponds to incoherent addition of the four different peaks, and it is a bit unclear why we should be allowed to do so. It will be investigated now.

A state with a single peak, as the initial states used in calculations, is actually not a 3D-aligned state, but a 3D-oriented state. A 3D-aligned state would contain two peaks, like 8.12 (a). The reason for only studying one of the peaks is that both molecules described in this thesis are in fact  $\pi$ -periodic, not just  $2\pi$ -periodic. This means that the two peaks in 8.12 (a) describe the same orientation of the molecule. They are expected to give the same result, and this means that they can be added incoherently. The argument is the following: A coherent addition of two identical states  $\psi$  will give

$$|\psi + \psi|^2 = 4|\psi|^2, \quad (8.11)$$

where the incoherent addition gives (see section 2.6)

$$|\psi|^2 + |\psi|^2 = 2|\psi|^2. \quad (8.12)$$

The only difference is an overall factor, which does not change the physics, so an incoherent addition will work well. Since the two peaks are expected to act in the same way when hit by the kick pulse, there is no need to calculate the result for them both. It is enough to study one peak and use symmetry considerations to acquire information of the other peak. As a matter of fact, the real 3D-aligned initial state should consist of eight peaks, like it is seen in figure 8.12 (b). One should include peaks in each torsional well in the initial state, so that their contributions are added coherently. The problem can be simplified by noting that four of the eight peaks actually correspond to the same orientation of the molecule: The ones that are also seen in figure 8.12 (a), the upper middle peak and left middle peak. It is therefore enough to only study one of those peaks. The four remaining peaks correspond to another orientation of the molecules with a different dihedral angle,  $-39^\circ$ , and can also be represented by just one peak. We are thus left with two peaks, and they should, in principle, be added coherently. Since the peaks are well separated by the torsional barrier, it is expected to be a good approximation to treat them incoherently anyway. It seems that this approximation can be explained much better than another approximation already introduced: using an initial state that is not an eigenstate of (6.1), but instead a localized state in  $\phi_d$  and  $\Phi$ . Therefore, the coherent addition of contributions from multiple wells in the torsional potential is not expected to have much influence on the results.

In conclusion, the theoretical results are not expected to be improved significantly by studying initial states that have a finite value in all four wells of the torsional potential. We can, to a good approximation, treat the initial state as being localized in one torsional well, and use incoherent addition to recreate the experimental situation, as was done in figure 8.8 and 8.10, for instance. This corresponds to treating the states as mixed states, see section 2.6.

## 8.7 Summary

The results of this chapter show oscillations in the dihedral angle, just as was observed experimentally in [1, 2, 3] and found using the theoretical model presented in [2]. In both experiments and all simulations, the period is about 1.2 ps, and it stems from the energy difference between two eigenstates of the Hamiltonian without the kick pulse.

The amplitude of the oscillations depends on the initial state. For initial states with a fixed value of  $\Phi$ , the amplitude may be larger than for states that are delocalized in  $\Phi$ . This is consistent with the experiments, but the values of the amplitude found by the 2D model are not in quantitative agreement with experimental results, deviating by up to a factor of two. The results are better than for the 1D model when comparing to [1, 2]. This experiment leads to an

amplitude of  $\sim 0.6^\circ$ , the 1D model  $3.1^\circ$  and the 2D model  $0.4^\circ$ . In [3], an experimental oscillation in  $\langle \phi_d \rangle$  of amplitude  $3^\circ$  was found, the 1D model yields an amplitude of  $6.8^\circ$ , and the 2D model show oscillations of  $6.5^\circ$ . This deviation is believed to be caused by approximations of the model, including the assumption of total initial 1D alignment, and, most importantly, by focal volume effects.

For initial states localized in  $\Phi$ , it is seen that the amplitude of the oscillations in  $\langle \phi_d \rangle$  is largest around  $\Phi \sim \pm 90^\circ$ , where  $\Phi = 4.3^\circ$  was used in the experiment in [3]. Therefore, rotating the initial state by approximately  $90^\circ$  might be a good idea for future experiments. This rotation can be done by changing the polarization direction of the elliptically polarized alignment pulse, and it might increase the amplitude of the experimental oscillation from about  $3^\circ$  to  $4\text{--}5^\circ$ .

The amplitude calculated for an initial state that is initially 3D-aligned also depends on the shape of the  $\Phi$ -dependence. In the simulations described in this chapter, the initial state was a Gaussian in  $\Phi$  with a width of about  $0.5 \text{ rad} \approx 30^\circ$ , which is close to the state used in experiments. Wider  $\Phi$ -distributions will lead to smaller oscillations, and the same thing will happen for very narrow  $\Phi$ -distributions.

The 2D model solved in this thesis agrees qualitatively with experimental results at times above 4 ps. Experimental observations show that the state begins to delocalize at large times, and that the delocalization process is a lot faster for the fluorine ring than for the bromine ring. This delocalization is also seen in theoretical calculations using the 2D model, as is the difference in delocalization rates for F and Br, which is not as outspoken as in experiments, though. The agreement with the experimental results is better than the 1D model, because the separation between rotation and torsion breaks down at larger times. The differences between the results of the 2D model and experiments are ascribed to the theoretical assumption of total 1D alignment and focal volume effects. For comparing with the experiments of [3], it will also make a difference that the torsional potential of the wrong molecule has been used in the model.

In the last section, more complicated choices of initial states than the ones used in the calculations were discussed. It is not expected that choosing a more complicated initial state will make much of a difference, but it might give results that are a little bit closer to what is seen experimentally.

## Chapter 9

# Future perspectives

### 9.1 Laser induced deracemization

As mentioned in chapter 1, one of the reasons for investigating the effects of lasers on torsional motion of molecules is the possibility of laser induced deracemization. To obtain deracemization using short laser pulses, one must be able to change  $\langle\phi_d\rangle$  by more than  $39^\circ$ . This will allow the molecule to flip into its mirror form, since it has overcome the torsional barrier at  $\phi_d = 0^\circ$ . Right now, one has only achieved experimental oscillations in  $\langle\phi_d\rangle$  with a much lower amplitude than  $39^\circ$ .

Now, there are a few obstacles on the road towards laser induced deracemization. One is that the torsional barrier seems to be too large to overcome with ultrashort lasers without dissociating the molecule. The pulse must not be intense enough to ionize the material, but it still has to have a great impact on the dihedral angle, which is hard to achieve. What is found in experiments and the corresponding numerical simulations is just small oscillations in the dihedral angle. It has been discussed in [1, 2] that using trains of kick pulses might improve the control of torsion. The reason is that the degree of non-adiabatic alignment can be improved by using multiple pulses [27], and this is believed to increase the amplitude of the torsional oscillations. In section 8.4, the degree of 3D alignment of the initial state is varied, and the conclusion is that this cannot increase the oscillation amplitude much. Since the maximum oscillation amplitude that we find occurs at the same width of the initial Gaussian as was used in figure 8.3, the amplitude of  $6.5^\circ$  seen in that figure is the maximum value that can be achieved by using better 3D alignment. The experimental result from [3] is  $3^\circ$ , so using trains of kick pulses cannot increase the oscillation amplitude by more than a factor of two. Another option is decreasing the torsional barrier itself, which we will return to at the end of this section.

There is also another problem. To obtain deracemization, it is not enough to ensure that one enantiomer  $S_a$  is converted into its mirror image  $R_a$ , because the molecular gas will contain a 50 : 50 ratio of the two enantiomers. The  $R_a$  enantiomer must not be converted into  $S_a$ , since the net result would then be a 50 : 50 ratio again. What is needed is an interaction between the kick pulse and the molecule that is stronger for the  $S_a$  enantiomer than for the  $R_a$ . This can only be achieved if the molecules are initially 3D-oriented, since there is otherwise no way of telling the difference between the two enantiomers. What is studied is projections of the molecule onto the  $XY$ -plane (see figure 3.3). Such a projection of an  $R_a$  enantiomer with the bromine end pointing in the  $+Z$ -direction cannot be discriminated from a projection of an  $S_a$  enantiomer with the bromine end pointing in the  $-Z$ -direction. A 50 : 50 ratio of aligned enantiomers will thus stay a 50 : 50 ratio, unless the molecules are oriented instead of aligned.

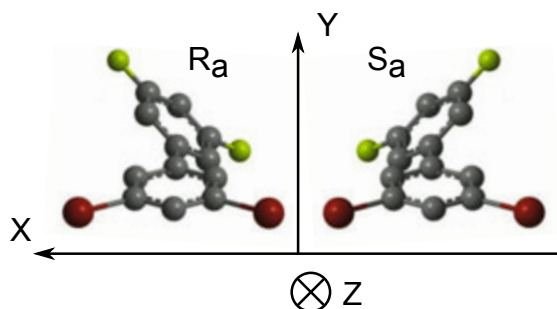


Figure 9.1: This shows the orientation of the axes of the 3D oriented molecules. The red atoms are Br and the yellow ones are F. It is seen here that the  $R_a$  enantiomer has  $\phi_d = -39^\circ$ , while  $S_a$  has  $\phi_d = 39^\circ$ . Note that this is a different choice of orientation of the axes than in [2].

3D orientation can be obtained experimentally by combining the alignment pulse with a static electric field. In the following discussion the bromine ring will be pointing out of the paper, which is in the  $-Z$ -direction, and the fluorine ring into the paper, in the  $+Z$ -direction. The choice of sign for  $\phi_1$  and  $\phi_2$  shown in figure 3.3 determines the orientation of the X-axis. This means that the enantiomer with  $\phi_d = 39^\circ$  is  $S_a$ , and the enantiomer with  $\phi_d = -39^\circ$  is  $R_a$ , as seen in figure 9.1. The calculations done in this thesis are for  $\phi_d = 39^\circ$ , which is the  $S_a$  enantiomer, so the figure 8.4 applies to  $S_a$ .

As we will see later, initial alignment of the SMPA at an angle of  $-13^\circ$  with respect to the X-axis yields an interaction that is different for the two enantiomers. This alignment leads to  $\Phi = -8.7^\circ$  for the  $S_a$ , which means that there is quite a strong interaction, as seen in figure 8.4. Since this figure is calculated for  $S_a$ , it is not clear at this point that it should also apply to  $R_a$ , and we will show that the interaction is actually not quite as strong for  $R_a$  as it is for  $S_a$  with this choice of alignment of the SMPA.

To understand the interaction strengths between laser and molecule for the two different enantiomers, we study the kick potential, which is given in  $(\phi_d, \Phi)$ -coordinates by (5.26) and seen in figure 4.4. By looking at (4.28) as well, it is noticed that the kick potential is an even function in the sense that changing the sign of both  $\phi_d$  and  $\Phi$  will leave it unchanged. The same is the case for the torsional potential (3.1), since it is even in  $\phi_d$  and independent of  $\Phi$ . On top of that, we note that changing from one enantiomer to the other corresponds to changing the sign of  $\phi_d$  from  $39^\circ$  to  $-39^\circ$ . We can therefore conclude that the enantiomer with  $\phi_d = -39^\circ$  ( $R_a$ ) will oscillate in  $\phi_d$  with an amplitude that has a dependence on  $\Phi$  similar to what was found for  $S_a$  in figure 8.4, but with the  $\Phi$ -axis reversed. Since there seems to be a symmetry around this axis in the figure, the corresponding figure for  $R_a$  will be very similar to 8.4.

Now, the reason for the different interaction strengths for the two enantiomers is that they will not have the same value of  $\Phi$  when the SMPA is aligned  $-13^\circ$  from the X-axis. In fact, the  $S_a$  enantiomer has  $\Phi = -8.7^\circ$  and the  $R_a$  enantiomer has  $\Phi = -17.2^\circ$ . By looking at figure 8.4, we see that the  $S_a$  enantiomer will experience an oscillation of larger magnitude than the  $R_a$  enantiomer.

With a numerical simulation using the 1D model, it was shown in [2] that it is theoretically possible to obtain laser induced deracemization by aligning the SMPA  $13^\circ$  from the X-axis. The simulation uses a kick pulse intensity of  $1.2 \text{ W cm}^{-2}$  and a pulse length of 1.0 ps, while the torsional potential was also diminished by a factor of four compared to the one used in

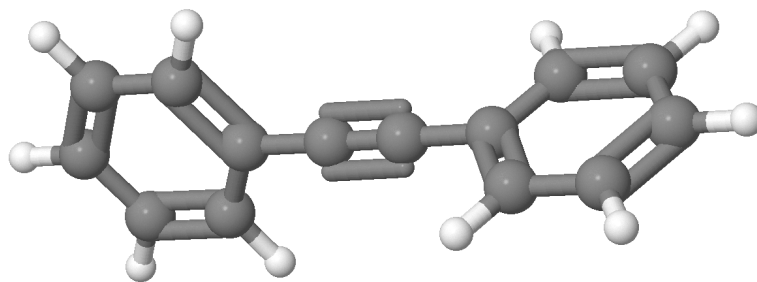


Figure 9.2: The molecule diphenylacetylene (tolane) has a torsional barrier of about 25 meV, which is a factor of three lower than DFDBrBPh. This figure is taken from [www.chembase.com](http://www.chembase.com).

this thesis. This result of the calculation was that 99% of the  $R_a$  enantiomers were converted into  $S_a$ , while only 13% of the  $S_a$  enantiomers were converted back. The only problems are that the laser intensity and pulse length are both relatively large, which means that the pulse has a large fluence, and the torsional barrier has to be lowered. It seems that laser pulses with quite a high fluence are needed to obtain deracemization, even when the torsional potential has been lowered, and a pulse of high fluence has a higher risk of ionizing the molecule. The kick pulse intensity is namely not too far from  $10^{14} \text{ W cm}^{-2}$ , which is usually considered the threshold for multiphoton excitation (see figure 2.2).

Based on figure 8.4, one could also try to align the SMPA at an angle that would give  $\Phi$ -values closer to  $90^\circ$ . The oscillations in  $\langle \phi_d \rangle$  will then be of larger amplitude and the curve in 8.4 is also steeper, such that it is possible to obtain a larger difference between the amplitude of the oscillation for the two enantiomers. There is, however, a problem. Figure 8.4 does not say anything about which way the dihedral angle is pushed by the laser, whether it is increased or decreased in the first quarter-cycle of the oscillation in  $\langle \phi_d \rangle$ . For values of  $\Phi$  around  $90^\circ$ , the dihedral angle is increased, at least if the initial state is  $S_a$  ( $\phi_d = 39^\circ$ ). Since the torsional potential has a larger barrier in that direction (see 3.2), this is not too promising for obtaining deracemization. For  $\Phi \approx 0^\circ$ , the dihedral angle is decreased by the laser interaction. Therefore,  $\Phi \approx 0$  might seem to be a better choice, but we must remember that the peak in figure 8.4 at  $\Phi \approx 90^\circ$  is also larger than the peak at  $\Phi \approx 0^\circ$ . As a result, it is hard to tell whether achieving deracemization will be easier for  $\Phi \approx 90^\circ$  or  $\Phi \approx 0^\circ$ .

Using an intense pulse without ionizing is not the only challenge. From the theoretical simulation of [2], it is seen that the torsional potential might have to be lowered by about a factor of four or more to achieve deracemization. This can be achieved by studying a different molecule. By using diphenylacetylene (tolane, see figure 9.2), the torsional barrier is reduced by about a factor of three [46], so for that molecule the laser induced deracemization might be easier to achieve.

Another way of improving the experiments is to use quantum optimal control, as will be discussed in the next section.

## 9.2 Quantum optimal control

One way to improve the control of molecular torsion in the future is to use quantum optimal control. It might be possible to tailor a specific and complicated kick pulse that does a better

job than the Gaussian pulse used so far. The shape of such an optimal pulse can be found theoretically by using quantum optimal control theory (QOCT) [47], and it has not been applied to this problem yet. It is also experimentally possible to create rather complicated pulses using pulse-shaping techniques [48]. Quantum optimal control seems to be the next step in the search for control of torsional motion in molecules.

The idea in QOCT is to find a laser pulse that maximizes the expectation value of a given operator in the final state at time  $T$ . If the goal is to do deracemization, and the initial state is localized in  $\phi_d$  with  $\phi_d = 39^\circ$ , that is  $|L_{0,0}^{(1)}\rangle$  (see figure 6.3), the relevant operator is the projection operator of the localized state with  $\phi_d = -39^\circ$ . This state is denoted by  $|L_{0,0}^{(2)}\rangle$ , so the projection operator is  $|L_{0,0}^{(2)}\rangle\langle L_{0,0}^{(2)}|$ . The expectation value of this operator in the final state at time  $T$  is

$$\langle\psi(T)|L_{0,0}^{(2)}\rangle\langle L_{0,0}^{(2)}|\psi(T)\rangle = |\langle\psi(T)|L_{0,0}^{(2)}\rangle|^2 \quad (9.1)$$

We see that the expectation value of the projection operator corresponds to the overlap between the final state and the desired state. It is therefore sensible to maximize this object.

The maximization can be done under certain constraints, for example minimizing the fluence of the laser field or keeping it constant. This is relevant if QOCT is to be applied to the study of torsion in molecules, since a large fluence will result in a destruction of the molecule, for example via multiphoton ionization. One can also limit the frequencies of the laser field, which is also relevant here. Large frequencies will allow for ionization, which is undesirable in our case.

In practice, QOCT is based on iterative algorithms, and hundreds of iterations are often needed. This means that the time-dependent Schrödinger equation has to be solved hundreds of times, which makes it time-consuming to find a solution.

The pulses that emerge from such calculations are often so complicated that they cannot be reconstructed experimentally. Usually, there are some features of the new pulse that can be created experimentally, and the use of QOCT might therefore lead to better control of the torsional motion.

### 9.3 Molecular switch

Control of torsional motion of biphenyl-like molecules might be applied to construct an ultrafast molecular switch, as noted in [2]. The idea is to use the molecules in a molecular junction, which means that a single or a small group of molecules will conduct electrical current between two electrodes [49]. The conductivity of a biphenyl-like molecule will depend on the dihedral angle with a maximum at  $0^\circ$  and a minimum at  $90^\circ$  [50], so the conductivity of the molecular junction can be controlled if the torsional motion is controlled. If this works, one will have a molecular switch that can operate on a very short time scale, since the involved laser pulses are short (1 ps or below).

Whether it is possible to use biphenyls as molecular switches depends on many things. First of all, the torsional motion must be under better control than it is today, otherwise it will not be possible to twist the molecule from  $\phi_d = 0^\circ$  to  $\phi_d = 90^\circ$ . Another problem is that the dependence of the conductivity on the dihedral angle is not known precisely. The difference between the minimum and the maximum current has to be significant if the molecule is to work properly as a switch. To obtain this information, one has to calculate the current-voltage characteristics of a molecule between two electrodes for different choices of the dihedral angle, as described in [51].



## Chapter 10

# Conclusion

With the arrival of ultrashort laser pulses, it has become possible to access molecular degrees of freedom that could previously not be probed. It is now possible to initiate torsional motion in certain molecules and to study the motion in a time-resolved manner. In this thesis, the torsional motion of biphenyl-like molecules when affected by intense laser pulses is studied theoretically. The results are compared to experiments from [1, 2, 3] and to a theoretical model described in [2]. The experiments are based on hitting the biphenyl-like molecules by three laser pulses. First, an alignment pulse aligns the molecules, then a kick pulse initiates torsional motion, and finally, a probe pulse is used to measure the dynamics. The experiment in [3] uses a 3D alignment pulse, where [1, 2] use a 1D alignment pulse.

The primary model used for simulations in this thesis is similar to the one described in [2]. Both models assume total initial 1D alignment of the molecules and rigid phenyl rings, so that the system is described by two coordinates,  $\phi_1$  and  $\phi_2$ . The model from [2] separates torsional ( $\phi_d$ ) and rotational ( $\Phi$ ) motion, and the problem is reduced to a 1D quantum mechanical problem for the torsion. The separation is achieved by an approximation, and this approximation is not needed in the primary model of this thesis. The primary model does not separate torsion and rotation, but sticks to solving a 2D quantum mechanical problem in the coordinates  $\phi_1$  and  $\phi_2$ . Since there are fewer approximations related to this 2D model, it is expected to give a better result when comparing to the experiments in [1, 2, 3].

First, the 1D model has been implemented, and its results compared to experiments. Then the 2D model has been discussed. The Hamiltonian for the 2D system *without* the kick pulse has been studied, and eigenstates and eigenvalues found. Surprisingly, the energies found are almost identical to the ones found when making the approximation of separating rotation and torsion. This peculiarity has been explained by studying the approximation in detail. It has also been shown that an exact decoupling of rotation and torsion can be done when the kick pulse is not applied.

Using an initial state that is almost an eigenstate of the Hamiltonian without the kick pulse and localized in one of the four wells of the torsional potential, the time evolution of a molecule in the 2D model has been found. Numerical solutions of the 2D model show oscillations in  $\langle \phi_d \rangle$  that are similar to the ones seen in experiments and in the 1D model. The period of these oscillations is about 1.2 ps in both models and experiments, and it relates to the energy difference between two eigenstates of the Hamiltonian for the system without the kick pulse. The amplitude of the oscillations show different values in the different experiments. In [1, 2], the experiments show a amplitude of  $\sim 0.6^\circ$ , whereas the 1D model finds  $3.1^\circ$  and the 2D model  $0.4^\circ$ . In [3], an experimental amplitude of  $3^\circ$  was found, where the 1D model finds  $6.8^\circ$  and the 2D model  $6.5^\circ$ . The differences between theory and experiment could be caused by

focal volume effects and the assumption of total 1D alignment used in the models. The reason for the larger amplitude in [3] than in [1, 2] is that the initial state is 3D-aligned, meaning that it is localized in  $\Phi$ . The 1D model cannot treat a state that is delocalized in  $\Phi$ , which is why it yields such a high value of the oscillation amplitude when comparing to the experiment in [1, 2].

For states that are initially localized in  $\Phi$ , it has been found that the amplitude of the oscillation in  $\langle\phi_d\rangle$  strongly depends on the initial value of  $\Phi$ . The amplitude is largest with initial values of  $\Phi$  about  $\pm 90^\circ$ ,  $0^\circ$  and  $-180^\circ$ . The peaks at  $\pm 90^\circ$  are largest, and in the experiment, a value of  $4.3^\circ$  is used. We thus conclude that the amplitude of the experimental oscillations can be increased by rotating the initial state by  $\approx 90^\circ$ . Such a rotation can be done by changing the direction of the polarization of the 3D alignment pulse, and it should increase the experimental oscillation amplitude from about  $3^\circ$  to  $4-5^\circ$ .

It has also been shown that the oscillation amplitudes for states that are initially 3D-aligned depend on the shape of the  $\Phi$ -dependence. In some of the 2D calculations in this thesis, the  $\Phi$ -dependence was chosen to be a Gaussian, and by varying the width, different amplitudes of the oscillation were seen. The width chosen for comparison to the experiment in [3] is  $0.5\text{ rad} \approx 30^\circ$ , which gives an amplitude near the maximum value. Since the amplitudes found using the model are a factor of two above the experimental value, we conclude that the amplitude of the oscillation in  $\phi_d$  cannot be increased by more than a factor two by using a more localized initial state, for example by using multiple kick pulses.

At times above 4 ps, the theory developed in this thesis does not give exactly the same results as were seen experimentally, but the agreement is much better than for the 1D model. The reason is that the separation of rotation and torsion in the 1D model is done in an approximate manner, and the underlying approximation breaks down at large times. It is seen in both experiments and theory that the molecules experience delocalization at times about 10 ps, and the delocalization rate is fastest for the fluorine ring. The remaining differences at large times is ascribed to the assumptions of the model, as mentioned above.

In all calculations, an initial state that is localized in  $\phi_d$  has been used. It would be more precise to use an initial state that is in fact an eigenstate of the Hamiltonian without the kick pulse, but it has been argued that the corrections will be rather small.

As a future application of the control of torsional motion, one hopes to enable laser induced deracemization with experiments like [1, 2, 3], i.e. to change between enantiomers at  $\phi_d = 39^\circ$  and  $\phi_d = -39^\circ$ . This is theoretically possible, since a different effect of the laser pulse on each of the two enantiomers can be obtained by 3D-orienting the initial state. It does however require an increase of the electric field strength and a reduction of the torsional barrier to obtain laser induced deracemization.

Another possibility of increasing the control of torsional motion is to use quantum optimal control. This has not been tried in this thesis, but remains a future research topic.

If complete torsional control is achieved, the molecules might be used as ultrafast molecular switches, because the conductivity depends on the torsional angle.

## Appendix A

# Matrix elements of the torsional potential

In this appendix the full calculations of the matrix elements used in sections 5.4 and 6.2 are calculated. The first matrix elements to be discussed are the ones used in chapter 5. In the exponential basis, they were actually calculated in section 5.4, so here we will show the calculation in the sine/cosine-basis. There are quite many cases to take care of. First, when  $|m'\rangle$  and  $|m\rangle$  are states that correspond to sines we find

$$\begin{aligned} \langle m' | V_{\text{tor}} | m \rangle &= \frac{1}{\pi} \int_{-\pi}^{\pi} d\phi_d \sin(m'\phi_d) \sin(m\phi_d) \left[ a \cos(4\phi_d) + b \cos(2\phi_d) \right. \\ &\quad \left. + d \cos(6\phi_d) + e \cos(8\phi_d) + c \right] \\ &= -\frac{1}{4\pi} \int_{-\pi}^{\pi} d\phi_d \left( e^{im'\phi_d} - e^{-im'\phi_d} \right) \left( e^{im\phi_d} - e^{-im\phi_d} \right) \left[ \frac{a}{2} \left( e^{i4m'\phi_d} + e^{-i4m'\phi_d} \right) \right. \\ &\quad \left. + \frac{b}{2} \left( e^{i2m'\phi_d} + e^{-i2m'\phi_d} \right) + \frac{d}{2} \left( e^{i6m'\phi_d} + e^{-i6m'\phi_d} \right) + \frac{e}{2} \left( e^{i8m'\phi_d} + e^{-i8m'\phi_d} \right) + c \right] \end{aligned}$$

A few calculations show that

$$\begin{aligned} \langle m' | V_{\text{tor}} | m \rangle &= -\frac{1}{2} \left[ a \left( \delta_{m'+m,4} - \delta_{m'-m,-4} - \delta_{-m'+m,-4} \right) + b \left( \delta_{m'+m,2} - \delta_{m'-m,-2} - \delta_{-m'+m,-2} \right) \right. \\ &\quad \left. + d \left( \delta_{m'+m,6} - \delta_{m'-m,6} - \delta_{m'-m,-6} \right) + e \left( \delta_{m'+m,8} - \delta_{m'-m,8} - \delta_{m'-m,-8} \right) - 2c\delta_{m',m} \right] \end{aligned}$$

Here, it has been used that there are no basis states with negative values of  $m$  or  $m'$ .

If both  $|m'\rangle$  and  $|m\rangle$  are states that correspond to cosines, we find

$$\begin{aligned}
\langle m' | V_{\text{tor}} | m \rangle &= \frac{1}{\pi} \int_{-\pi}^{\pi} d\phi_d \cos(m'\phi_d) \cos(m\phi_d) \left[ a \cos(4\phi_d) + b \cos(2\phi_d) \right. \\
&\quad \left. + d \cos(6\phi_d) + e \cos(8\phi_d) + c \right] \\
&= \frac{1}{4\pi} \int_{-\pi}^{\pi} d\phi_d \left( e^{im'\phi_d} + e^{-im'\phi_d} \right) \left( e^{im\phi_d} + e^{-im\phi_d} \right) \left[ \frac{a}{2} \left( e^{i4m'\phi_d} + e^{-i4m'\phi_d} \right) \right. \\
&\quad \left. + \frac{b}{2} \left( e^{i2m'\phi_d} + e^{-i2m'\phi_d} \right) + \frac{d}{2} \left( e^{i6m'\phi_d} + e^{-i6m'\phi_d} \right) + \frac{e}{2} \left( e^{i8m'\phi_d} + e^{-i8m'\phi_d} \right) + c \right]
\end{aligned}$$

This can be calculated, and the result is

$$\begin{aligned}
\langle m' | V_{\text{tor}} | m \rangle &= \frac{1}{2} \left[ a \left( \delta_{m'+m,4} + \delta_{m'-m,-4} + \delta_{-m'+m,-4} \right) + b \left( \delta_{m'+m,2} + \delta_{m'-m,-2} + \delta_{-m'+m,-2} \right) \right. \\
&\quad \left. + d \left( \delta_{m'+m,6} + \delta_{m'-m,6} + \delta_{m'-m,-6} \right) + e \left( \delta_{m'+m,8} + \delta_{m'-m,8} + \delta_{m'-m,-8} \right) + 2c\delta_{m',m} \right]
\end{aligned}$$

Furthermore, if the constant term of  $m = 1$  for the cosine is involved, we can still use the formula above, but the matrix element has to be multiplied by  $1/\sqrt{2}$  afterwards. This is caused by the fact that the constant state  $1/\sqrt{2\pi}$ , where the other cosines are multiplied by the normalization constant  $1/\sqrt{\pi}$ . If  $|m\rangle$  corresponds to a cosine and  $|m'\rangle$  to a sine, the integral will be odd, so it vanishes. The same is true when  $|m\rangle$  corresponds to a sine and  $|m'\rangle$  to a cosine. Now, we know every matrix element of the torsional potential in the sine/cosine basis.

This was a lot harder than the exponential basis, and it is obvious that this calculation would have been really unpleasant if it was generalized to two dimensions. Therefore, we use only the exponential basis in the 2D model.

Now, we move on to the 2D integral in the exponential basis. Here the matrix elements of the torsional potential are

$$\begin{aligned}
\langle m_1, m_2 | V_{\text{tor}} | m_3, m_4 \rangle &= \frac{1}{4\pi^2} \int_{-\pi}^{\pi} d\phi_1 \int_{-\pi}^{\pi} d\phi_2 e^{i(m_3-m_1)\phi_1} e^{i(m_4-m_2)\phi_2} \\
&\quad \cdot [a \cos(4(\phi_1 - \phi_2)) + b \cos(2(\phi_1 - \phi_2)) + d \cos(6(\phi_1 - \phi_2)) + e \cos(8(\phi_1 - \phi_2)) + c] \\
&= \frac{1}{4\pi^2} \int_{-\pi}^{\pi} d\phi_1 \int_{-\pi}^{\pi} d\phi_2 \left[ \frac{a}{2} e^{i(m_3-m_1+4)\phi_1} e^{i(m_4-m_2-4)\phi_2} \right. \\
&\quad + \frac{a}{2} e^{i(m_3-m_1-4)\phi_1} e^{i(m_4-m_2+4)\phi_2} \\
&\quad + \frac{b}{2} e^{i(m_3-m_1+2)\phi_1} e^{i(m_4-m_2-2)\phi_2} + \frac{b}{2} e^{i(m_3-m_1-2)\phi_1} e^{i(m_4-m_2+2)\phi_2} \\
&\quad + \frac{d}{2} e^{i(m_3-m_1+6)\phi_1} e^{i(m_4-m_2-6)\phi_2} + \frac{d}{2} e^{i(m_3-m_1-6)\phi_1} e^{i(m_4-m_2+6)\phi_2} \\
&\quad + \frac{e}{2} e^{i(m_3-m_1+8)\phi_1} e^{i(m_4-m_2-8)\phi_2} + \frac{e}{2} e^{i(m_3-m_1-8)\phi_1} e^{i(m_4-m_2+8)\phi_2} \\
&\quad \left. + c e^{i(m_3-m_1)\phi_1} e^{i(m_4-m_2)\phi_2} \right] \\
&= \frac{a}{2} (\delta_{m_3-m_1,4} \delta_{m_4-m_2,-4} + \delta_{m_3-m_1,-4} \delta_{m_4-m_2,4}) \\
&\quad + \frac{b}{2} (\delta_{m_3-m_1,2} \delta_{m_4-m_2,-2} + \delta_{m_3-m_1,-2} \delta_{m_4-m_2,2}) \\
&\quad + \frac{d}{2} (\delta_{m_3-m_1,6} \delta_{m_4-m_2,-6} + \delta_{m_3-m_1,-6} \delta_{m_4-m_2,6}) \\
&\quad + \frac{e}{2} (\delta_{m_3-m_1,8} \delta_{m_4-m_2,-8} + \delta_{m_3-m_1,-8} \delta_{m_4-m_2,8}) + c \delta_{m_3,m_1} \delta_{m_4,m_2}.
\end{aligned}$$



# Bibliography

- [1] C. B. Madsen, L. B. Madsen, S. S. Viftrup, M. P. Johansson, T. B. Poulsen, L. Holmegaard, V. Kumarappan, K. A. Jørgensen, and H. Stapelfeldt. Manipulating the torsion of molecules by strong laser pulses. *Phys. Rev. Lett.*, 102:073007, Feb 2009.
- [2] C. B. Madsen, L. B. Madsen, S. S. Viftrup, M. P. Johansson, T. B. Poulsen, L. Holmegaard, V. Kumarappan, K. A. Jorgensen, and H. Stapelfeldt. A combined experimental and theoretical study on realizing and using laser controlled torsion of molecules. *The Journal of Chemical Physics*, 130(23):234310, 2009.
- [3] Jonas L. Hansen, Jens H. Nielsen, Christian Bruun Madsen, Anders Thyboe Lindhardt, Mikael P. Johansson, Troels Skrydstrup, Lars Bojer Madsen, and Henrik Stapelfeldt. Control and femtosecond time-resolved imaging of torsion in a chiral molecule. *The Journal of Chemical Physics*, 136(20):204310, 2012.
- [4] E. Goulielmakis, M. Schultze, M. Hofstetter, V. S. Yakovlev, J. Gagnon, M. Uiberacker, A. L. Aquila, E. M. Gullikson, D. T. Attwood, R. Kienberger, F. Krausz, and U. Kleineberg. Single-cycle nonlinear optics. *Science*, 320(5883):1614–1617, 2008.
- [5] G Mainfray and G Manus. Multiphoton ionization of atoms. *Reports on Progress in Physics*, 54(10):1333, 1991.
- [6] M. Lewenstein, Ph. Balcou, M. Yu. Ivanov, Anne L’Huillier, and P. B. Corkum. Theory of high-harmonic generation by low-frequency laser fields. *Phys. Rev. A*, 49:2117–2132, Mar 1994.
- [7] X. Liu, D. Du, and G. Mourou. Laser ablation and micromachining with ultrashort laser pulses. *Quantum Electronics, IEEE Journal of*, 33(10):1706 –1716, oct 1997.
- [8] S. Nolte, C. Momma, H. Jacobs, A. Tünnermann, B. N. Chichkov, B. Wellegehausen, and H. Welling. Ablation of metals by ultrashort laser pulses. *J. Opt. Soc. Am. B*, 14(10):2716–2722, Oct 1997.
- [9] D.A.B. Miller. Optical interconnects to silicon. *Selected Topics in Quantum Electronics, IEEE Journal of*, 6(6):1312 –1317, nov.-dec. 2000.
- [10] R. Ramaswami and K. Sivarajan. *Optical Networks: A Practical Perspective*. Morgan Kaufmann, third edition, 2010.
- [11] Ahmed H. Zewail. Laser femtochemistry. *Science*, 242(4886):1645–1653, 1988.
- [12] R. Fulton, A. I. Bishop, M. N. Shneider, and P. F. Barker. Controlling the motion of cold molecules with deep periodic optical potentials. *Nature Physics*, 2:465–468, 2006.

- [13] H. Stapelfeldt, Hirofumi Sakai, E. Constant, and P. B. Corkum. Deflection of neutral molecules using the nonresonant dipole force. *Phys. Rev. Lett.*, 79:2787–2790, Oct 1997.
- [14] Hoi Sung Chung, Bum Suk Zhao, Sung Hyup Lee, Sungu Hwang, Keunchang Cho, Sang-Hee Shim, Soon-Mi Lim, Wee Kyung Kang, and Doo Soo Chung. Molecular lens applied to benzene and carbon disulfide molecular beams. *The Journal of Chemical Physics*, 114(19):8293–8302, 2001.
- [15] Henrik Stapelfeldt and Tamar Seideman. *Colloquium* : Aligning molecules with strong laser pulses. *Rev. Mod. Phys.*, 75:543–557, Apr 2003.
- [16] Hiromichi Niikura, P. B. Corkum, and D. M. Villeneuve. Controlling vibrational wave packet motion with intense modulated laser fields. *Phys. Rev. Lett.*, 90:203601, May 2003.
- [17] Y. Fujimara, L. Gonzalez, K. Hoki, J. Manz, and Y Ohtsuki. Selective preparation of enantiomers by laser pulses: quantum model simulation for h2posh. *Chemical Physics Letters*, 306(1–2):1–8, 1999.
- [18] David Gerbasi, Moshe Shapiro, and Paul Brumer. Theory of enantiomeric control in dimethylallene using achiral light. *The Journal of Chemical Physics*, 115(12):5349–5352, 2001.
- [19] Petr Král and Moshe Shapiro. Cyclic population transfer in quantum systems with broken symmetry. *Phys. Rev. Lett.*, 87:183002, Oct 2001.
- [20] Dominik Kröner and Bastian Klaumünzer. Stereoselective laser pulse control of an axial chiral molecular model system supporting four stereoisomers. *Chemical Physics*, 338:268 – 276, 2007.
- [21] S. Ramakrishna and Tamar Seideman. Torsional control by intense pulses. *Phys. Rev. Lett.*, 99:103001, Sep 2007.
- [22] L. H. Coudert, Luis F. Pacios, and Juan Ortigoso. Rotation-induced breakdown of torsional quantum control. *Phys. Rev. Lett.*, 107:113004, Sep 2011.
- [23] Shane M. Parker, Mark A. Ratner, and Tamar Seideman. Coherent control of molecular torsion. *The Journal of Chemical Physics*, 135(22):224301, 2011.
- [24] J. Floss, T. Grohmann, M. Leibscher, and T. Seideman. Nuclear spin selective laser control of rotational and torsional dynamics. *The Journal of Chemical Physics*, 136(8):084309, 2012.
- [25] B. H. Bransden and C.J. Joachain. *Physics of Atoms and Molecules*. Pearson Education, second edition, 2003.
- [26] Christian Bruun Madsen. *Molecules in intense laser fields: Studies of ionization, high-order harmonic generation and alignment*. PhD thesis, University of Aarhus, 2010.
- [27] M. Leibscher, I. Sh. Averbukh, and H. Rabitz. Enhanced molecular alignment by short laser pulses. *Phys. Rev. A*, 69:013402, Jan 2004.
- [28] E. L. Eliel. *Stereochemistry of organic molecules*. John Wiley and Sons, first edition, 1994.
- [29] Friedrich Grein. Twist angles and rotational energy barriers of biphenyl and substituted biphenyls. *The Journal of Physical Chemistry A*, 106(15):3823–3827, 2002.



- [30] B. S. Gould, H. M. Goldman and H. N. Munro. The antiscorbutic action of l-ascorbic acid and d-isoascorbic acid (erythorbic acid) in the guinea pig. *Am J Clin Nutr*, 34(1):24–33, 1981.
- [31] J. J. Sakurai. *Modern Quantum Mechanics*. Addison-Wesley, revised edition, 1994.
- [32] Vinod Kumarappan, Christer Z. Bisgaard, Simon S. Viftrup, Lotte Holmegaard, and Henrik Stapelfeldt. Role of rotational temperature in adiabatic molecular alignment. *The Journal of Chemical Physics*, 125(19):194309, 2006.
- [33] Frank Filsinger, Jochen Kupper, Gerard Meijer, Lotte Holmegaard, Jens H. Nielsen, Iftach Nevo, Jonas L. Hansen, and Henrik Stapelfeldt. Quantum-state selection, alignment, and orientation of large molecules using static electric and laser fields. *The Journal of Chemical Physics*, 131(6):064309, 2009.
- [34] Mikael P. Johansson and Jeppe Olsen. Torsional barriers and equilibrium angle of biphenyl: Reconciling theory with experiment. *Journal of Chemical Theory and Computation*, 4(9):1460–1471, 2008.
- [35] Stephen J. Blanksby and G. Barney Ellison. Bond dissociation energies of organic molecules. *Accounts of Chemical Research*, 36(4):255–263, 2003.
- [36] D.J. Maas, D.I. Duncan, R.B. Vrijen, W.J. van der Zande, and L. D. Loordam. Vibrational ladder climbing in no by (sub)picosecond frequency-chirped infrared laser pulses. *Chemical Physics Letters*, 290(1-3):75–80, 1998.
- [37] Boyan T Torosov and Nikolay V Vitanov. Adiabatic elimination of a nearly resonant quantum state. *Journal of Physics B: Atomic, Molecular and Optical Physics*, 45(13):135502, 2012.
- [38] Benjamin J. Sussman, Jonathan G. Underwood, R. Lausten, Misha Yu. Ivanov, and Albert Stolow. Quantum control via the dynamic stark effect: Application to switched rotational wave packets and molecular axis alignment. *Phys. Rev. A*, 73:053403, May 2006.
- [39] P. W. Atkins. *Molecular quantum mechanics*. Oxford University Press, first edition, 1970.
- [40] H. Friedrich. *Theoretical Atomic Physics*. Springer, second edition, 1998.
- [41] Ole Sørensen and Klaus Mølmer. Born-oppenheimer description of two atoms in a combined oscillator and lattice trap. *Phys. Rev. A*, 86:013625, Jul 2012.
- [42] N. W. Ashcroft and N. D. Mermin. *Solid State Physics*. Harcourt College Publishers, first edition, 1976.
- [43] M.D Feit, J.A Fleck Jr., and A Steiger. Solution of the schrödinger equation by a spectral method. *Journal of Computational Physics*, 47(3):412 – 433, 1982.
- [44] C Leforestier, R.H Bisseling, C Cerjan, M.D Feit, R Friesner, A Guldberg, A Hammerich, G Jolicard, W Karrlein, H.-D Meyer, N Lipkin, O Roncero, and R Kosloff. A comparison of different propagation schemes for the time dependent schrödinger equation. *Journal of Computational Physics*, 94(1):59 – 80, 1991.
- [45] S. J. Leon. *Linear Algebra with Applications*. Prentice Hall, seventh edition, 2006.

- [46] Dong Xu and Andrew L. Cooksy. Ab initio study of the torsional motion in tolane. *Journal of Molecular Structure: THEOCHEM*, 815(1):119 – 125, 2007.
- [47] J Werschnik and E K U Gross. Quantum optimal control theory. *Journal of Physics B: Atomic, Molecular and Optical Physics*, 40(18):R175, 2007.
- [48] Constantin Brif, Raj Chakrabarti, and Herschel Rabitz. Control of quantum phenomena: past, present and future. *New Journal of Physics*, 12(7):075008, 2010.
- [49] Abraham Nitzan and Mark A. Ratner. Electron transport in molecular wire junctions. *Science*, 300(5624):1384–1389, 2003.
- [50] Jorge M. Seminario, Angelica G. Zacarias, and James M. Tour. Theoretical interpretation of conductivity measurements of a thiotolane sandwich. a molecular scale electronic controller. *Journal of the American Chemical Society*, 120(16):3970–3974, 1998.
- [51] Angelica Zacarias and E. Gross. Transport properties of chrysazine-type molecules. *Theoretical Chemistry Accounts: Theory, Computation, and Modeling (Theoretica Chimica Acta)*, 2010.